Developing Tools towards Ion Homeostasis in Spatially Polarized Excitable Cells

Ziyi Liu

Thesis submitted to the University of Ottawa in partial fulfillment of the requirements for the Master of Science in Physics

Department of Physics
Faculty of Science
University of Ottawa

Abstract

In 1800, Volta, inspired by the electric organs of a genus of electric fish, the *Electrophorus*, invented the first electric batteries, which were termed "artificial electric organs." Since then, the far-reaching implications of the fishes' electrogenesis have come under greater attention and interest. In these fishes, the electric organ resembles a series of batteries. The electric organs are formed by electrocytes (the "batteries") with a distinct cytomorphology for discharging and charging. Although the arrangements of electrocytes in the electric organ are well-understood, the mechanisms involved in generating electric discharges within equivalent circuits remain unclear. In this thesis, the first element consists of adapting spatially defined models that we use to investigate the process of electrocyte charging and recharging under the added assumption of ion homeostasis, the process by which a cell restores its internal milieu. The study focuses on *Eigenmannia* and *Electrophorus*, two genera of electric fish. *Eigenmannia*'s steady high-frequency dipole oscillator-like electric organ discharges enables electro-sensing and electro-communication, whilst *Electrophorus*'s brief taser-like electric bursts serve as tetanizing predatory assaults. In addition, the second section of this study proposes a one-dimensional charge difference model that focuses on the modification of endogenous electric fields resulting from the uneven distribution of ions in a homeostatic apparatus.

Résumé

En 1800, Volta, inspiré par les organes électriques d'un genre de poisson électrique, soit les *Électrophores*, inventa les premières piles électriques, qui sont nommés les « organes électriques artificielles ». Dès lors, les implications considérables de l'électrogénèse des poissons ont attiré d'importantes attentions et intérêt. Dans ces poissons, les organes électriques (EO) ressemblent à une série de piles. Elles sont formées par des électrocytes disposant d'une cyto-morphologie distincte pour décharger et charger. Bien que la configuration des électrocytes dans l'organe électrique soit bien comprise, les mécanismes impliqués dans la génération de décharges électriques dans des circuits équivalents restent inconnus. Dans cette thèse, le premier élément consiste à adapter les modèles définis dans l'espace que nous utilisons pour étudier le processus de charge et de recharge des électrocytes sous l'hypothèse supplémentaire de l'homéostasie ionique, le processus par lequel une cellule restaure son milieu interne. L'étude porte sur *Eigenmannia* et *Électrophores*, deux genres de poissons électriques. La décharge d'un organe électrique à haute fréquence d'*Eigenmannia*, semblable à un oscillateur dipôle, permet l'électrodétection et l'électro communication, tandis que les brèves rafales de décharges électriques des *Électrophores*, semblables à celles d'un taser, servent d'assauts prédateurs tétanisants. En outre, la deuxième partie de cette étude propose un modèle unidimensionnel de différence de charge qui se concentre sur la modification des champs électriques endogènes résultant de la distribution inégale des ions dans un appareil homéostatique.

Acknowledgement

I would like to take this opportunity to express my sincere and profound gratitude to my supervisor, Dr. Bela Joós, for the invaluable guidance and mentorship he has provided throughout my study of biophysics. Dr. Joós has been an exceptional mentor, whose generosity and expertise have been instrumental in shaping my academic and professional development.

I also could not have undertaken this academic journey without Dr. Cathy Morris. I appreciate her scientific curiosity and life and artistic zeal. I'd want to thank her for her consistent engagement and discussions with my supervisor, and her brilliant ideas regarding my projects.

I would like to express my sincere gratitude to Dr. Gary Slater for his invaluable help throughout my physics courses. Dr. Slater's expertise and guidance have been instrumental in my understanding of complex concepts and theories. His commitment to my success has been evident through his willingness to go above and beyond in answering my questions and providing additional resources to aid in my learning.

I would like to extend my heartfelt appreciation to Dr. Michael Wong for his invaluable guidance and advice on how to be a good Teaching Assistant.

I would like to thank the University of Ottawa for providing me with the exceptional bilingual atmosphere and scholarship that allowed me to obtain my education abroad.

I would like to express my deep gratitude to my family for their financial and emotional support. Their love, encouragement, and guidance have been the cornerstone of my personal and academic success.

I would like to thank my friends who have kindly provided me companionship during my study.

Finally, I am truly grateful to all who devote much time to reading this thesis and giving me a lot of advice, which will be beneficial to me in my further study.

List of Abbreviations

A: Cross-sectional area

AChR: Acetylcholine receptor

An^-: Impermeant intracellular anion (Donnan effector)

Ant.: Anterior

AP: Action potential

A_{post}: *Electrophorus* posterior membrane's area

ATP: Adenosine triphosphate

C_a: Membrane capacitance of the anterior end

Ccy: Connectivity

CD: Charge difference

C_p: Membrane capacitance of the posterior end

C_t: Membrane capacitance of the tubular invagination at the anterior end

$D_{impermeant\ anions}$: Diffusion coefficient of impermeant anions

$D_{permeant\ ions}$: Diffusion coefficient of permeant ions

EEF: Endogenous electric field

EO: Electric organ

EOD: Electric organ discharge

Epm: Excitable posterior model

F: Faraday constant

GHK: Goldman Hodgkin Katz

H-H: Hodgkin-Huxley model

L: Effective cell length

I_{AChR}: Acetylcholine receptor current

I_{axial}: Axial current

I_K: Delays rectifier potassium current

I_{leak}: Generic leak current

I_{La}: Generic leak current at the anterior end

$I_{Na,leak}$: Sodium leak current

$I_{K,leak}$: Potassium leak current

$I_{maxNaKpump}$: Maximum Na^+/K^+ pump current

I_{Na}: Transient sodium current

I_{stim}: Stimulus current initiates the action potential.

Kv: Voltage-gated potassium channel

M: Number of columns of electric organ

MP: Transmembrane potential

N: Number of electrocytes in each column

Nav: Voltage-gated sodium channel

PA-CD: Posterior anterior-charge difference (model)

$P_{AChR,K}$: Permeability of potassium flux throughs acetylcholine receptor

$P_{AChR,Na:}$ Permeability of sodium flux throughs acetylcholine receptor

P_{Cl}: Permeability of chloride leak channels

$P_{leak,Cl,a/p}$: Permeability of chloride leak channels at anterior or posterior end

P_K: Permeability of sodium leak channels

$P_{leak,K,a/p}$: Permeability of sodium leak channels at anterior or posterior end

P_{Kmax}: Maximum potassium permeability

P_{H2O}: Membrane water permeability

P_{leak} : Generic leak permeability at posterior end

P_{La} : Generic leak permeability at anterior end

P-L/D: Pump-Leak/Donnan

P_{Na}: Permeability of sodium leak channels

$P_{leak,Na,a/p}$: Permeability of sodium leak channels at anterior or posterior end

P_{Namax}: Maximum sodium permeability

Post.: Posterior

R: Gas constant

R_{cyt}: Cytoplasmic resistance

$R_{cyt,Eel}$: Cytoplasmic resistance of *Electrophorus*'s electrocyte

$R_{cyt,Eig}$: Cytoplasmic resistance of *Eigenmannia*'s electrocyte

R_{eff}: Effective resistance

R_{ext}: External resistance

R_{gap}: Gap resistance

R_{hsk}: Resistance of the skin of fish's head

R_{tsk}: Resistance of the skin of fish's tail

R_t: Tubular resistance

SA: Surface area

T: Temperature

V_a: Membrane potential at anterior end

Va_e: Exterior membrane voltage of the anterior compartment

Va_i: Interior membrane voltage of the anterior compartment

V_{cyt}: Cytoplasmic voltage

V_{ext}: External voltage

V_{in}: Interior membrane voltage

V_t: Tubular voltage

Vol_{cell}: Volume of the cell

V_{out}: Exterior membrane voltage

V_p: Membrane potential at posterior end

Vp_e: Exterior membrane voltage of the posterior compartment

Vp_i: Interior membrane voltage of the posterior compartment

Z_{ionX}: Valence of ionX

Table of Contents:

List of Figures

List of Tables

1.Introduction

1.1. Overviews

In 1800, Alessandro Volta, inspired by the natural "electric organs" of the *Electrophorus* electric fish, invented the first electric battery. This development sparked increased interest in electrogenesis in fishes, leading to notable discoveries about their electric organs (Finger and Piccolino, 2011). These organs, composed of specialized cells called electrocytes, operate analogously to batteries and are distinctively structured for either discharging or recharging electricity (Kramer, 2019). While the configurations of these electrocytes in the electric organ are well-understood, the mechanisms of the generation of the electric discharges at cell level within equivalent circuits remain unclear (Markham, 2013; Catania, 2014). This thesis seeks to explore this gap in knowledge by employing a spatially specific equivalent circuit model to study the charging and recharging processes of electrocytes, assuming ion homeostasis. We focus on two electric fish types, *Eigenmannia* and *Electrophorus*, which exhibit distinct electric organ discharges (EODs). *Eigenmannia* utilizes them for electro-sensing and communication (Lissmann, 1958), while *Electrophorus* employs them for predatory attacks (Gifford and Leming, 2021; Luft, 1957). Postulating that EODs can be tuned by altering physiological parameters, this study aims to enrich our understanding of these species. Additionally, the thesis introduces a one-dimensional charge difference model to study the ion homeostasis process and examine how cellular component distribution produces the endogenous electric field (EEF).

1.2. Background:

Electric fish express their characteristics through EOD, which we analyze using equivalent circuits. *Eigenmannia* is distinguished for its dipole-oscillator like and continuous high-frequency EODs, for navigation and communication. *Electrophorus* produces intense electric shocks, like tasers, used mainly for defense and predation. The equivalent circuits model for *Eigenmannia* and *Electrophorus* EOD is under the assumption of ion homeostasis.
In our study of ion homeostasis, the Posterior Anterior Charge Difference (PA-CD) model is employed. Ion homeostasis is a pump-leak Donnan mechanism. It is crucial for intracellular

environmental stability, especially how the system returns to the steady state after perturbations. This model considers the uneven distribution of cellular components and ion channels, which could produce an endogenous electric field (EEF). Research into the EEF reveals multiple physiological and biophysical aspects, such as wound healing and cell migration (Sanjuan-Alberte et al., 2018).

1.3. Main Research Questions:

In the equivalent circuit model, we focus on understanding how the spatial configurations and physiological characteristics of electrocytes in *Eigenmannia* and *Electrophorus* contribute to their distinct electric organ discharge patterns and figuring out the underlying mechanisms of electrocyte recharging in these fish. *Eigenmannia* and *Electrophorus* are evolutionarily closely related genera. We also aim to show that EODs are tunable by altering physiological parameters. Furthermore, the second part of this research introduces a one-dimensional charge difference model, focusing on endogenous electric fields due to the uneven distribution of cellular components to enhance our insight into homeostasis.

1.4. Equivalent Circuits for Electric Organ Discharge (EOD)

The order *Gymnotiforms*, also known as South American or Neotropical knifefish, are mostly nocturnal fishes (Henninger et al., 2020). *Gymnotiforms* cannot rely on vision for navigation; therefore, they emit and detect weak electric fields to sense and communicate with their environment (Lissmann, 1958). As of 2017, there are thirty-four recognized gymnotid genera (Ferraris Jr et al., 2017). *Eigenmannia*, *Sternopygus*, and *Electrophorus* are three closely related genera (Craig et al., 2019). In this research, we concentrate on *Eigenmannia* and *Electrophorus*. *Eigenmannia*, often referred to as glass knifefishes, are typically 10 to 20 centimeters long (Fig. 1.4.1 B). They are unique among their kind for their continuous high-frequency electric discharges, which occur both day and night (Fig. 1.4.1 A). *Electrophorus* species, on the other hand, are known for generating strong electric currents. These currents are so powerful that they can be used for both offense and defense (Gifford and Leming, 2021; Luft, 1957).

The electric discharges in these fish are produced by specialized cells called electrocytes, found within their electric organs (EO). These cells are responsible for creating action potential-based electric discharges (Bennett, 1971). Unlike the neurogenic electrocytes found in some other fish, the electrocytes in *Eigenmannia* and *Electrophorus* are myogenic, meaning they originate from muscle tissue (Thomas et al., 1996). However, these cells do not contract like normal muscle cells (Cuellar et al., 2006). Because of their relative simplicity compared to regular muscle cells, electrocytes are ideal for modeling ion homeostasis, a critical aspect of how these cells function.

At the electrocyte level, non-propagating action potentials (APs) generate currents that flow exclusively along the rostro-caudal axis (Assad et al., 1998). To model the size of the electric organ (EO) in multiple genera, we adopt a simplified approach in which only ten columns of 100 electrocytes are considered (Fig. 1.4.1 F). This configuration, 10x100, resembles a juvenile *Eigenmannia* EO (Kramer and Kaunzinger, 1991) and is significantly smaller than an *Electrophorus* EO (Xu et al., 2021).

Mechanistically, the medullary pacemaker nucleus controls EOD production. It synchronizes the EOD and modulates the fish's firing frequency . The EOD patterns (frequency ranges and waveforms) of gymnotiform fish are highly varied among genera. Among weak electric gymnotiform fishes, only the EODs of the genus *Eigenmannia* can be accurately described as simple oscillating dipoles in the near-field region (Fig. 1.4.1 C). Consequently, this characteristic renders *Eigenmannia* an ideal model for EOD study (Assad et al., 1998). Importantly, *Electrophorus* inspires extensive biomimetic research and inventions due to its strong electric charge and its far-reaching implications (Gifford and Leming, 2021). For instance, Xu and Lavan developed an equivalent circuit model to simulate AP creation in an electric eel's electrocyte by analyzing ion concentration gradients across ion channels and pumps. Their synthetic cells may have applications in medical implants and other micro-devices (Xu and Lavan, 2008). Sophisticated biophysical models are essential for studying these electrocytes. Notably, after a decade of research on electric fish (1959 - 1970). Bennett introduced the global equivalent circuit in 1971. This framework has influenced subsequent studies (Catania, 2016, 2017; Joos et al., 2018b; Song et al., 2020). Our aim is to develop a model that captures the biophysical complexity yet inherent simplicity of EODs, from electrocytes to the electric organ

level, drawing on Bennett's research and Joos's Epm model (Joos et al., 2018b). Currently, in the first part of this thesis, we propose a new paradigm: an EO electrical equivalent circuit model, incorporating ion homeostasis, which serves as a basis for developing spatially explicit models and a comprehensive ion homeostasis framework.

1.4.1. *Eigenmannia*

The genus *Eigenmannia* is widely distributed in Neotropical freshwater habitats across South America (Peixoto et al., 2015). *Eigenmannia* (Fig.1.4.1 B), a nocturnal species, generates weak electric organ discharges (EODs) at frequencies ranging from 250–500 Hz for navigation and communication in darkness (Markham, 2013). These EOD frequencies vary among individuals and occur continuously throughout the day and night (Scheich, 1977; Hopkins, 1974). *Eigenmannia*'s EODs exhibit a distinctive waveform characterized by a head-positive peak and a head-negative baseline (Bennett, 1971). During each EOD, the intensity of the electric field fluctuates from strong to weak while its direction remains constant (Assad et al., 1998).

The capability of *Eigenmannia* to produce EODs stems from its large, specialized electrocytes. Each electrocyte, measuring approximately 1.5 mm in length and 600 µm in width (Fig. 1.4.2), comprises three parts: an anterior section without nerve connections, a posterior section with nerve connections, and a central cell body (R_{cyt}). The cell body, primarily composed of cytoplasm, links the anterior and posterior sections, functioning as a resistor in an electric circuit (Bennett, 1971). Immunocytochemical evidence indicates that voltage-gated sodium channels and acetylcholine receptors are present exclusively at the posterior end (Ban et al., 2015). This suggests that the posterior end initiates currents flowing toward the anterior end by stimulating non-propagating action potentials. The concentration of cellular mitochondria at the posterior, the cell's energy generators, supports this hypothesis (Schwartz et al., 1975; Ban et al., 2015). Importantly, successive electrocytes do not have direct contact and are thus electrically isolated, as illustrated in Fig.1.4.1 D.

The spaces between electrocytes along a column contain axon terminals and blood vessel penetration, increasing the longitudinal resistance (R_{gap}). An insulating connective tissue sheath

envelops the electrocyte edges longitudinally. These features are vital for EOD production, enabling current to flow along the organ's axis (head to tail) (Bennett, 1971). As components of the electric organ, electrocytes are intricately organized both in series and parallel. Their voltages and currents cumulatively contribute to the overall output: in series, electrocytes accumulate voltages, while in parallel, multiple rows combine their currents (Stoddard, 1999).

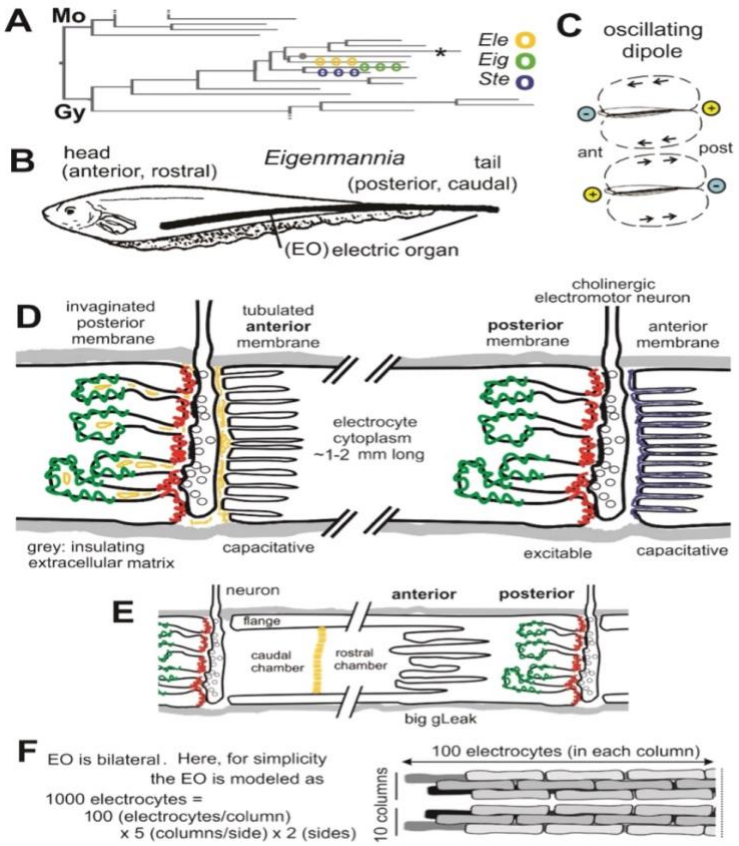

Figure 1.4.1 **Electric fish and their electrocytes. A**: A section of the cladistics scheme associated with electric fish Nav channels. Gy: the order *Gymnotiformes*; Mo: the order *Mormyriformes*. *Eigenmannia* (Eig) is closely related to *Sternopygus* (Ste) and *Electrophorus* (Eel). The asterisk represents *Brachyhypopomus*, and the grey dot represents Gymnotus, a vast genus with several EOD types. **B**: In *Eigenmannia*, the location of an electric organ with a fish length between 10 and 20 cm. **C**: *Eigenmannia*'s continuous wave EOD resembles an oscillating dipole. **D**: Schematic interpretations (not to scale) of an *Eigenmannia*-like electrocyte. **E**: Non-scale interpretive diagrams of an *Electrophorus*-like electrocyte. In diagrams D and E, the grey part: the electrocyte column's continuous insulating sheath. Gold part: a low-resistance, acellular supportive material. Blue: anterior membrane coating of negatively charged glycoproteins. Provisionally, we assume that this is also a feature of the fine anterior tubules of *Eigenmannia*. Red: AChR channels. Green: Nav channels. **F**: Electric organs are bilateral. To simplify the modeling of electric organs in various species, we use only 10 (2x5) columns of 100 electrocytes. Using 10 columns of 100 electrocytes for modeling would represent a juvenile *Eigenmannia* EO and be significantly smaller than an *Electrophorus* EO. (Figure created by Cathy Morris. Reproduced with permission).

1.4.2. *Electrophorus*

The genus *Electrophorus*, distinct from other Gymnotiform fishes, produces both weak and strong electric organ discharges (EOD) (Bauer, 1979; Cox et al., 1945). In *Electrophorus*, there are three types of electric organs: the main organ, Sachs' organ, and Hunter's organ. Sachs' organ and the posterior part of Hunter's organ generate weak EODs for navigation and communication. Conversely, the principal electric organ and anterior portion of Hunter's organ can emit up to 600 volts of EOD for predation and defense (Cox et al., 1945). These three electric organs exhibit distinct EODs owing to physiological differences, such as channel density (Traeger et al., 2017). However, these EODs share a common feature: they are monophasic, with head-positive peaks and a neutral baseline (Bennett, 1971; Catania, 2019). Initially, our research did not focus on the EOD's potency, but rather on its biophysical uniqueness and simplicity from a single electrocyte to the organ level. Hence, we concentrated on the cytomorphological characteristics (Gotter et al., 1998). We examined features analogous to *Eigenmannia*, as they offer a simpler model for understanding EODs. *Electrophorus* electrocytes are ribbon-shaped, approximately 20 mm in length, 1.5 mm in width, and 0.08 mm in height (Fig. 1.4.2). These cells are segmented into three sections: an anterior section without nerve connections, a posterior section with nerve connections, and an intervening cell body. The cell body is more compact than in *Eigenmannia* and functions as a resistor. Uniquely in *Electrophorus*, the anterior part of the electrocyte features wide flanges and numerous potassium leak channels (Fig. 1.4.1 E). Yet, these cells lack a particular potassium channel found in *Eigenmannia*, indicating that even minor structural differences can significantly impact the EOD shape.

The spaces between the electrocytes in *Electrophorus*, the electric eel, differ markedly from those in *Eigenmannia* (Fig. 1.4.1 E). In *Electrophorus*, these gaps are larger and comprise two sections, termed the caudal and rostral chambers (Luft, 1957). These chambers are filled with a conductive gel-like substance, facilitating electric signal transmission (Keynes and Martins-Ferreira, 1953). Due to the lack of direct experimental data on their electrical resistance, we estimate that the gap resistance in *Electrophorus* ($R_{gap,Eel}$) is considerably lower than in *Eigenmannia*, potentially tenfold less. This reduced resistance contributes to *Electrophorus*'s potent electric shocks. Moreover, *Electrophorus*'s electrocytes have a broader cross-sectional

area, yet they are shorter than those in *Eigenmannia*. This suggests that their internal resistance ($R_{gap,Eig}$) is also lower, estimated to be approximately five times less than in *Eigenmannia*.

A key feature of *Electrophorus*' electrocytes is their isolated structure (Fig. 1.4.1 E). Each electrocyte is encased in an insulating layer of connective tissue. This insulation is vital as it prevents the strong electric currents generated by the fish from causing self-harm. The electrocytes, anchored to this connective tissue, also guide the flow of electric current along the organ's length (Luft, 1957). This architecture enables *Electrophorus* to produce intense electric shocks and shields the fish from its own powerful discharges, resembling a biological taser (Wolfe, 1988).

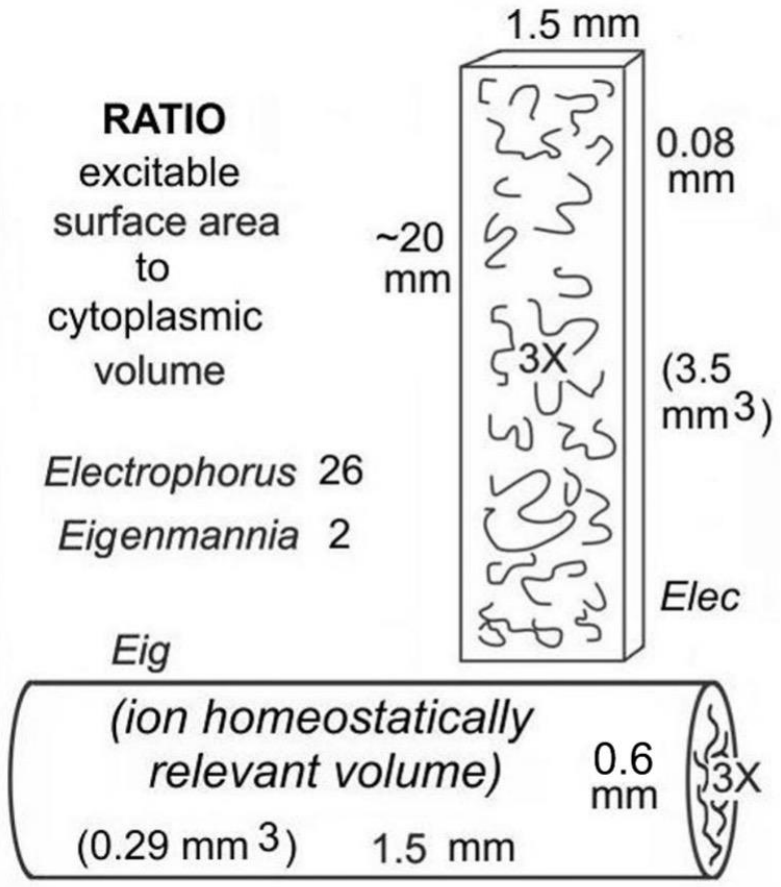

Figure 1.4.2 **Illustrations of *Eigenmannia*'s and *Electrophorus*'s electrocytes.** (Figure created by Cathy Morris. Reproduced with permission).

1.5. Posterior Anterior Charge Difference Model (PA-CD)

In electrophysiology, the study of the electrical properties of biological cells and tissues, choosing appropriate models is essential to understand how cells regulate their ion levels. A fundamental concept here is the "Pump Leak Mechanism" (Tosteson and Hoffman, 1960; Kay and Blaustein, 2019), which elucidates how cells maintain ion balance. Building on this, Fraser and Huang developed the Charge Difference (CD) technique (Fraser and Huang, 2004). This approach is straightforward yet effective, because it computes the total ions moving across a cell's membrane to determine its electrical potential (Fraser and Huang, 2004; Morris et al., 2022). Traditionally, charge difference models have been elementary, focusing solely on the cell's membrane without distinguishing its various components (Fraser et al., 2011). However, Fraser and his team enhanced this model to include t-tubules, creating a hybrid model. The t-tubule component of the model is one-dimensional, considering the movement of ions along a single axis.

Our research initially utilized this one-dimensional model, but we identified certain limitations, especially the assumption of a uniform ion environment across the cell membrane. To overcome these, we developed a new dynamic model named the Posterior Anterior Charge Difference (PA-CD) model. This model, incorporating insights from earlier studies, considers a cell as having two different membrane areas (Dijkstra et al., 2016; Morris et al., 2022). It simulates a one-dimensional generic polarized cell with two distinct membrane regions, calculating cytoplasmic ion fluxes (membrane-permeant and membrane-impermeant ions) using one-dimensional Nernst-Planckian diffusion and drift. An upcoming discussion will further elucidate key concepts of the PA-CD model.

1.5.1. Ion homeostasis

Homeostasis, a term coined in 1932 by Walter Cannon (Cannon, 1963; Billman, 2020), refers to the physiological concept of a stable internal environment, originally proposed by Claude Bernard in the 19th century (Billman, 2020). Ion homeostasis and equilibrium are distinct concepts. Ion homeostasis is the process by which an animal cell regains its set point after a temporary ionic disturbance, while equilibrium refers to a system's condition where competing influences are balanced, resulting in no net change. Formally defined, the set-point represents the steady state for intracellular ions ($[K^+]_i$, $[Na^+]_i$, $[Cl^-]_i$), transmembrane potential (MP), and cell volume (Vol_{cell}). This set-point is adaptable, allowing systems to adaptively function in varying environmental conditions (Morris et al., 2022).

In achieving ion homeostasis, evolution has selected an optimal ion homeostatic set-point for different cell types, characterized by the specific ion homeostatic apparatus: an optimal amount of water-permeable membrane, standard maximum pump strength, a range of ion-selective leak permeabilities, and a defined number of valences for impermeant ions (Donnan effecter in this model). Employing these cellular components, the system maintains the determined ion homeostatic set-point through inherently functioning active and passive feedback mechanisms without specifically monitoring MP, $[ions]_i$, or Vol_{cell}. The active feedback sensors respond to changes in intracellular sodium concentration, while the passive feedback sensors react to variations such as shifts in neutrality and osmotic balance (Morris et al., 2022). In our study's initial phase, we assumed ion homeostasis without detailed mechanistic insight. Consequently, we formulated ion homeostasis based on the Pump-leak Donnan process (P-L/D), which will be explained further below.

1.5.2. Pump-leak Donnan

Pump-leak Donnan is a process discussed in detail in Morris et al. (2022), in which cellular ion homeostasis is regulated by different cellular components. A mechanistic discussion of this concept follows and is summarized in Fig. 1.5.1.

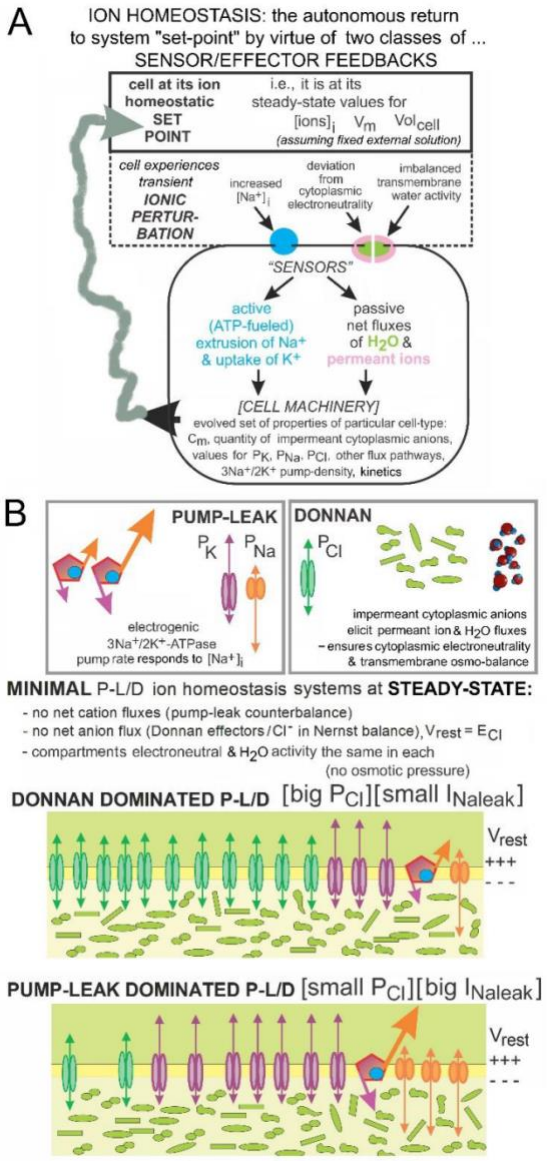

Figure 1.5.1 **P-L/D ion homeostatic at steady state.** See List of abbreviations. (Morris et al., 2022)(reproduced with permission)

1.5.2.1. Cellular components

Cellular components critical to electrophysiology, including cell type-specific membrane area, impermeant anion amount (Donnan effector amount), permeability, pump density, intracellular sodium concentration, and extracellular potassium concentration, are all parameters shaped by evolution. As shown in Fig. 1.5.1 B, the sodium-potassium ATPase is an electrogenic pump. This pump's primary role is to transport sodium and potassium ions across the membrane in a ratio of three sodium ions outwards for every two potassium ions inwards. It ensures a higher concentration of sodium ions outside the cell and a higher concentration of potassium ions inside the cell. Additionally, it is an active cellular transport mechanism requiring energy. Meanwhile, leak channels permit ion movement across the membrane, thus impacting the membrane potential by modifying the leak permeability of specific ions. Conversely, cytoplasmic Donnan effectors neutralize intracellular cations and maintain osmotic balance. At steady state, electrogenic pumps balance cation leaks, Donnan effectors and Cl^- reach Nernst equilibrium, resulting in no net ion fluxes, electroneutrality, and equal osmotic pressure across the cellular membrane (Morris et al., 2022).

Notably, the ratio between sodium leak permeability and potassium leak permeability has significant electrophysiological implications. Lower ratios yield a hyperpolarized resting membrane potential (V_{rest}), while higher ratios result in a depolarized one. After establishing V_{rest} via P_{Na} and P_K, the resting state's intracellular anion concentrations are fixed. In a minimal state, indicating entirely passive Cl^- transport, $E_{Cl} = V_{rest}$ (Morris et al., 2022). Further details will be provided in the methods Section 3.1.12. Although the circuit model presupposes ionic homeostasis, our dynamic model suggests that cells achieve such homeostasis at steady state through the differing influences of pumps, leaks, and Donnan effectors, varying depending on the cell type. This topic will be elaborated on subsequently.

1.5.2.2. Pump-Leak dominated /Donnan dominated.

Cells will achieve cellular homeostasis either through Pump-Leak dominant or Donnan dominant mechanisms (Fig.1.5.1 B). For instance, neurons typically restore ionic homeostasis in a Pump-Leak dominated manner, while skeletal muscles do so through Donnan dominance. This is dictated by the differential leak permeabilities towards various ions across the membrane at steady state, as shown in Table 1.1.

Table 0.1 **Mechanism to achieve ion homeostasis through either Pump-Leak or Donnan dominant fashions.**

Permeabilities\Dominance	**Pump-Leak**	**Donnan**
$P_{Cl} >> P_K >> P_{Na}$		Dominated
$P_K >> P_{Na} > P_{Cl}$	Dominated	

Previous research indicates that healthy skeletal muscle requires a Donnan dominated steady state, characterized by a low P_{Na} and a large P_{Cl}. Consequently, skeletal muscles are mostly in a steady state, rendering them less responsive to stimulation. With no net ion flux across the membrane, steady-state Na^+ extraction ($I_{NaKpump}$) matches steady-state Na^+ influx ($I_{Na,leak}$). This low-impedance, Donnan-dominated steady state is a cost-effective method to achieve ion homeostasis. In contrast, neurons exemplify a Pump-Leak-dominated stable state. Their high P_{Na} and low P_{Cl} at steady state support their specialized function as highly excitable, message-transmitting cells. Thus, this high impedance, Pump-Leak-dominated steady state is energetically demanding (Morris et al., 2022). Our PA-CD model in this thesis focuses primarily on the pump leak dominant steady state.

1.5.2.3. Active and passive feedback.

In response to ionic perturbations, the ion homeostasis process "blindly" returns cells to a steady state. Such a blind-to-system process means that the deviations of internal ions ($[K^+]_i$, $[Na^+]_i$, and $[Cl^-]_i$), transmembrane potential (MP), and cell volume (Vol_{cell}) are not detected and responded to (Fig. 1.5.1 A). This process is mediated through active and passive sensor feedback mechanisms present in the P-L/D process, which is demonstrated in Fig. 1.5.1 A.

Active sensors identify changes in intracellular sodium concentration and adjust Na^+ efflux and K^+ uptake of ATP-fueled $3Na^+/2K^+$ pumps. Passive feedback sensors recognize deviations, such as shifts in neutrality and osmotic balance. They are regulated by Donnan effectors and P_{Cl} in a water-permeable membrane equipped with P_{Na} and P_K, acting to counter any osmotic imbalance and departure from cytoplasmic neutrality (Morris et al., 2022).

1.5.3. Endogenous electric fields (EEF)

Endogenous electric fields (EEFs) are natural electrical fields produced by cells. The first EEF was identified by Jaffe and Nuccitelli in 1974 during their research on electric currents near living cells. Each cell type generates a unique transmembrane potential, contributing to these electric fields (Nuccitelli and Jaffe, 1974). While endogenous electric fields have been recognized for decades, the widespread zero-dimensional model, which overlooks cytomorphology and presumes a uniform spatial distribution of ion permeability, has hindered a deeper understanding of the mechanisms and origins of such electric fields. Despite initial waning interest following the advent of single-channel recording and molecular cloning of ion channels, recently, research has intensified due to discoveries that EEFs play a critical role in complex physiological processes such as regeneration (nerve/tissue) (Ryan et al., 2021) and electrotaxis (e.g., cancer cell migration) (Funk, 2015), which are highly relevant to human health.

Pietak and Levin (2017) modeled the interaction between EEFs and reaction-diffusion in gap-junction coupled cells with varying P_{Na}:P_K ratios. However, they used a 'forced cycle' test simulation, creating a transient perturbation that leads to depolarization followed by hyperpolarization of MP. The system fails to achieve a steady state after this perturbation.

Consequently, to develop a foundational model for EEF, we suggest that EEFs arise from the ion homeostatic process in cells with non-uniformly distributed ion homeostatic machinery, implying posterior/anterior asymmetries are regulated differently across tissues. Our goal is to create tools for a more comprehensive understanding of ion homeostasis in spatially polarized cells.

2. Equivalent Circuit Model for *Eigenmannia* and *Electrophorus* EOD

2.1. Development of the equivalent circuit model

2.1.1. The equivalent circuit for *Eigenmannia* and *Electrophorus*

The Bennett equivalent electrical circuit served as the basis for our model (Bennett, 1971). The posterior membrane of these two fishes exhibits similar mechanisms. It is a development of the previous model Epm (excitable posterior membrane) (Joos et al., 2018). The transmembrane currents in Epm are Ohmic. However, this equivalent electrical circuit uses the Goldman-Hodgkin-Katz (GHK) model as the driving force for all the transmembrane currents to make the excitable cells more resilient to the perturbations (Kotler et al., 2022) .
Moreover, the types and functions of EODs differ between *Eigenmannia*-type to *Electrophorus*-type. The main distinctions are their anterior end morphology and the size of electrocytes. Moreover, this equivalent circuit model assumes ion homeostasis. Thus, there will be perfect reciprocal transport: for every Na^+ ion that enters, one Na^+ ion will be pumped out. At the anterior end, diverse flux mechanisms could counteract pump-induced local polarisation. For the posterior end, Ion channel currents must precisely balance every three incoming Na^+ with two outgoing K^+ for pumping across the posterior end.

.

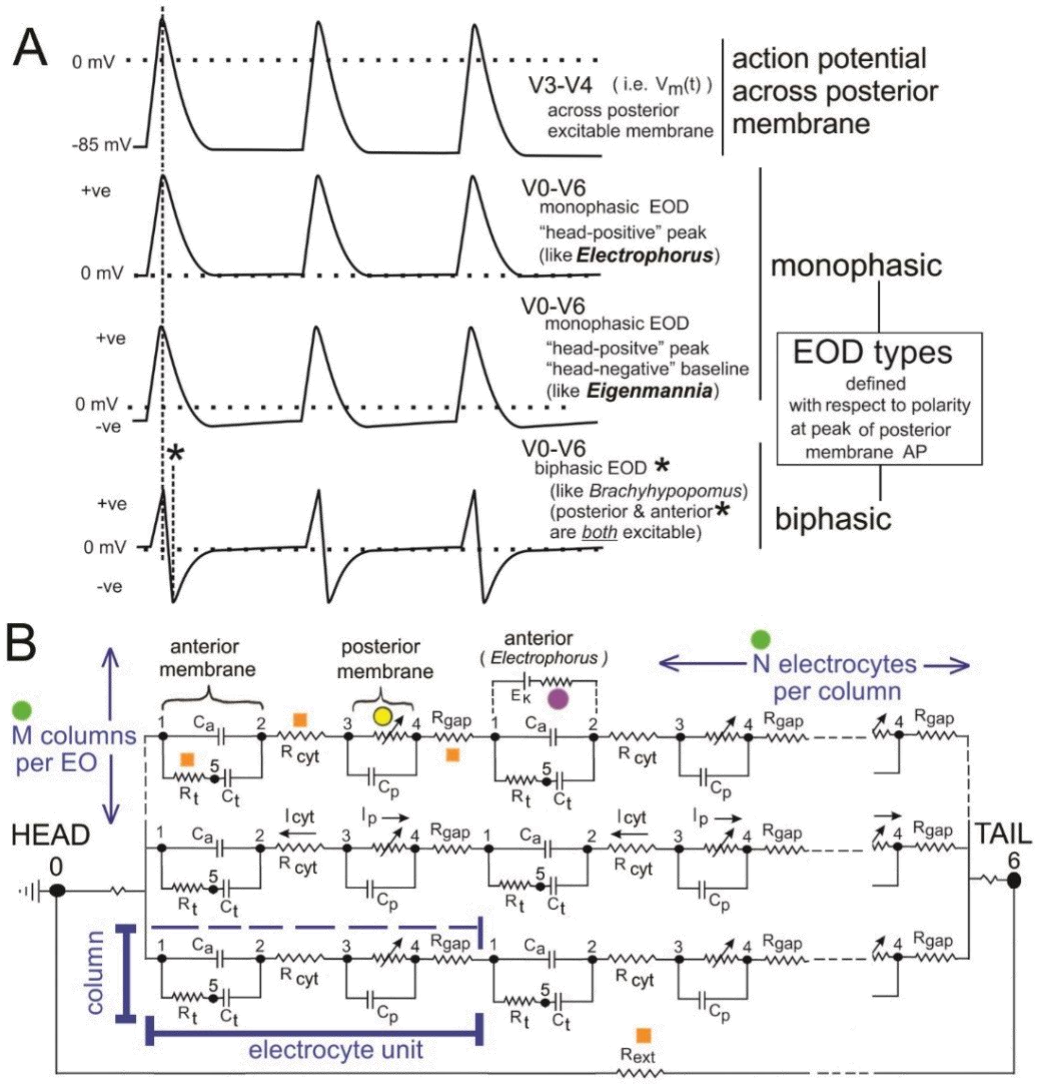

Figure 2.1.1 **Illustration of the action potential, different shapes of electric organ discharge ,and equivalent circuit for *Eigenmannia* and *Electrophorus*. A**. The hand-drawing action potentials show APs on the posterior electrocyte membrane, with a specific action potential measured as the voltage difference between V3 and V4 in the equivalent circuit. The head-to-tail EODs can be seen from the outside and are measured as V6-V0. *Electrophorus* and *Eigenmannia* EODs are monophasic with head-positive peaks. The *Electrophorus* EOD has a neutral baseline, whereas the *Eigenmannia* EOD has a head-negative baseline. Some gymnotids, such as *Branchyhypopomus*, have excitable posterior and anterior membranes, and produce biphasic EODs.(Bennett, 1971; Markham, 2013) **B**. The generic EO equivalent circuit is used for *Eigenmannia*-type electrocytes (lower left, blue-dash brackets) or *Electrophorus*-type electrocytes with the anterior membrane changed, as shown by the purple dot in the top column. Each electrocyte has a cholinergic excitable posterior membrane, indicated by the variable resistor (arrow), as previously described (Joos et al., 2018). The multitude of tubules in the anterior membrane is represented (lumped) as C_t in series. C_t represents the number of tubules in the anterior membrane in series. The formal representation of fish-skin resistance (between V0–V1 and V5–V6) shows that electrodes for measuring head-to-tail EODs placed outside the fish. (Figure created by Cathy Morris. Reproduced with permission)

The Fig. 2.1.1 B shows the electric organ circuit. Applying Kirchhoff's voltage and current rules to this circuit, the voltage across an electrocyte is given by:

$$\begin{aligned} V_e &= V_1 - V_4 = (V_1 - V_2) + (V_2 - V_3) + (V_3 - V_4) \\ &= -V_a - I_{cyt} R_{cyt} + V_p \end{aligned} \tag{1}$$

V_a is the membrane potential difference at the anterior end, while V_p is the membrane potential difference at the posterior end, with the convention that the voltage difference is calculated as $V_{in} - V_{out}$. I_{cyt} is the cytoplasmic current and R_{cyt} is the cytoplasmic resistance.

For each column, we have N electrocytes. To simplify the calculation, we assume that there are N gaps in each column. By the Kirchhoff 's voltage rule, we have:

$$NV_e - NR_{gap} I_{cyt} = MI_{cyt} (R_{ext} + R_{hsk} + R_{tsk}) \tag{2}$$

R_{gap} are the tubular and gap resistance. R_{ext} represents the exterior resistance. R_{hsk} is the head's skin resistance, while R_{tsk} is that of the tail. The parameter values are in the Table. 2.2.

From Eq. (2), V_e can be also given by:

$$V_e = R_{gap} I_{cyt} + \frac{M}{N} (R_{ext} + R_{hsk} + R_{tsk}) I_{cyt} \tag{3}$$

Thus, from Eqs. (1) and (3) the cytoplasmic current is:

$$I_{cyt} = \frac{V_p - V_a}{R_{cyt} + R_{gap} + \frac{M}{N}\left(R_{ext} + R_{hsk} + R_{tsk}\right)} \tag{4}$$

For the cytoplasmic current I_{cyt}, when current flows from posterior to anterior, the current is in the positive direction. Our model is a close circuit (Fig. 2.1.1 B), when the cell achieves ion homeostasis, the total anterior, and posterior transmembrane current, the cytoplasmic current,

and the external current should be equal. Furthermore, the direction of external current is opposite to the cytoplasmic current, from head to tail.

In the equivalent model, we compute the EOD by the ohmic relationship as an important feature, i.e., type, shape, and amplitude, to verify if the model is valid. As shown in Fig. 2.1.1 A, both *Eigenmannia*-type and *Electrophorus*-type EOD are monophasic. The *Eigenmannia*-type EOD has a head-positive peak and head-negative baseline. However, the *Electrophorus*-type EOD has an almost neutral baseline. The head-to-tail EODs can be seen from the outside and are measured as V6-V0. The EOD voltage is :

$$V_{EOD} = MI_{cyt}R_{ext} \tag{5}$$

From Eqs. (4) and (5), the EOD voltage can be given as:

$$V_{EOD} = M\frac{V_p - V_a}{R_{cyt} + R_{gap} + \frac{M}{N}\left(R_{ext} + R_{hsk} + R_{tsk}\right)}R_{ext} \tag{6}$$

The equivalent circuit output for a given electric organ size, as determined by column M and the number of electrocytes in each column N. R_{ext} represents the exterior resistance. As indicated by the of fish skin resistance, R_{hsk} is the head's skin resistance, while R_{tsk} is that of the tail. R_t and R_{gap} are the tubular and gap resistance.

2.1.2. The anterior compartment of *Eigenmannia* and *Electrophorus*

Table 2.1 shows the compartment feature of *Eigenmannia* and *Electrophorus*. The anterior of *Eigenmannia* is a pure capacitor. The membrane potential of *Eigenmannia*'s anterior end is given by:

$$\frac{dV_a}{dt} = \frac{1}{C_a}\left(\frac{V_p - V_a}{R_{cyt} + R_{gap} + \frac{M}{N}\left(R_{ext} + R_{hsk} + R_{tsk}\right)} - \frac{V_a - V_t}{R_t}\right) \tag{7}$$

However, for *Electrophorus*, the anterior end has a large potassium leak I_{La}. The anterior membrane potential of *Electrophorus* is given by:

$$\frac{dV_a}{dt} = \frac{1}{C_a}\left(\frac{V_p - V_a}{R_{cyt} + R_{gap} + \frac{M}{N}\left(R_{cxt} + R_{hsk} + R_{tsk}\right)} - \frac{V_a - V_t}{R_t} - I_{La} \right) \tag{8}$$

With:

$$I_{La} = P_{La} F \left(\frac{FV_a / RT}{1 - e^{-zFV/RT}} \right) \left[[K]_{in} - [K]_{out} e^{-FV/RT} \right] \tag{9}$$

P_{La} is anterior leak potassium permeability. If I_{La} is positive, the current will flow out of the cell, and vice versa.

Table 2.1 **The compartment features of the electrocytes of *Eigenmannia* and *Electrophorus*.**

	Eigenmannia	***Electrophorus***
Anterior	Pure capacitor	Capacitor
		Potassium leak channels
Posterior	Voltage-gated Sodium Channel	Voltage-gated Sodium Channel
	Delayed Rectifier Potassium Channel	Delay-Rectifier Potassium Channel
	Generic Leak	Generic Leak
	Acetylcholine Receptors	Acetylcholine Receptors

Both *Eigenmannia* and *Electrophorus* have narrow blind-ended tubular invaginations at the anterior end, which increases the membrane area. The invaginations of electrocytes resemble those of muscle T-tubules (Bennett,1971; Luft,1998). These tubulars can be regarded as capacitors in series with a high resistance, which represent negatively charged glycoproteins occupying tubular lumens. The tubular voltage of both *Eigenmannia* and *Electrophorus* are:

$$\frac{dV_t}{dt} = \frac{1}{C_t}\left(\frac{V_a - V_t}{R_t}\right) \quad (10)$$

2.1.3. The posterior compartment of *Eigenmannia* and *Electrophorus*

Similar characteristics define the posterior membrane of *Eigenmannia* and *Electrophorus*. This equivalent circuit model accounts for the subsequent generation of action potentials. Other circuit components are parameterized based on available electrocyte cytomorphology. The expression of acetylcholine receptors (AChR) and voltage-dependant or gated sodium (Nav) channels indicates that the posterior face is the only location where sodium can enter and where action potentials originate. The posterior membrane potentials of both *Eigenmannia* and *Electrophorus* are given by:

$$\frac{dV_P}{dt} = \frac{1}{C_p}\left(\left(-I_{Na} - I_K - I_{leak} - I_{stim}\right) - \frac{V_{p-} V_a}{R_{cyt} + R_{gap} + \frac{M}{N}\left(R_{ext} + R_{hsk} + R_{tsk}\right)}\right) \quad (11)$$

I_{Na} is the transient currents that flow through Nav channels. I_k represents the delayed rectifier potassium channel. I_{leak} is the generic leak current. I_{stim} is the stimulus current that initiates the action potential and is discussed in Section 2.1.3.3. If the transmembrane currents, like I_{Na}, I_K, I_{leak}, I_{stim}, are positive, which signify that the currents flow out of the cell, and vice versa.

2.1.3.1. Voltage-gated channels:

Sodium voltage gated channel and delayed rectifier potassium channel are voltage-gated channels. Voltage-dependent sodium current is characterised by a transient inward Na^+ flux that depolarizes the cell. Persistent sodium current is present during the resting state of membrane potential. It gradually depolarizes the membrane potential until the next action potential generation threshold. In our minimal equivalent circuit model, we exclude the persistent sodium current to let *Electrophorus* have a more direct current like membrane potential at the anterior end, this is in accordance with a previous study on the computational model for *Electrophorus*

(Xu et Lavan's). In our model, we give a fixed PNa_{max}, which can maintain high frequency firing for both kinds of fish. This simplifies the model.

I_{Na} is given by:

$$I_{Na} = P_{Namax} Fm^3 h \left(\frac{FV_p/RT}{1 - e^{-zFV/RT}} \right) \left[[Na]_{in} - [Na]_{out} e^{-FV/RT} \right] \quad (12)$$

P_{Namax} is the maximum membrane sodium permeability through a sodium voltage-gated channel. m is the activation/deactivation gating variable for the H-H Na^+ channel, while h is the inactivation/recovery gating variable.

Furthermore, a delayed rectifier potassium is essential for maintaining the action potential of electrolytes at a high frequency.

I_K is given by:

$$I_K = P_{Kmax} Fn^2 \left(\frac{FV_p/RT}{1 - e^{-zFV/RT}} \right) \left[[K]_{in} - [K]_{out} e^{-FV/RT} \right] \quad (13)$$

P_{Kmax} is the maximal membrane permeability of potassium ions through the voltage-gated delay rectifier channel. Potassium delay rectifier channels work in an H-H pattern, and n is the variable for the delayed rectifier K^+ channel activation/deactivation gate. The power for n is not universal; the power depends on the model used and channel characteristics. As suggested by Dijkstra et al. (2016), we choose for the second power.

In Eqs. (12) and (13), the non-dimensional gating parameters j = m, h, and n are subject to equations of the form:

$$\frac{dj}{dt} = \alpha_j (1 - j) - \beta_j j \quad (14)$$

With

$$\alpha_j = \kappa_{\alpha j} e^{\eta_{\alpha j} V} \quad (15)$$

$$\beta_j = \kappa_{\beta j} e^{\eta_{\beta j} V} \tag{16}$$

m and n correspond to gate activation and deactivation, and h to inactivation and recovery from inactivation. α_j and β_j are voltage dependent rate constant (Joos et al., 2018). The pre-factors $K_{\alpha j}$ and $K_{\beta j}$ and the exponential factors $\eta_{\alpha j}$ and $\eta_{\beta j}$ are given in table 2.2. However, as mentioned in the Epm, to have the functional form of squid axon, the kinetic variable β_h is described as:

$$\beta_h = \frac{3.33}{\exp\left(-\frac{V+30}{9}\right)+1.0} \tag{17}$$

2.1.3.2. Generic leak channel at posterior end

The generic leak channel at the posterior end that is important for action potential repolarization.

The generic leak current (I_{leak}) is given by:

$$I_{leak} = P_{leak} F \left(\frac{FV_p/RT}{1 - e^{-zFV/RT}} \right) \left[[K]_{in} - [K]_{out} e^{-FV/RT} \right] \tag{18}$$

P_{leak} is the Leak permeability at the posterior end. For both *Eigenmannia* and *Electrophorus*, the generic potassium leak current is present at the posterior end.

2.1.3.3. The stimulus current initiates the action potential.

Pacemaker signals initiated in the brain control the periodic release in the synapse of vesicles containing the neurotransmitters acetylcholine (ACh). They diffuse to the postsynaptic membrane which is the posterior end of the electrocyte and trigger the opening of acetylcholine receptor channels (AChR). The resulting net influx of positive ions I_{stim} initiates the action potentials producing the EODs. As stated in Epm, a description of ion permeation through AChR based on electro diffusion enables the independent calculation of Na^+ and K^+ fluxes (Joos et al., 2018).

$$I_{stim} = syn(t)\left(I_{AChR(Na)} + I_{AChR(K)}\right) \quad (19)$$

The standard pulsatile stimulus shape, syn(t), consists of three segments: a linear rise for 0.05 ms, a plateau for 0.200 ms and an exponential decay to zero (Joos et al., 2018).

The sodium and potassium ions passing through the AChR channels can be given by:

$$I_{AChR(X)} = P_{AChR(X)} Fz\left(\frac{zFV_p/RT}{1 - e^{-zFV/RT}}\right)\left[[X]_{in} - [X]_{out} e^{-zFV/RT}\right] \quad (20)$$

Where X can represent either Na^+ or K^+, F is the Faraday constant, R is the gas constant, and z is the ionic valence. The firing frequencies of electrocytes depend on the Syn(t). The ratio of $P_{AChR,K}/P_{AChR,Na}$ is 1.11 and $P_{AChR,Na}$ was selected to provide a suitable size depolarization of the posterior membrane potential to initiate an action potential.

Table 2.2 **Parameter values of circuit model.**

	Unit	***Eigenmannia***	***Electrophorus***
M	-	10	10
N	-	100	100
T	K	293.15	293.15
R	J / mol•K	8.3144621	8.3144621
F	J/K	1.3806488×10^{-23}	1.3806488×10^{-23}
$\mathbf{R_{cyt}}$	MΩ	0.004255	0.000851
$\mathbf{R_{gap}}$	MΩ	0.5	0.05
$\mathbf{R_{ext}}$	MΩ	0.03	0.03
$\mathbf{R_{hsk}}$	MΩ	1×10^{-5}	1×10^{-5}
$\mathbf{R_{tsk}}$	MΩ	1×10^{-5}	1×10^{-5}
$\mathbf{R_t}$	MΩ	100	100
$\mathbf{C_a}$	nF	18	180

C_p	nF	48	48
C_t	nF	117	1170
P_{leak}	mm^3/s	0.00007	0.00007
P_{Namax}	mm^3/s	0.015	0.015
P_{Kmax}	mm^3/s	0.03	0.03
P_{La}	mm^3/s	0	0.02625
NaV			
γ		0.02	0.02
kαm	ms^{-1}	7.6	7.6
kβm	ms^{-1}	0.6894	0.6894
ηαm	mV^{-1}	0.0037	0.0037
ηβm	mV^{-1}	-0.0763	-0.0763
kαh	ms^{-1}	0.0081	0.0081
ηαh	mV^{-1}	-0.06803	-0.06803
KV delayed rectifier			
kαn	ms^{-1}	1.209	1.209
kβn	ms^{-1}	0.4448	0.4448
ηαn	mV^{-1}	0.03792	0.03792
ηβn	mV^{-1}	-0.01552	-0.01552
AChR			
$P_{AChR,Na}$	mm^3/s	0	0.00025
$P_{AChR,K}$	mm^3/s	0	0.0002775

2.2. *Eigenmannia*

2.2.1. The mechanisms of *Eigenmannia*'s dipole-oscillator-like electric organ discharges (EODs).

The anterior end of *Eigenmannia*'s electrocytes acts as a pure capacitor, while the cholinergic posterior end has Nav, Kv, and leak channels. Acetylcholine receptor current depolarizes the posterior membrane (Fig. 2.2.1 A). When the posterior membrane potential V_P reaches the activation threshold of the Nav, the activation gate (m) of voltage-gated sodium channel (Nav) opens quickly. Nav is in an open state. The open probability of Nav is defined as m^3h. m^3 is the probability that any of the three gating subunits is active. The factor h means that the probability of inactivation (Fig. 2.2.1 D). Consequently, this sodium influx depolarizes the membrane (Fig. 2.2.1 E).

However, the delayed rectifier channels (Kv) with n-gates have open probability n^2 and respond more slowly than the Nav's activation gates. Therefore, when the membrane is depolarized, the Kv opens after the Nav (Fig. 2.2.1 D). The efflux of potassium (Fig. 2.2.1 E) causes repolarization of the membrane. Following repolarization, Nav is inactivated, however, Kv remains open. During the hyperpolarization phase, the Kv channels remain open after the membrane voltage reaches its resting level. At posterior resting potential, Nav is nearly closed, featuring an open h-gate and closed m-gates (Fig. 2.2.1 D). Furthermore, a generic potassium current is consistently present (Fig. 2.2.1 E), determining the posterior resting membrane potential.

Since the anterior end is purely capacitive, it receives the charge from the posterior end and keeps charging and recharging (Fig. 2.2.1 B). Thus, the resultant EODs of the whole electric organ have a head-positive peak and a head-negative baseline. When $V_a > V_p$, the EOD is head negative (Fig. 2.2.1 C). In comparison, when $V_a < V_p$, the EOD is head positive (Fig. 2.2.1 C).

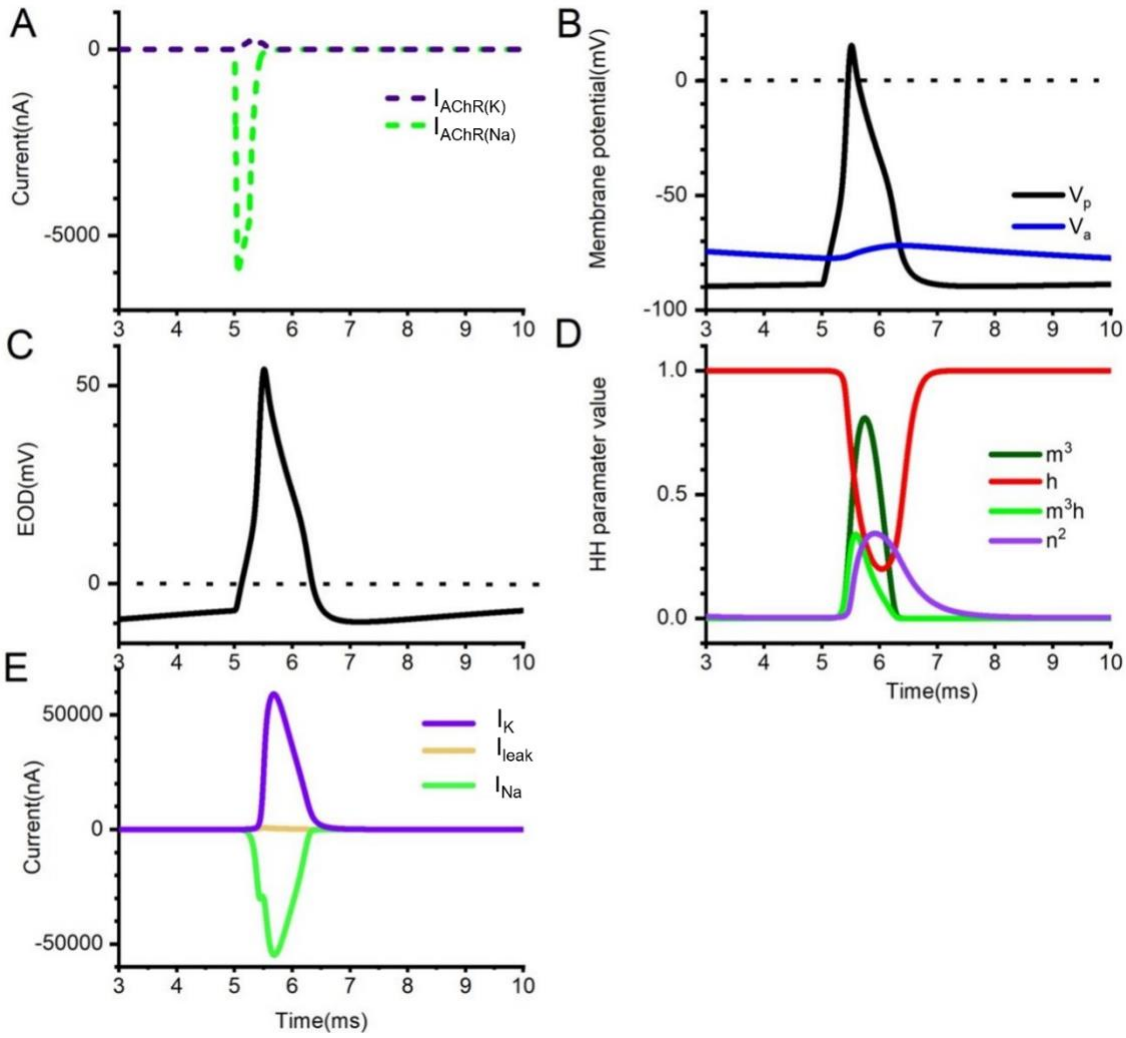

Figure 2.2.1 ***Eigenmannia*-type EOD at 200 Hz. A**. Na^+ and K^+ AChR current. **B**. The membrane potential of the anterior and posterior ends. **C**. At 200 Hz, the developed circuit model with the Goldman-Hodgkin-Katz (GHK) driving force can provide an *Eigenmannia*-type EOD with a positive peak and a negative baseline. The reference line is 0 mV. **D**. Hodgkin–Huxley gating variables m, h, and n. m is the Nav activation variable; h is for the Nav inactivation. Variable n is Kv activation variable. The transient sodium current is determined by m and h. The value of delayed rectifier potassium current is determined by the n^2 Current at the posterior end **E**. I_{Na}: Transient sodium current; I_K: delayed rectifier potassium current: I_{leak}: generic leak current. I_{leak} is always persistent. Notably, the I_{leak} is relatively minor compared with other currents.

2.2.2. Equivalent circuit predicted *Eigenmannia*-type EODs can undergo high frequency firing.

Eigenmannia continuously generates weak electric organ discharges (EODs) at a frequency ranging from 200 to 500 Hz for navigation and communication in the darkness (Scheich, 1977). We examine the equivalent circuit model with varied frequencies to evaluate its capacity for generating *Eigenmannia*-type electric organ discharges (EODs) at high frequencies and to explore the electrocytes' discharging and recharging behavior.

When the fundamental frequency of *Eigenmannia* (250–500 Hz) increases, all EODs show a positive peak and a negative baseline (Fig. 2.2.2). Notably, with increasing frequency, the peak and the trough of the EODs get more polarized, and the amplitude diminishes (Fig. 2.2.3 B). A previous study (Joos et al., 2018) suggested that Nav channel density should be increased at higher frequency to keep the amplitude of EOD constant. In our circuit model, the Nav channel density is constant, and it is strong enough to trigger an action potential from 200 to 500 Hz. However, it is insufficient to keep the amplitude constants with increasing frequency.

As frequency increases while P_{Namax} and P_{Kmax} remain constant, the peaks of the posterior action potentials become less depolarized, and the troughs become more depolarized (Fig. 2.2.3 A). In this case, the number of oscillations during a given time increases as the frequency increases. At higher frequency, the accelerated activation and inactivation speeds of Nav and Kv reduce the time for membrane depolarization by Nav and repolarization by Kv, causing a more polarized peak and a more depolarized trough in the action potentials.

In addition, a generic leak current is always present to drive the resting membrane potential to the leak potential. We make the leak potential was made equal to the potassium leak potential. We set the leak potential equal to the potassium leak potential. Consequently, a posterior action potential with a higher frequency allows less time for the generic leak channel to drive membrane potential to E_k, leading to a more depolarized resting state. Since the anterior end is a pure capacitor, the anterior end becomes more depolarized with increasing frequency. Consequently, the amplitude diminishes.

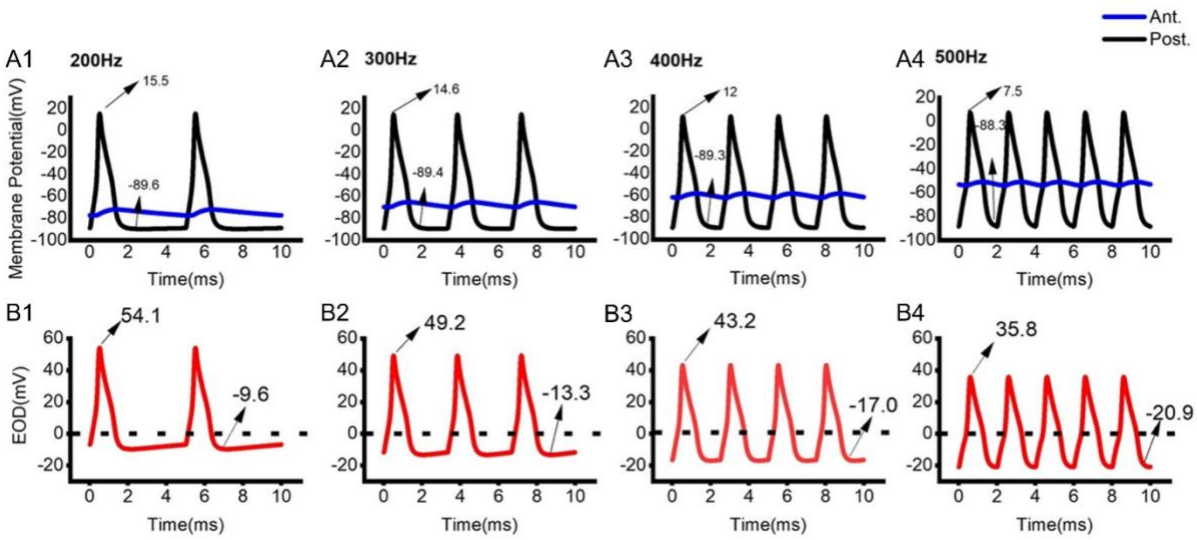

Figure 2.2.2 ***Eigenmannia*-type EODs and membrane potential at different frequency (from 200 Hz to 500 Hz).** The only variation is frequency. **A1-A4:** Membrane potentials from 200Hz to 500Hz **B1-B4:** EODs with frequencies from 200Hz to 500Hz.

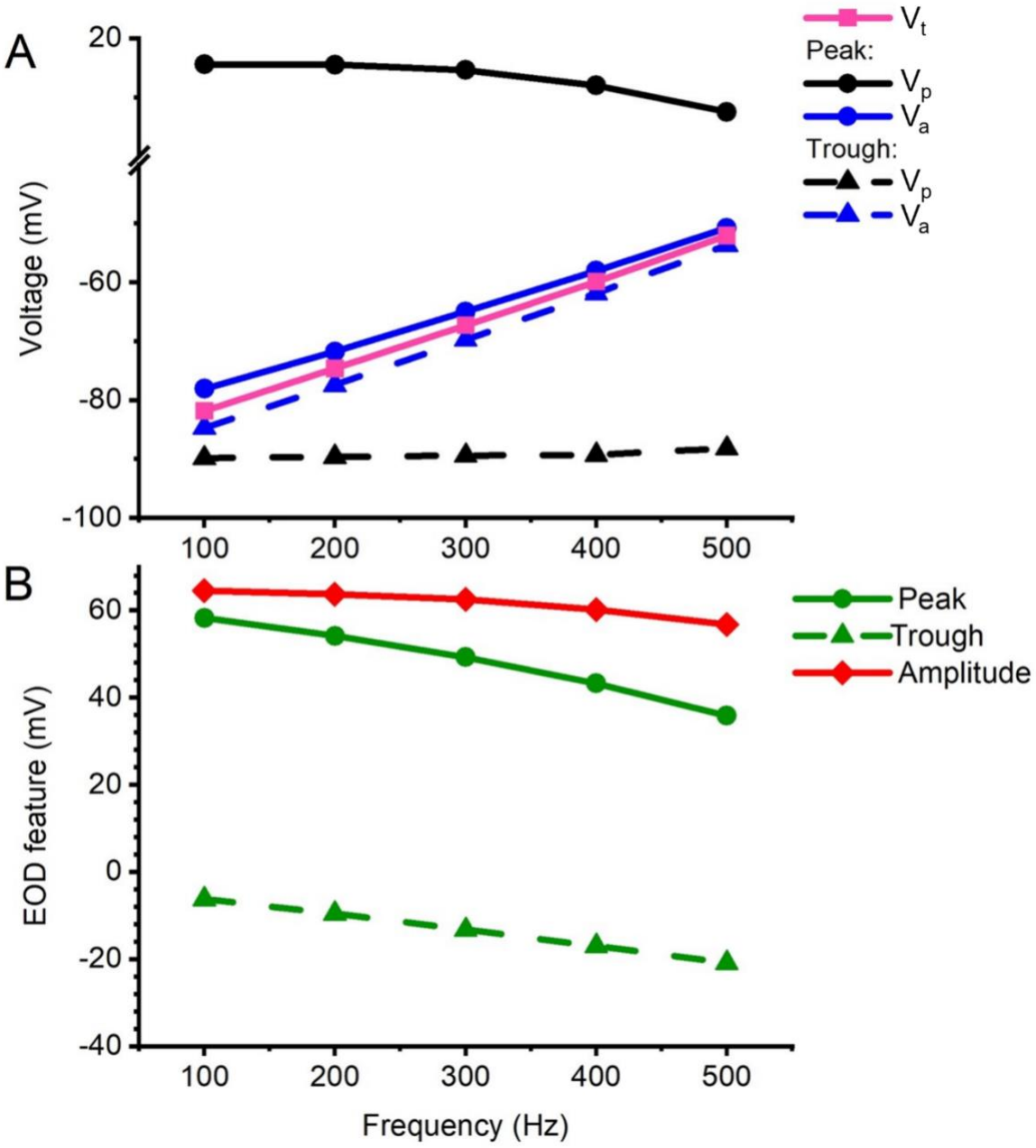

Figure 2.2.3 ***Eigenmannia*-type membrane potential and EOD feature at different frequencies. A**: The peak and the trough of V_a increase with increasing frequency. V_t follows the change in V_a. The peak and the trough of V_p decrease with increasing frequency. **B**: As frequency increases, the peak of the EOD decreases, the trough becomes polarized, and the amplitude diminishes.

To evaluate how P_{Namax} influences EOD magnitude of *Eigenmannia*-type EOD, we change P_{Namax} at high frequency, making P_{Namax} 1.3-fold at 500 Hz. As we expected, the EOD amplitude increases (Fig. 2.2.4 B). The posterior action potential peak gets more depolarized (Fig. 2.2.4 A). However, its trough has undergone insignificant changes (Fig. 2.2.4 A) because the Nav is closed at this phase. V_a becomes more depolarized (Fig. 2.2.4 A), resulting in a larger EOD amplitude.

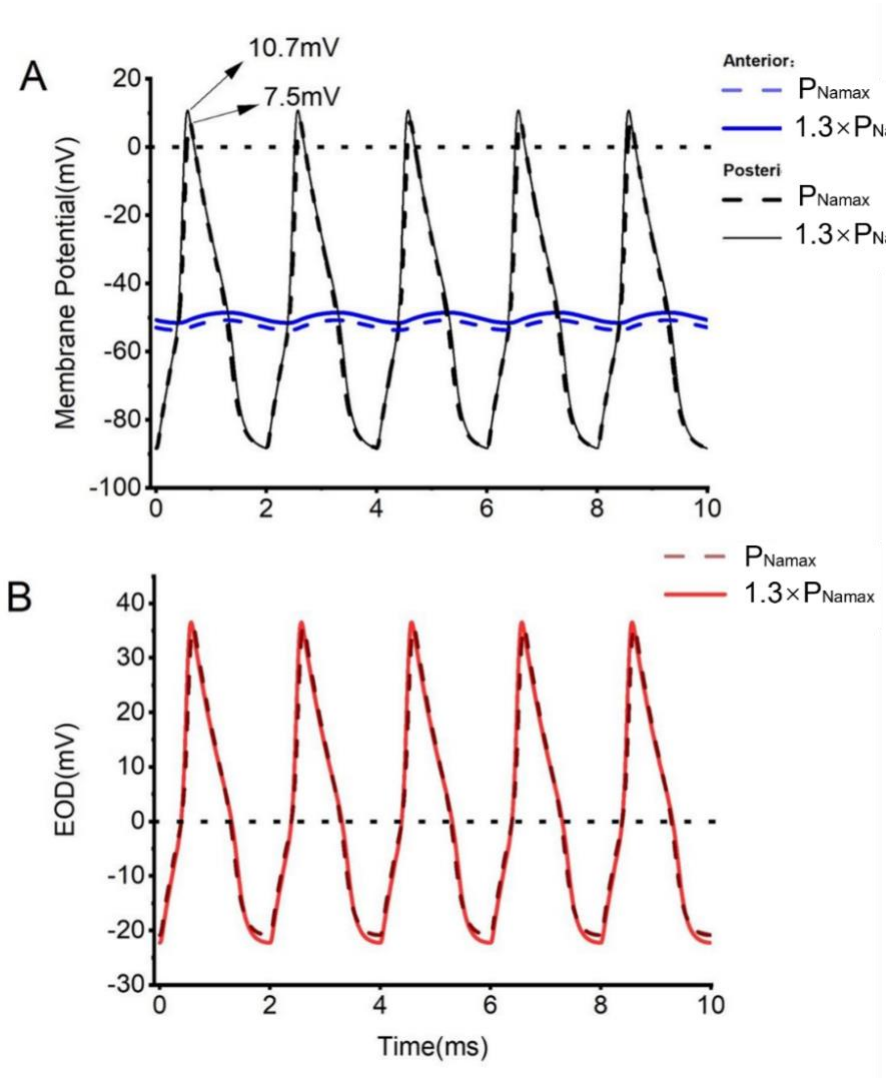

Figure 2.2.4 **Boost the P_{Namax} of *Eigenmannia* at 500 Hz. A**: The anterior and posterior membrane potentials with different P_{Namax} values. As V_a became polarized, the peak of V_p became depolarized. **B**: *Eigenmannia*-type EOD with varying P_{Namax} values. The peak of EOD is more depolarized, whereas the through is more polarized, resulting in a larger amplitude.

2.2.3. Determinants of *Eigenmannia*-type EOD magnitude.

The preceding section demonstrated a decrease in EOD amplitude as the frequency increased with constant PNamax. In this section, we will explore various parameters of the system to identify the determinants of *Eigenmannia*-type EOD magnitude. The cytoplasmic resistance (R_{cyt}) links the anterior and posterior compartments. Changes in R_{cyt} from 0.2-fold to 10-fold have negligible effects on the V_a and V_p (Fig. 2.2.5 A). The resultant EODs almost overlap (Fig. 2.2.5 B). The cytoplasmic resistance (R_{cyt}=0.004255 MΩ) is considerably smaller than the gap resistance (R_{gap}=0.5 MΩ). However, when an extreme change in R_{cyt} is made by making it 100-fold larger, the EOD amplitude decreases significantly. In this case, R_{cyt} is on the same order of magnitude as R_{gap} , resulting in a smaller cytoplasmic current. Therefore, EOD amplitude decreases.

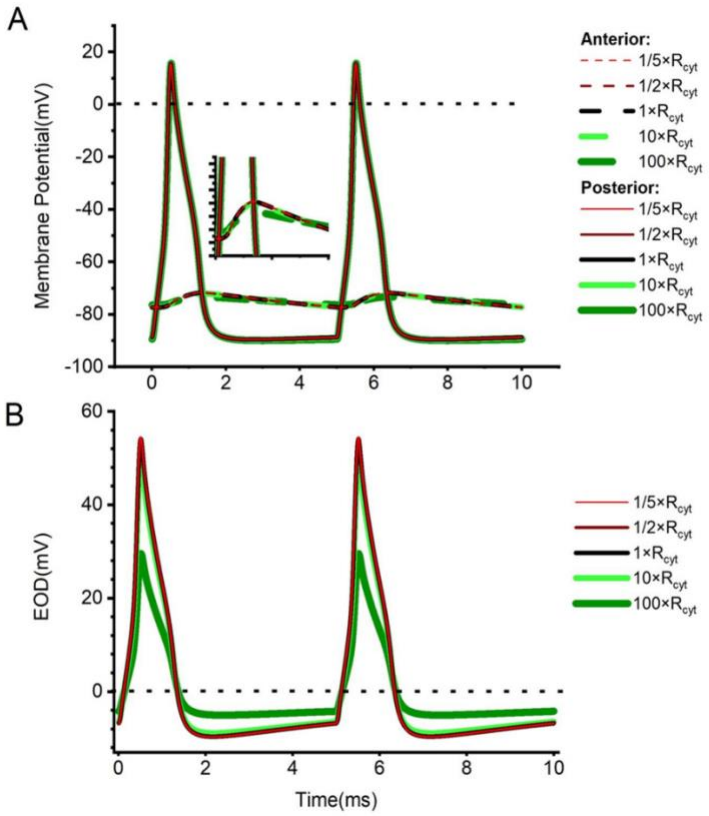

Figure 2.2.5 **Variation of cytoplasmic resistance (R_{cyt}) of *Eigenmannia* at 200 hertz. A**: The membrane potential of the anterior and posterior ends with distinct R_{cyt} values. The impact of modifying R_{cyt} is negligible; the lines overlap. **B**: Eigenmannia-type EOD with different R_{cyt}. Given that changes in membrane potentials are negligible, the EODs under varied R_{cyt} are consistent.

However, the gap between *Eigenmannia*'s electrolytes has unknown properties. According to a prior study (Joos et al., 2018a), when the R_{gap} dominant effective resistance is equivalent to 0.5 MΩ, the triggered *Eigenmannia*-type EOD matches experimental observation. In this similar circuit, R_{gap} is assumed to be 0.5 MΩ, and several R_{gap} values are investigated. As R_{gap} increases, the peaks of V_p become slightly depolarized, whereas the trough and resting state becomes marginally polarized (Fig. 2.2.6 A). R_{gap} regulates the magnitude of the cytoplasmic current, which is essential to the EOD shape (Fig. 2.2.6 B). When R_{gap} gets larger, cytoplasmic current will be smaller. Thus, the amplitude of the resultant EOD decreases. In addition, since the anterior end is a pure capacitor, a larger R_{gap} will decrease the cytoplasmic current, resulting in more polarized V_a peaks and more depolarized V_a troughs (Fig. 2.2.6 A).

The EOD peak becomes more depolarized with increasing R_{gap} due to the polarized V_a peak and the depolarized V_p peak. Furthermore, the EOD trough becomes more depolarized according to the depolarized V_a trough and the polarized V_p trough. However, when R_{gap} is too small, one fifth of its standard value, the head-negative phase of the EOD loses its shape with an unrealistic curvature. In conclusion, these findings indicate that the R_{gap} determines the shape of EOD.

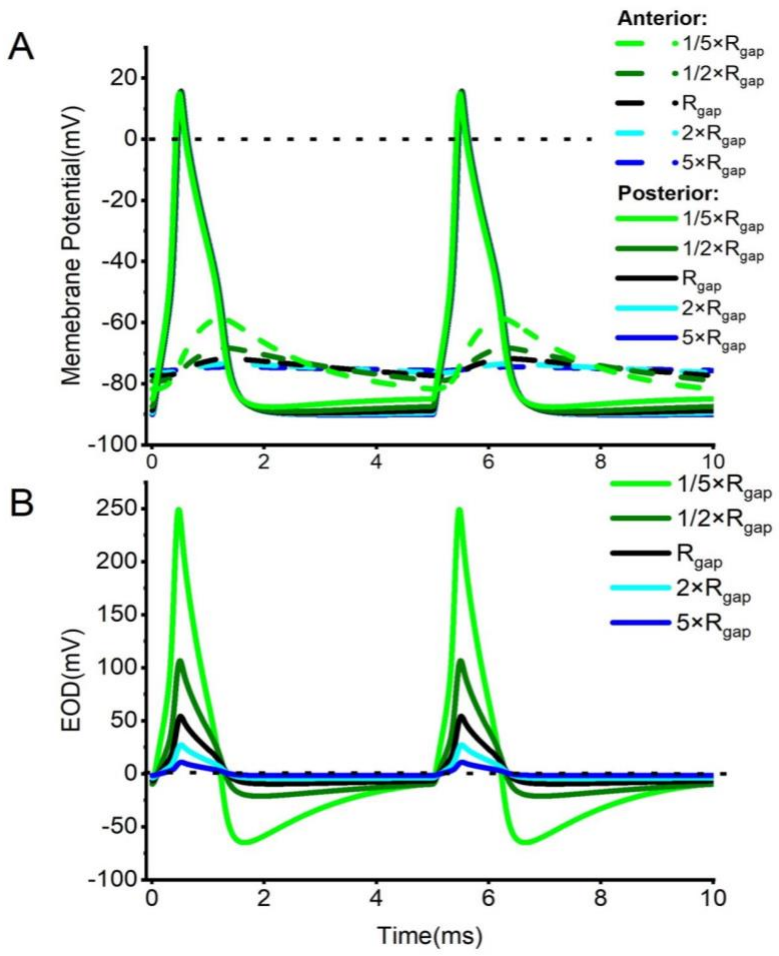

Figure 2.2.6 **Changing gap resistance (R_{gap}) of *Eigenmannia* at a frequency of 200 Hz. A**: The membrane potentials of the anterior and posterior membrane end with distinct R_{gap} values. As R_{gap} increases, the peaks of V_p become slightly depolarized, but the trough and resting states become polarized. Since the anterior end is a pure capacitor, increasing R_{gap} reduces V_a's responsiveness to the V_P. **B**: *Eigenmannia*-type EOD with various R_{gap}s. As the R_{gap} rises, the EOD peak becomes polarized, but the trough becomes more depolarized.

Furthermore, there are narrow, blind-ended tubular invaginations at the anterior end of *Eigenmannia*. These tubulars can be thought of as high-resistance capacitors in series. As shown in Eq. (10), a substantial change in R_t would have a negligible influence on V_a. The system is evaluated with a R_t that is ten times bigger. As a result, the V_p remain constant, the change in V_a is unsignificant (Fig. 2.2.7 A), and the resultant EODs are unchanged (Fig. 2.2.7 B).

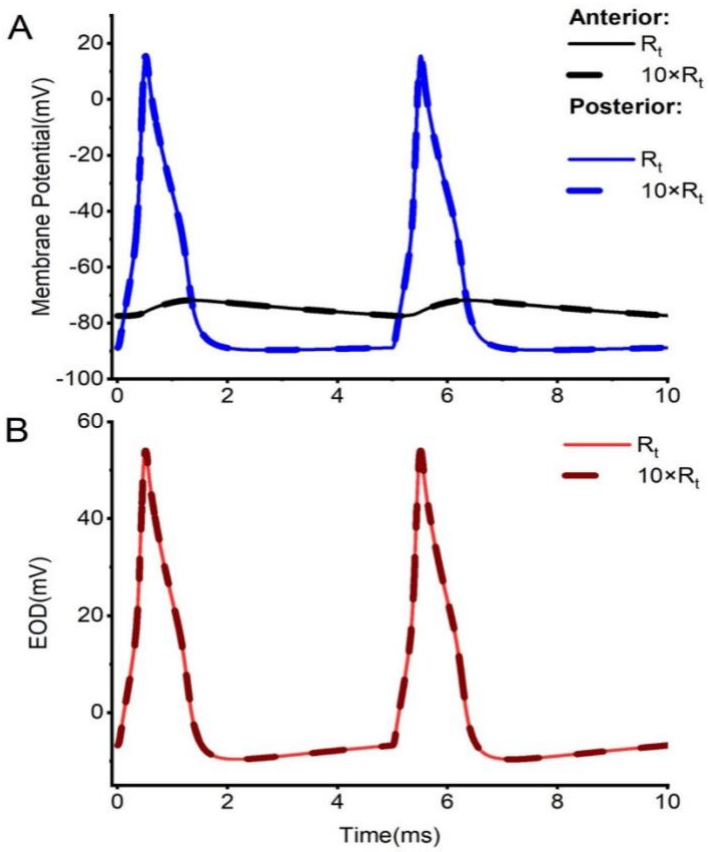

Figure 2.2.7 **Modifying the tubular resistance (R_t) of *Eigenmannia* at 200 Hz. A**: The membrane potentials of the anterior and posterior membrane end with different R_t values. When R_t is ten times larger, V_p and V_a remain constant. **B**: *Eigenmannia*-type EOD with various R_t. As R_t rises, the EODs tend to be constant.

We also evaluate if a change in anterior membrane capacitance influences the magnitude of EOD. A variation in capacitance at the anterior end has no effect on the posterior action potential V_p. The reason is that the total transmembrane current is much larger than I_{cyt}. However, when the anterior membrane capacitance gets smaller, we obtain a considerably depolarized V_a peak, a more polarized V_a trough, and a larger V_a amplitude. The reason is that V_a is inversely proportional to the anterior end capacitance (Eq. (7)). In addition, the EOD is defined by the difference between the posterior V_p and anterior V_a, as discussed above. During the head-negative phase, a depolarized peak, and a polarized trough of V_a with a smaller C_a result in a more polarized trough and a more depolarized resting state for EODs. (Fig. 2.2.8 A). Notably, EODs show an obvious curvature at the trough, which means that C_a changes the EOD amplitude (Fig. 2.2.8 B).

In summary, the amplitude of *Eigenmannia*-type electric organ discharges (EOD) is primarily influenced by gap resistance (R_{gap}) and anterior membrane capacitance (C_a). R_{cyt} has a negligible impact on the amplitude unless it approaches the same order of magnitude as R_{gap}. R_t has minimal effect on the amplitude of *Eigenmannia*-type EOD.

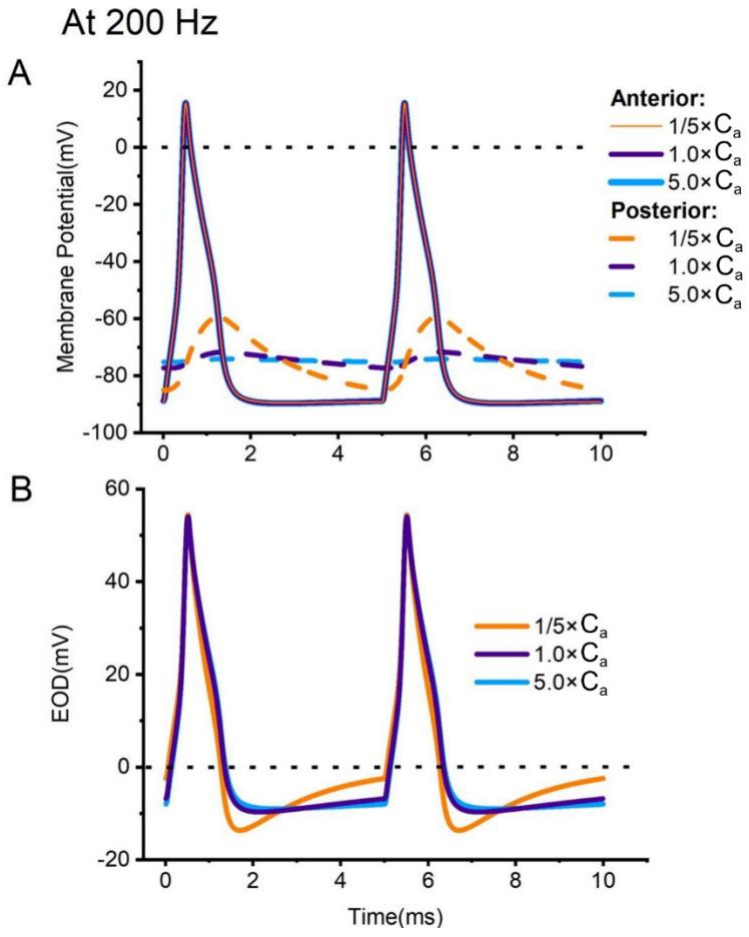

Figure 2.2.8 **Membrane potentials and EODs for *Eigenmannia* with a variety of anterior membrane capacitances at 200 Hz. A**: The anterior and posterior membrane potentials with different anterior capacitance values. As C_a increases, V_p remains intact. Because the anterior end is a pure capacitor, increasing C_a reduces V_a's variation to the V_p. **B**: *Eigenmannia*-type EOD with different C_a. As C_a increases, the EOD peak and resting state polarize while the trough depolarizes.

2.2.4. Insights into Tubular Invaginations

Most of the anterior membrane consists of tubular invaginations. A significant resistance (R_t), which symbolizes tubular lumens occupied by charge-dense proteins, is connected in series with the capacitance of the tubules (Schwartz et al., 1975). Thus, the tubular voltage depends on

V_a, R_t and C_t. Even though R_t is ten times larger than the reference value, changes in R_t have a negligible influence on V_t (Fig. 2.2.9 D). The reason is that R_t is a significant resistance. When the resistance gets larger, the current through the tubule is even more modest. When R_t and C_t are fixed, modification in R_{cyt} generates inconsequential alterations in V_a. Hence, the difference between V_t is negligible (Fig. 2.2.9 B). Nevertheless, V_a shows an enhanced response to changes in R_{gap}. Therefore, V_t varies more with changing R_{gap} (Fig. 2.2.9 C). Furthermore, as the frequency increases, V_a becomes more polarized, causing V_t to also become more polarized (Fig. 2.2.9 A).

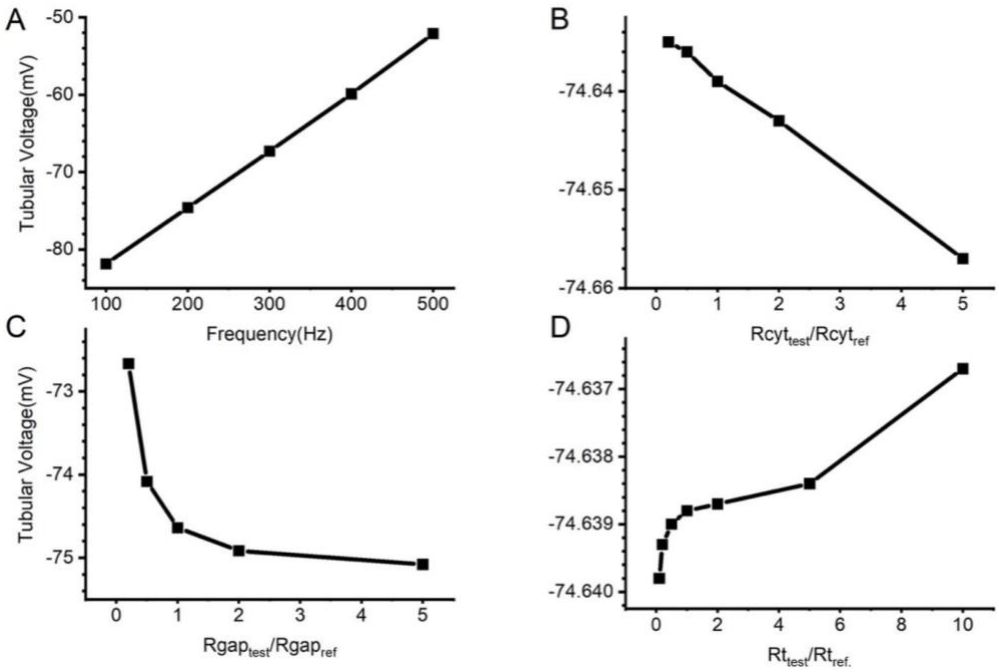

Figure 2.2.9 **Tubular voltage of *Eigenmannia* under different variations. A**: Variation in tubular voltage with various frequencies. **B**: Small variation in tubular voltage with changing R_{cyt}. **C**: Variation in tubular voltage with changing R_{gap}. **D**: Negligible alteration in tubular voltage with different R_t values.

2.2.5. Observed *Eigenmannia*-type EOD suggests the imperfect synchronicity in the activation of electrocytes.

Experimental analysis reveals that *Eigenmannia*-EOD has a sinusoidal form. However, the EOD anticipated by the equivalent circuit model does not accurately fit this characteristic. For *Eigenmannia*, there are two types of neurons in the medullary pacemaker nucleus:

pacemaker cells and relay cells. Each pulse from the pacemaker cells is transmitted to the spinal motor neurons of the electric organ via the relay cells. Previous research on *Eigenmannia* has assumed that the activation of the EO's electrocytes is effectively synchronized. However, research on skeletal muscle demonstrated that a significant fraction of sympathetic AP discharge fires asynchronously between human muscle sympathetic nerve activity bursts (Klassen and Shoemaker, 2021). Since *Eigenmannia* electrocytes are derived from skeletal muscle, we hypothesize that the imperfect synchronicity in the activation of electrocytes.

To demonstrate how imperfect synchronicity would affect EODs, we let the 1000-electrocyte EO have five different AP arrive time and calculated the EOD with 0.1 ms time intervals at different frequencies (Fig. 2.2.10). The only variable is the rate of pulsatile activation of the posterior AChR. In the region of *Eigenmannia*'s firing frequency, the EODs have a more sinusoidal shape and lose amplitude with a 0.1 ms temporal interval, which corresponds to the experimental findings (Assad et al., 1998). To better explore the impact of imperfect synchronicity on EODs, the time interval is increased to 0.2 ms at 200 Hz and the population size is also increased to 15 (Fig. 2.2.11). We find that both increasing the time interval and rising populations of difference arrive time result in a decrease in the amplitude of EOD. With an interval of 0.1 ms, the EODs have a more sinusoidal shape compared to the reference EODs. The sinusoidal shape of EOD improves as the population size increases from 5 to 15. When the time interval is raised to 0.2 ms, the effects of imperfect synchronicity become more significant. The *Eigenmannia*-type EOD starts to lose its shape and become less homogenous. Moreover, the EODs of fifteen populations with a 0.2-ms spacing cannot maintain *Eigenmannia*-style EODs. Thus, there is an imperfect synchronicity in the activation of electrocytes.

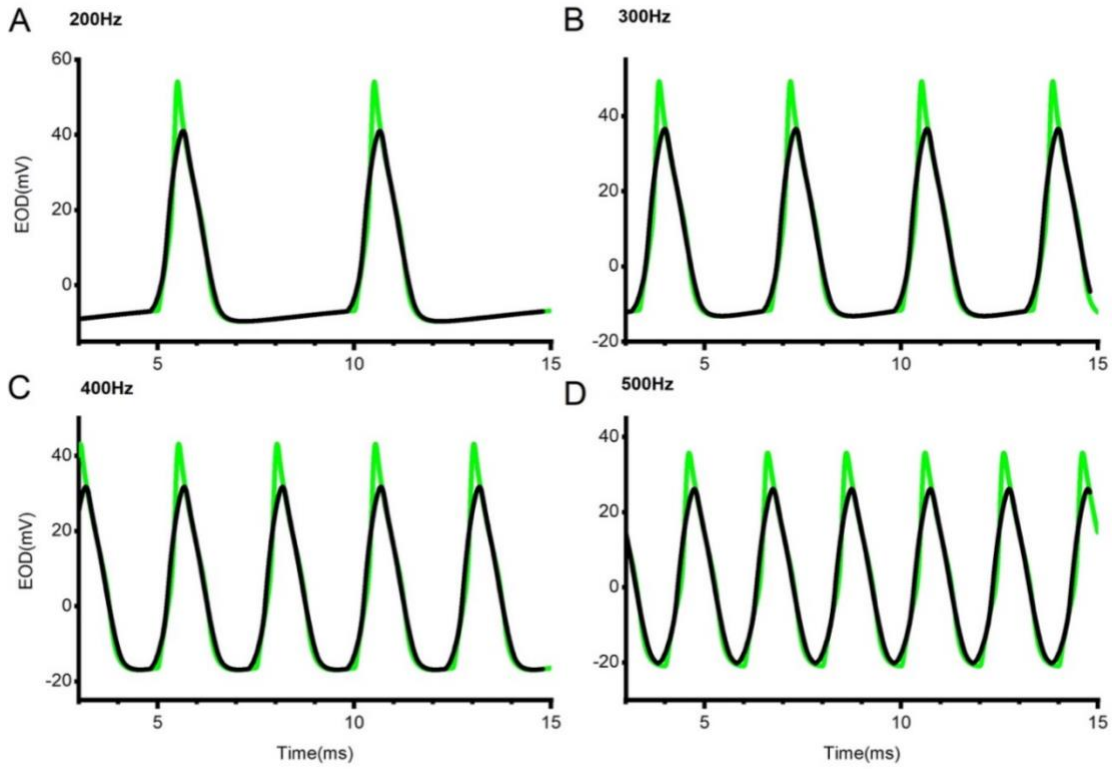

Figure 2.2.10 ***Eigenmannia*-type EODs with imperfect synchronicity between 200Hz and 500Hz, with five different arrival time (-0.2, -0.1, 0, 0.1, 0.2 ms). A**:200Hz **B**:300Hz **C**:400Hz **D**:500Hz

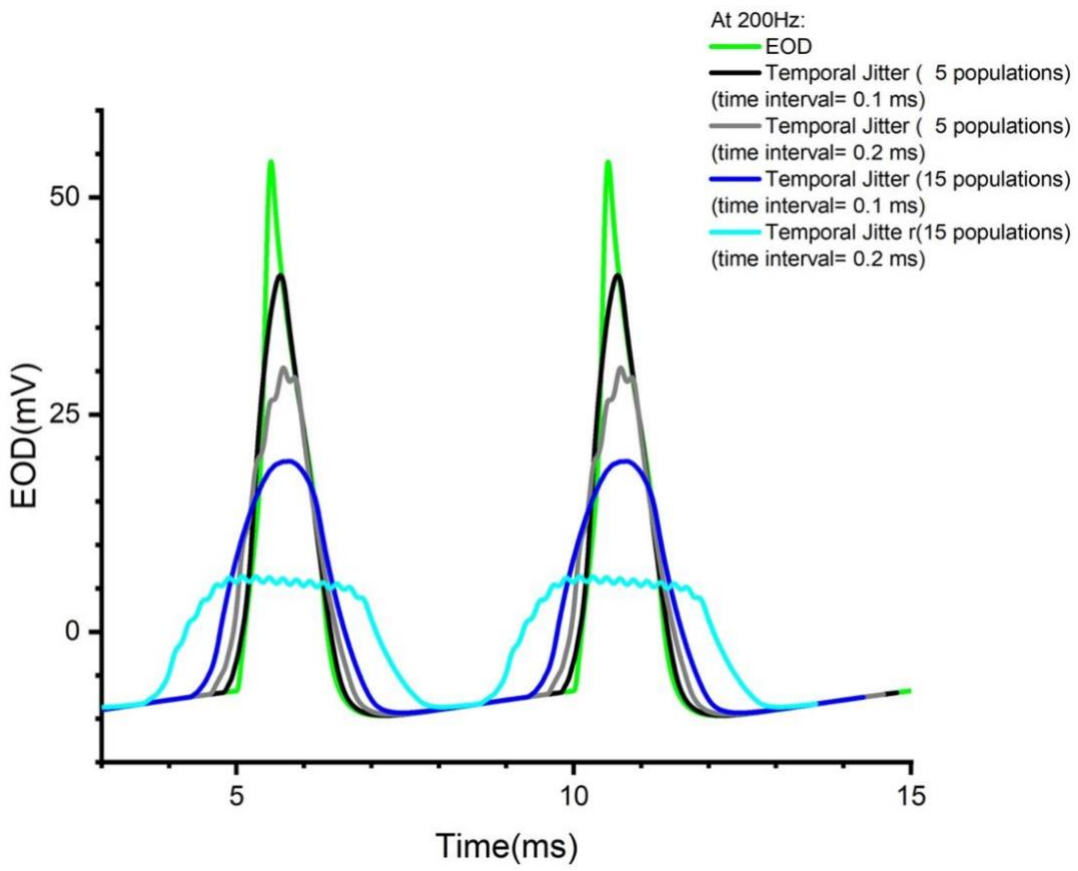

Figure 2.2.11 ***Eigenmannia*-type EODs with different temporal differences and population at 200 Hz.** The activation of 1,000 electrocytes in perfect synchrony is improbable. To demonstrate how imperfect synchronicity affects EODs, we let 1000-electrocyte EO have 5 and 10 different arrival time (populations) and calculate the EOD for two diverse levels of asynchrony.

2.3. *Electrophorus*

2.3.1. Conversion of *Eigenmannia*-type EOD to *Electrophorus*-type EOD

Evolutionarily, *Eigenmannia* and *Electrophorus* are closely related genera. To provide a substantive extra dimension for reality checks, we transform an *Eigenmannia*-type EOD into an *Electrophorus*-type. In the initial step, we introduce an anterior potassium leak with the same channel density as the posterior potassium leak, denoted as $P_{La}=(C_a/C_p)P_L$. This addition induces a substantial potassium leak current through the anterior membrane, leading to a polarization of V_a (Fig. 2.3.1 A1). Consequently, the head-negative phase or the baseline of the EODs becomes more depolarized (Fig. 2.3.1 B1). The addition of this leak at the anterior end can be considered a transitional stage between *Eigenmannia*-type and *Electrophorus*-type EODs.
Morphological observations highlight distinct features in *Electrophorus*, including a significantly larger anterior leak permeability, lower cytoplasmic resistance, and lower gap resistance (Details are available in the introduction Section 1.4.2). To simulate *Electrophorus*-type characteristics, we first increase the P_{La} 1,000-fold higher than the one of the posterior one and increase C_a 10-fold. This abundance of leak channels drives the anterior end to become highly polarized, reaching approximately -92.5 mV, exhibiting a direct current-like feature (Fig. 2.3.1 A2). Considering the leak channel density at the anterior, we proportionally increase the anterior capacitance by a factor of ten, corresponding to the membrane area. Consequently, EODs demonstrate an almost neutral baseline rather than a head-negative one (Fig. 2.3.1 B2), aligning with expectations for *Electrophorus*-type EODs. However, the magnitude of the EOD remains comparable to *Eigenmannia*-type EODs.

Subsequently, we make R_{cyt} 5 times smaller, with minor contribution to the R_{eff}. The resulting drop in R_{cyt} has an insignificant impact on V_a, V_p, and EOD (Figs. 2.3.1 A3 and B3). Furthermore, we make R_{gap} 10 times smaller, where R_{gap} dominates R_{eff}. As the R_{gap} decreases, the posterior current depolarizes the V_p (Fig. 2.3.1 A4). This leads to a rise in I_{cyt}, causing a slightly more depolarized V_a (Fig. 2.3.1 A4). The EOD is equal to the product of the number of columns (M), the cytoplasmic current (I_{cyt}), and R_{ext}. A drop in R_{gap} may substantially increase I_{cyt} and make significantly larger EODs, about 586 mV (Fig. 2.3.1 B4).

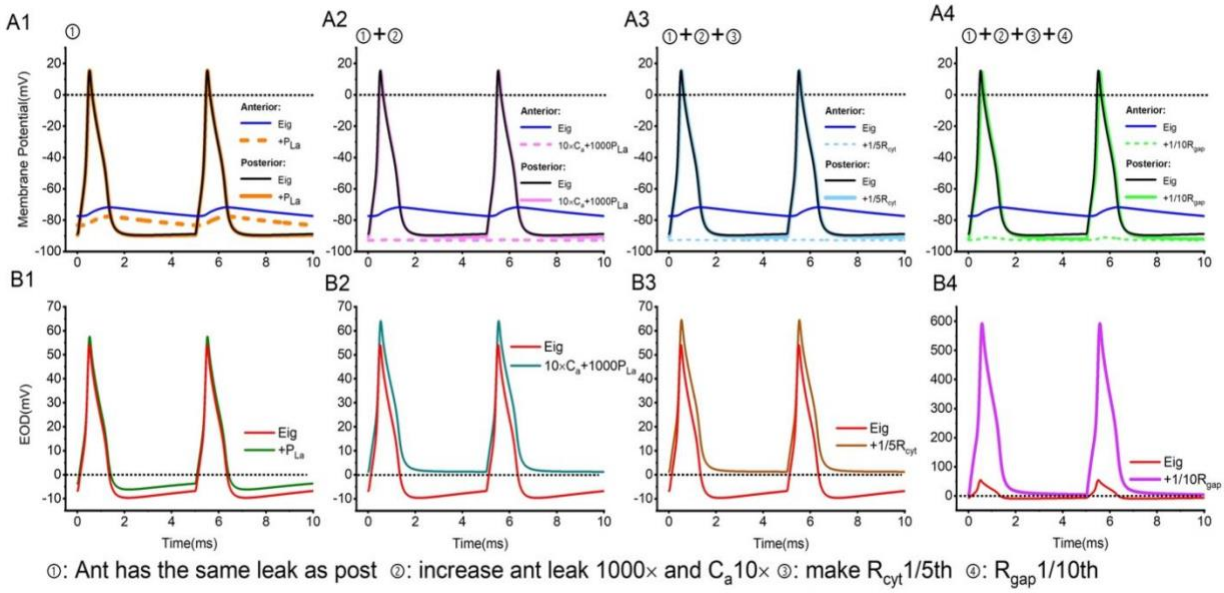

Figure 2.3.1 **Conversion of an *Eigenmannia*-type EOD to an *Electrophorus*-type EOD.** To convert an *Eigenmannia*-type EOD to an *Electrophorus*-type, we first add a leak with the same density as the posterior. Then, we make the anterior leak 1,000 times larger and increase C_a 10-fold. Next, we make R_{cyt} are five times smaller. Finally, we make R_{gap} 10 times smaller.**A1-A4**: Membrane potentials under different situations **B1-B4**: EODs under different conditions. After the following change, we get *Electrophorus*-type EODs with head-positive peak and natural baseline.

Notably, even with a doubled and a fivefold area of posterior end, the anterior end can retain the DC property of V_a (Fig. 2.3.2 A) as well as *Electrophorus*-type EODs with a positive and almost neutral baseline (Fig. 2.3.2 B). In the scenario of a larger posterior end, the number of channels and membrane capacitance must increase to maintain the same channel density. Therefore, the currents on posterior end i.e., I_{leak}, I_{stim}, I_K, I_{Na} become stronger to depolarize the V_p (Fig. 2.3.3 A). However, the resulting V_p is insignificantly depolarised (Fig. 2.3.2 A) because of increasing C_p. Further, V_a depolarization is negligible, about 0.05 mV (Fig. 2.3.2 A). Due to insignificantly depolarized V_p, negligible depolarization of V_a, and unchanged effective resistance, the current of an electrocyte is barely changed (Fig. 2.3.3 B). Consequently, the EOD demonstrates insignificant depolarization despite the enlarged membrane area.

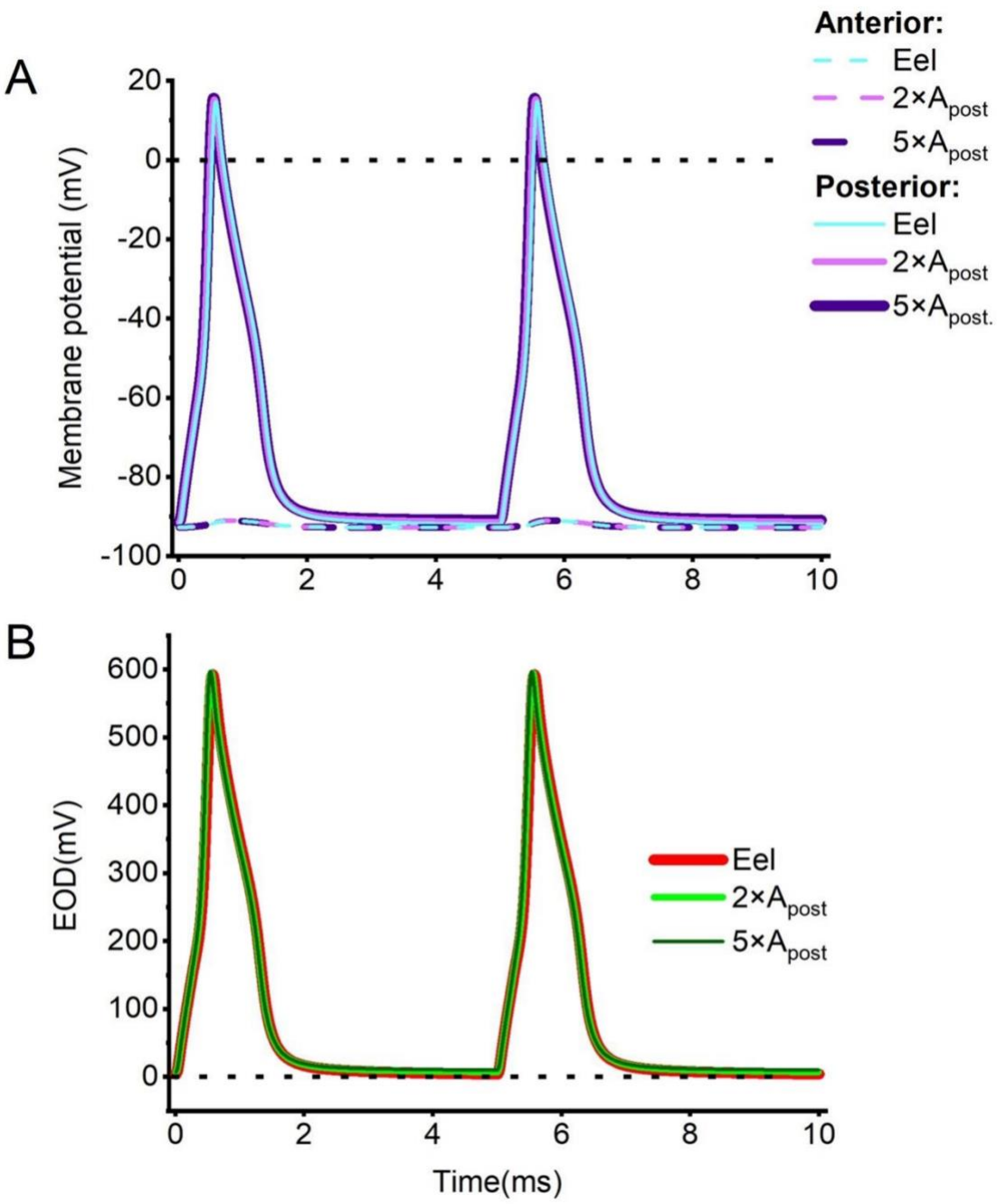

Figure 2.3.2 **Increasing the *Electrophorus* posterior membrane area twofold and fivefold. A**: The *Electrophorus* anterior and posterior membrane potentials with a double and fivefold posterior area. **B**: EODs of *Electrophorus* with a posterior area twice and five times larger. A larger posterior end results in a modest alteration in membrane potentials and EODs.

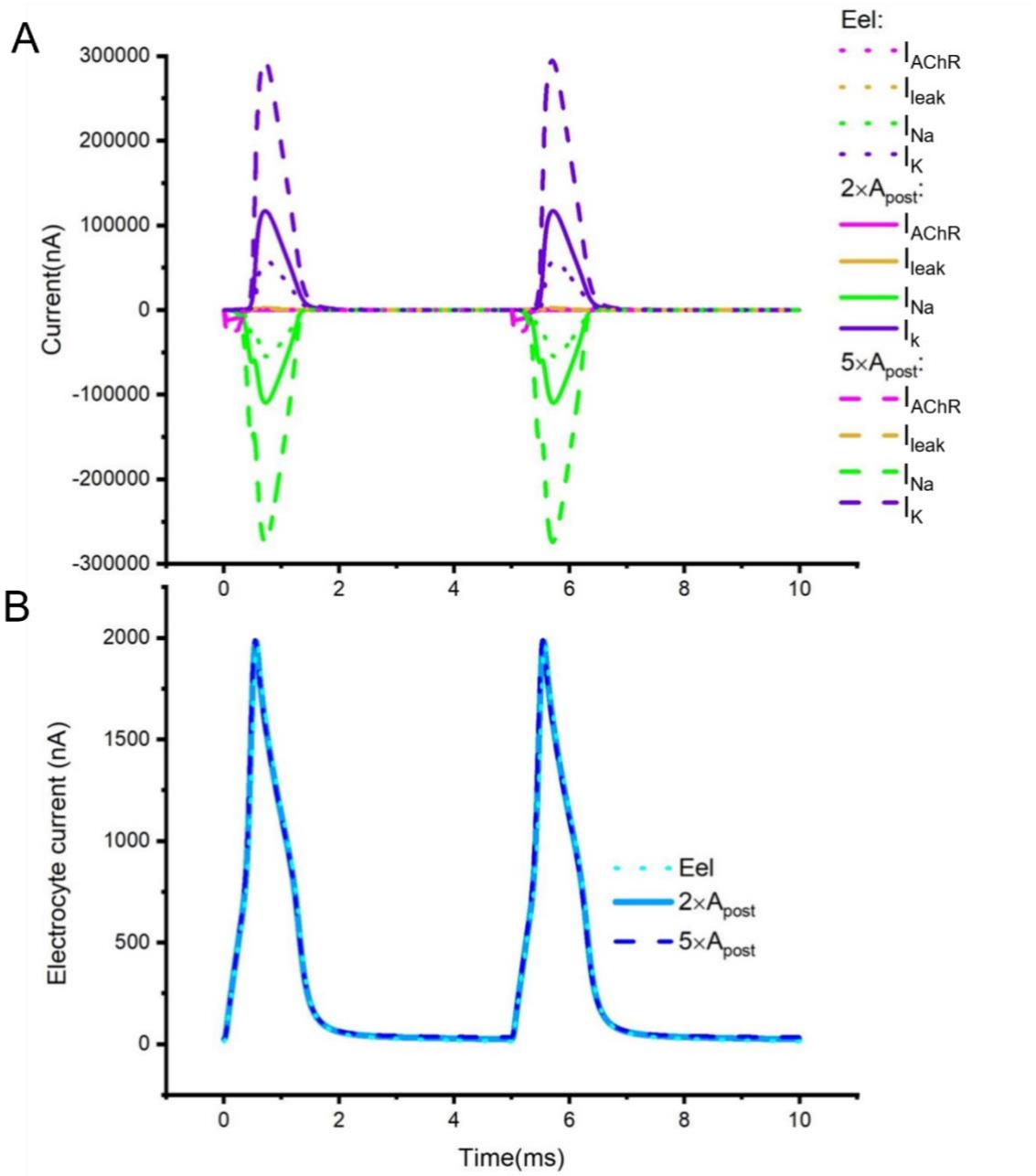

Figure 2.3.3 **Current with a two- to fivefold increase in the posterior membrane area of the *Electrophorus.* A**: The current components of the *Electrophorus* anterior and posterior ends, with double and fivefold posterior areas. **B**: Current through an *Electrophorus* with a posterior area that is twice as large and five times as large as its anterior. I_{cyt} remains constant when the posterior area gets larger.

However, when the area of the posterior end shrinks by a factor of 0.2, the posterior current is insufficient to depolarize the posterior membrane and trigger enough opening of Nav channels and Kv channels. Thus, the posterior AP lacks the overshoot characteristic (Fig. 2.3.4 A). While the posterior end of the channel is not depolarized enough to trigger the firing of an action potential, a small fraction of the voltage-gated channels remains open, leading to a minor current flow through Nav and Kv (Fig. 2.3.5 A). Voltage influences the dynamic properties, including Nav activation (m), Nav deactivation (h), and Kv activation (n). The depolarization of the posterior end leads to a small proportion of Nav (m^3h) and Kv (n^2) channels opening, with respective fractions of 0.003 and 0.0075 (Fig. 2.3.6). In addition, the I_{La} is too leaky compared to a significantly decreased posterior current. In this case, although the EODs' shape is *Electrophoru*s-type, they are unhealthy (Fig. 2.3.4 B) because of the failure of the firing AP.

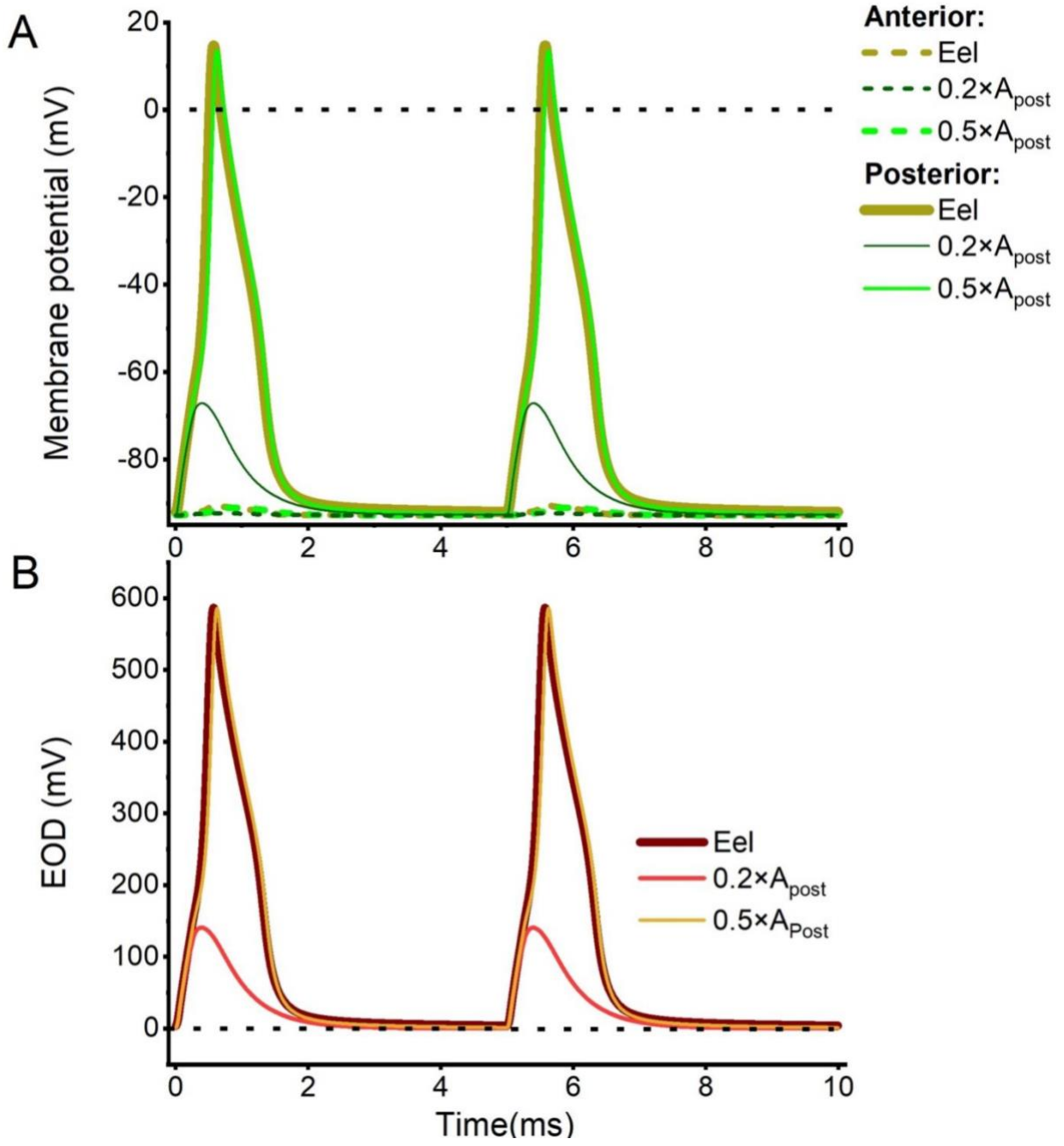

Figure 2.3.4 **Reducing the *Electrophorus* posterior membrane's area (A_{post}) by a half and a fifth. A**: The membrane potentials of the *Electrophorus* anterior and posterior ends with one-half and one-fifth smaller posterior area. **B**: *Electrophorus* EODs with one-half and one-fifth posterior. When the area of the posterior end shrinks by a factor of 0.2, the posterior current is insufficient to depolarize the posterior membrane.

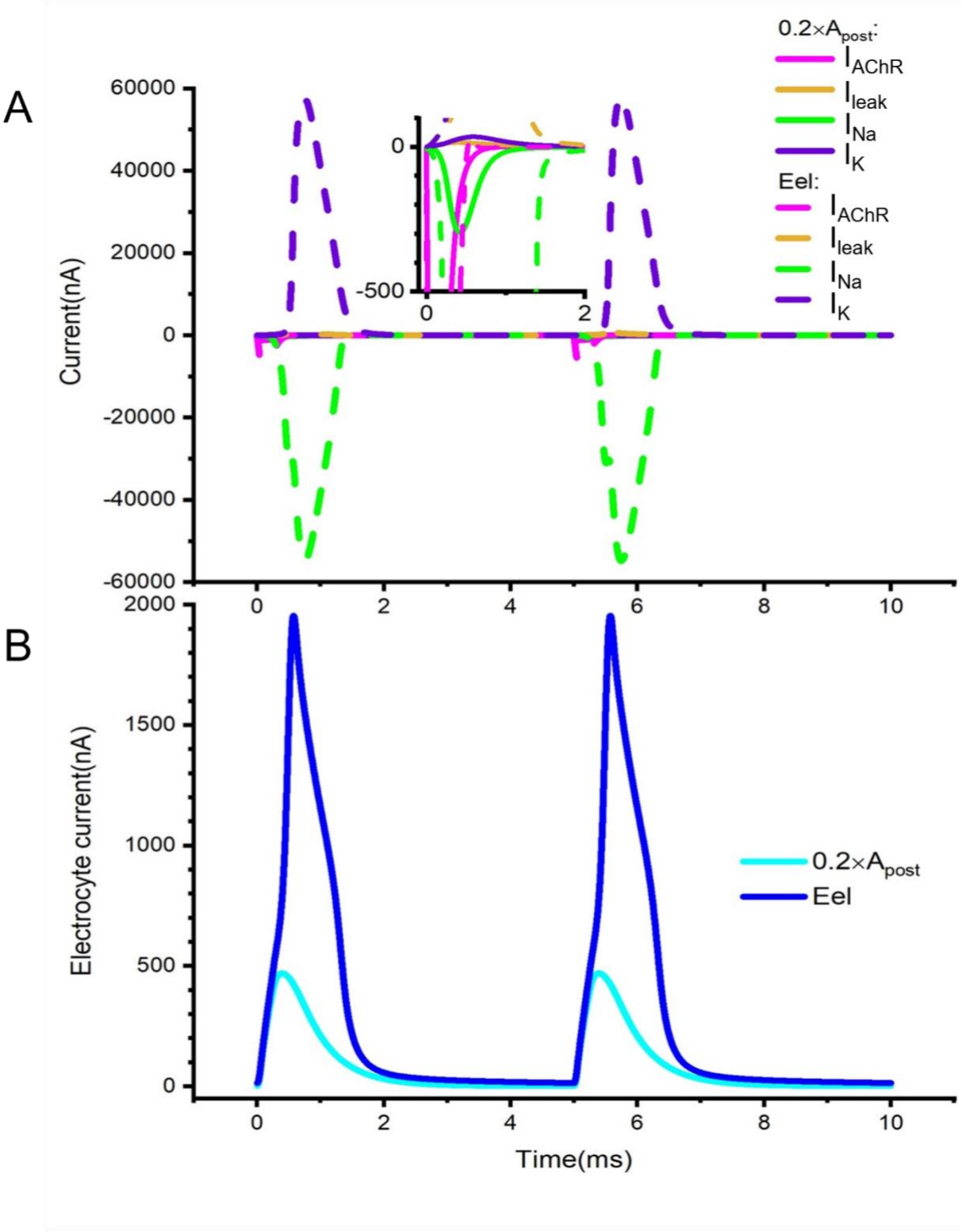

Figure 2.3.5 **Current with a 0.2-fold reduction in *Electrophorus* posterior membrane area (A_{post}). A**: Current components at the *Electrophorus* anterior and posterior ends indicate a 0.2-fold reduction in membrane area at the posterior end. **B**: A current flows through an *Electrophorus* whose posterior region is 0.2 times larger than its anterior region.

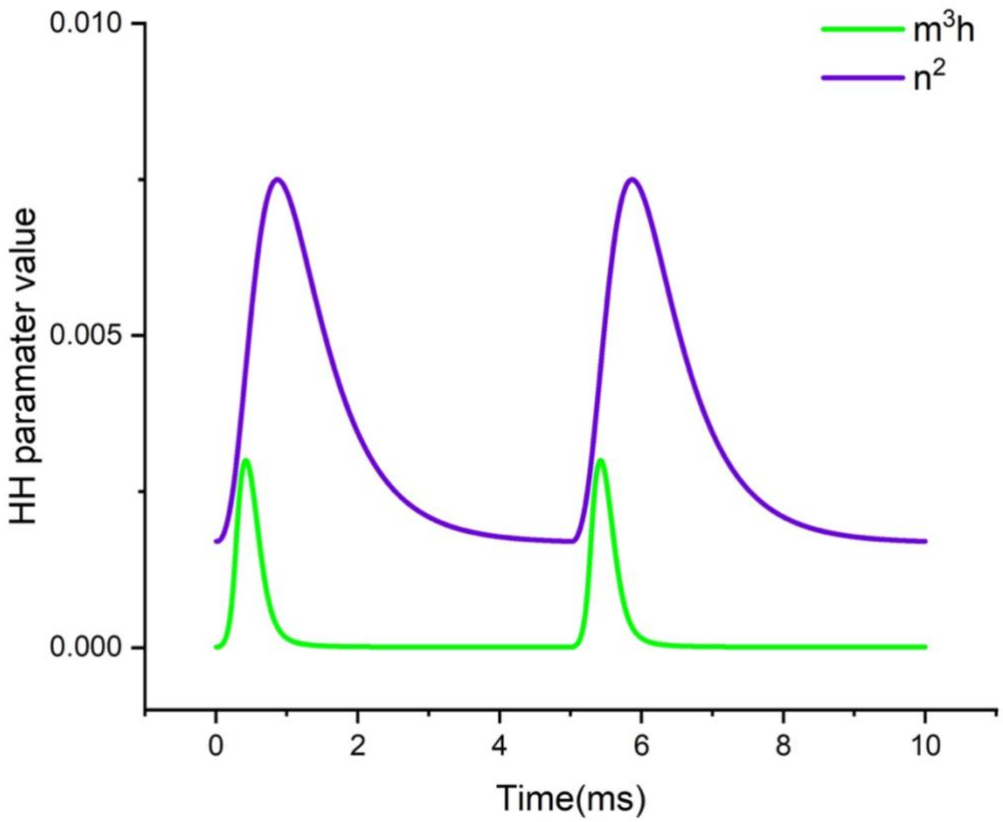

Figure 2.3.6 **H-H parameter value for the opening of Nav (m^3h) and Kv (n^2) channels with a 0.2-fold reduction in *Electrophorus* posterior membrane area.**

2.3.2. A burst of *Electrophorus*-type EODs

Studies have shown that *Electrophorus* uses its taser-like EOD to prey. To simulate this feature, we evaluate the membranes potentials and the EODs with a longer duration (100 ms). The results show that the EOD's amplitude remains steady (Fig. 2.3.7 B). The *Electrophorus*-type EODs produced by 1000 electrocytes are approximately 592 mV. It is comparable to the experimental recording with larvae of *Electrophorus* (Schwassmann et al., 2014).

As the *Electrophorus* grows, the size and volume of the electrocytes increase, causing a higher EOD amplitude. In addition, *Electrophorus* produces predation-related bursts at roughly 100 Hz; therefore, we also evaluate the EOD at this frequency. At 100Hz, the membrane has more time to return to its resting state. Therefore, V_p has more time to polarize, and V_a is slightly more depolarized than the results at 200Hz (Fig. 2.3.8 A), whereas the baseline of EOD approaches closer to zero. However, the amplitude of EODs is insignificantly more depolarized, approximately 593 mV (Fig. 2.3.8 B). Remarkably, the maximum reported current in *Electrophorus* is approximately 1 A (Cox et al., 1945), a value significantly higher than the results we obtained through stimulation. This disparity may be attributable to our parameters, including effective resistance, capacitance, and channel permeability, which are not perfectly proportional. Nevertheless, reproducing the powerful EOD is not the purpose of our project.

Through modifications in cellular properties, our spatially defined equivalent circuit model successfully transforms *Eigenmannia'*s dipolar oscillator-like electric organ discharge (EOD) into a biotaser-like EOD. This feature indicates that our circuit model can generate the appropriate EOD type for each genus.

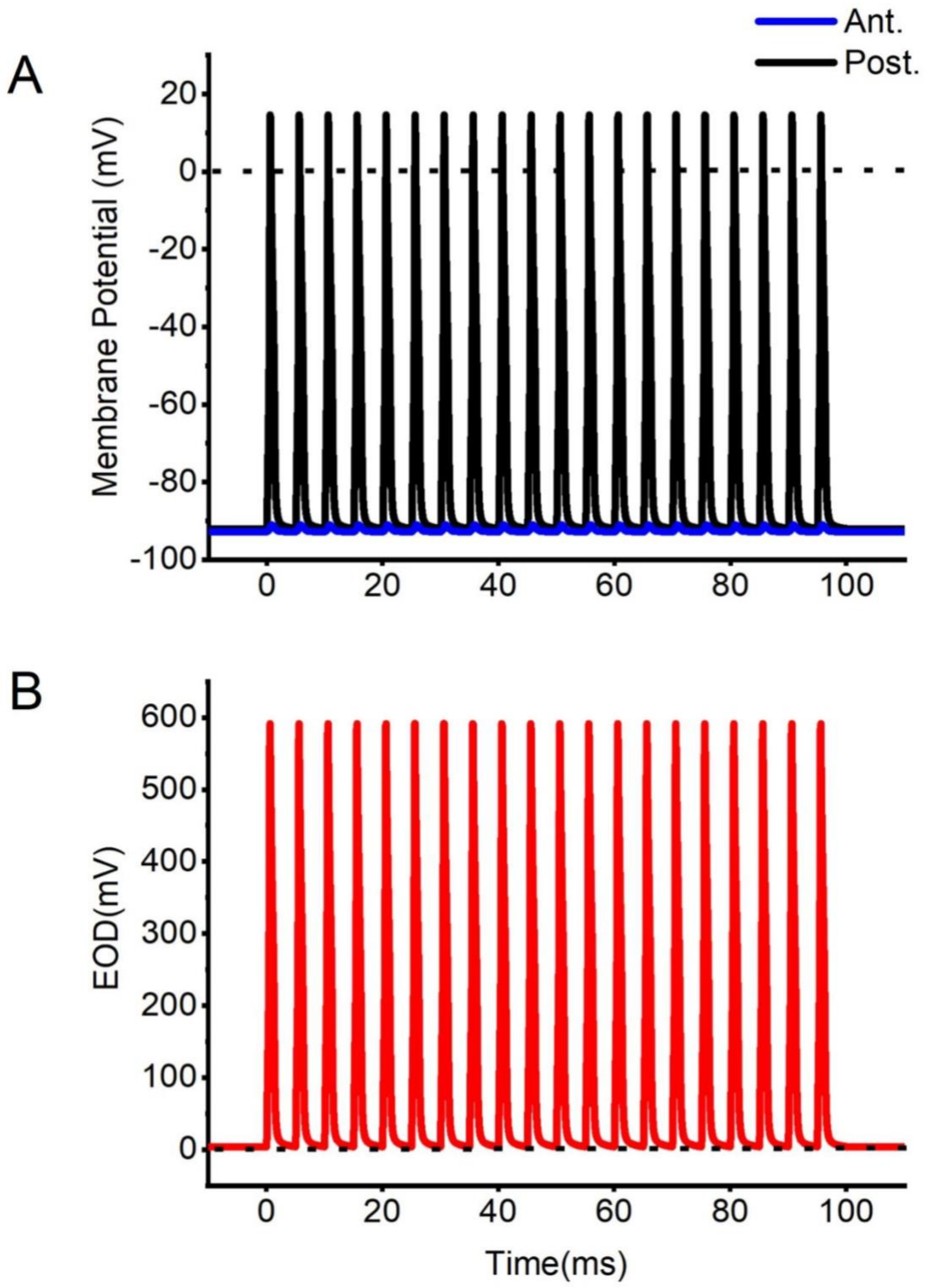

Figure 2.3.7 ***Electrophorus*** **taser-like EODs with detailed membrane potentials at 200 Hz (100 ms). A**: The membrane potentials of the anterior and posterior membrane end for *Electrophorus*. The action potential is triggered at the posterior end, and the anterior end shows a DC feature. **B**: *Electrophorus*-type EOD with almost neutral baseline.

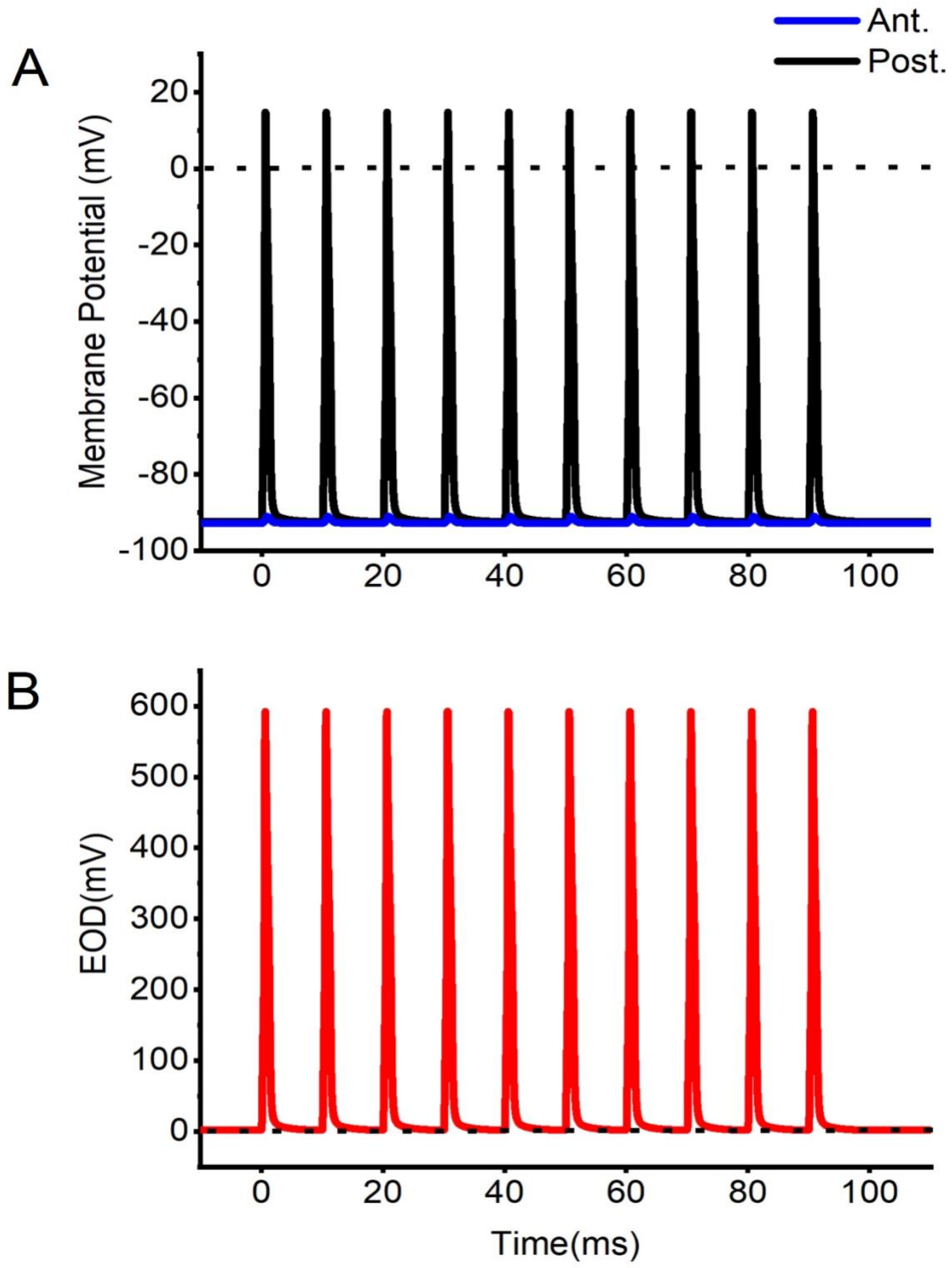

Figure 2.3.8 **Membrane potentials and EODs of *Electrophorus* at 100Hz (100 ms). A**: The membrane potentials of *Electrophorus*' anterior and posterior membrane end. The posterior end initiates the action potential, while the anterior end displays a DC characteristic. **B**: EOD of the *Electrophorus* variety with a nearly neutral baseline.

3. Posterior/Anterior Charge Difference Model (PA-CD) for Endogenous Electric Field (EEF)

3.1. PA-CD: One dimensional ion homeostasis model.

Under the assumption of ion homeostasis, we use axial resistance to connect the anterior and posterior compartments in chapter 2 to develop an equivalent circuit model.
In this chapter, we develop a one-dimensional ion homeostasis model PA-CD (Posterior/anterior charge difference) in which diffusion and electric-field terms replace resistance. There is a closed circuit between the cell or cell pair and its surroundings. The model resembles a two-compartment cell or a pair of cap junction cells. In steady state, the external current (I_{ext}), axial current (I_{axial}), and transmembrane currents ($I_{tran,a}$ and $I_{tran,p}$) in two compartments are equal (Fig. 3.1.1). The PA-CD is based on the Morris et al. (2022) and Dijkstra et al. (2016). The physical attributes are identical to their models. The models are zero-dimensional in earlier studies. In this thesis, this general polarized cell, PA-CD, is created by connecting two zero-dimensional units and we focus on the minimal P-L/D system. Even though this P-L/D ion homeostasis model is one-dimensional, its one-dimensionality is not functionally significant until posterior and anterior membrane permeabilities become asymmetric. Furthermore, to evaluate our new one-dimensional model, we begin with a model that excludes voltage-gated channels, meaning that the cell is non-excitable.

3.1.1. Intercompartmental currents:

Utilizing the Nernst-Planck equation, our model incorporates diffusion and drift currents to simulate intercompartmental currents. The diffusion current responds to the concentration gradient of ion species within each compartment, while the voltage differential between compartments drives the drift current. Given the intercompartmental nature of these currents, the flow from the anterior end to the posterior end should exhibit the same magnitude as the flow

from the posterior to the anterior end. However, their directions are opposite, as illustrated in Fig. 3.1.1

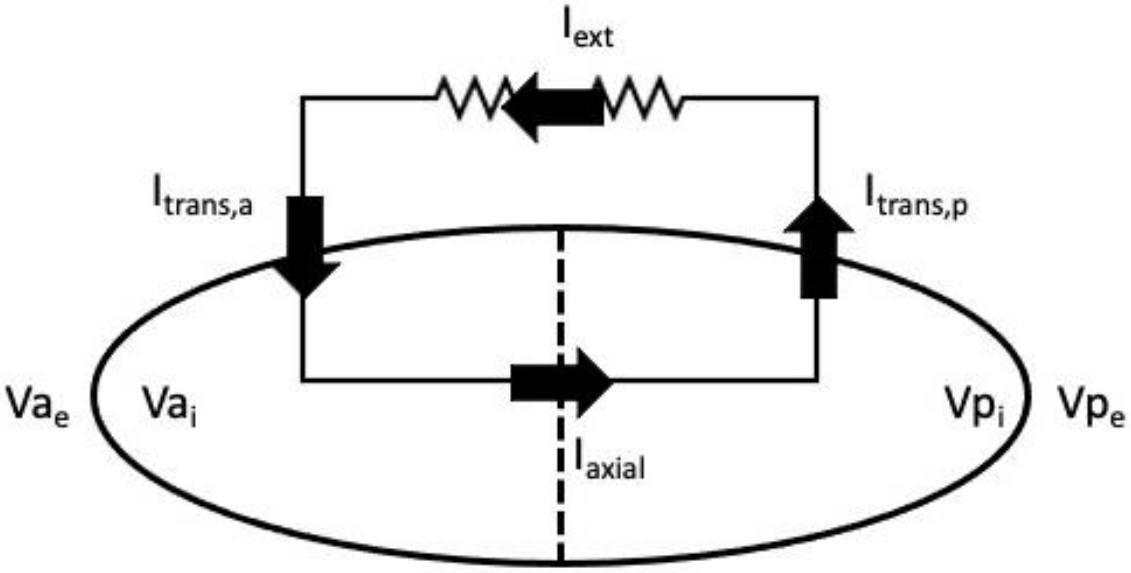

Figure 3.1.1 **PA-CD Model making.** The model resembles a cell with two compartments, like a pair of capacitor junction cells. Va_e and Vp_e represent the exterior membrane voltages of the anterior and posterior compartments, respectively. Va_i and Vp_i are the corresponding membrane internal voltages of the anterior and posterior compartments. The transmembrane potential is computed by subtracting the internal voltage from the exterior voltage (Eqs. (6) and (7)). A close circuit exists between the cell or cell pair and its surrounding environment. External current (I_{ext}), axial current (I_{axial}), and transmembrane current ($I_{tran,a}$, and $I_{tran,p}$) in two compartments are equal in steady state.

The diffusion current is given by:

$$\mathbf{I_{diff} = \frac{-D_{ionX} A F \Delta [ionX]}{x}} \quad (1)$$

With

$$\mathbf{\Delta [ionX] = \Delta [ionX]_a - \Delta [ionX]_p} \quad (2)$$

$$\mathbf{I_{diff,a} = -I_{diff,p}} \quad (3)$$

Where ionX represents Na^+, K^+, or Cl^-, and An^- and Δ [ionX] indicates the concentration difference. D_{ionX} is the diffusion coefficient of ionX. A is the cross-sectional area. F is the

Faraday constant. x is the length between the center of anterior and the center of posterior (see Table 3.1 for values). $I_{diff,a}$ represents the diffusion current flowing from the anterior end to the posterior, whereas $I_{diff,p}$ is the diffusion current that flows from the posterior end to the anterior. The drift current is given by:

$$\mathbf{I_{drift,\,ionX,\,a} = \frac{Z_{ionX} F^2 \Delta V}{RT} \frac{D_{ionX} A [ionX]_{a/p}}{x}} \tag{4}$$

By the Kirchhoff's law, ΔV is given by:

$$\mathbf{\Delta V = V_a - V_p - V_{ext}} \tag{5}$$

With

$$\mathbf{V_a = V_{a,i} - V_{a,e}} \tag{6}$$

$$\mathbf{V_p = V_{p,i} - V_{p,e}} \tag{7}$$

$$\mathbf{I_{drift,\,ionX,\,p} = - I_{drift,\,ionX,\,a}} \tag{8}$$

Where Z_{ionX} is the valence of ionX, and $[ionX]_a$ is the concentration of each ion at the anterior end. V_a, V_p and V_{ext} are the transmembrane potential of anterior end, posterior end, and external voltage. $I_{drift,ionX,a}$ represents the drift current flowing from the anterior end to the posterior, whereas $I_{drift,ionX,p}$ is the drift current that flows from the posterior end to the anterior.

In the purpose of comparison, Axial resistance (R_{axial}) is calculated by Ohm's law. R_{axial} is given by:

$$\mathbf{R_{axial} = \frac{RTx}{DA[ionX]Z_{ionX}^2 e^2 N_A}} \tag{9}$$

3.1.2. $Na^+/2K^+$ ATPase pump current

The formulation of this electrogenic $3Na^+(out)/2K^+(in)$-ATPase is based on the assumption that the extracellular medium is constant, which is as follows (as in Morris et al., 2022; Dijkstra et al., 2016):

$$\frac{I_{NaKpump,a/p}}{I_{maxNaKpump,a/p}} = \frac{0.62}{1+\left(\frac{6.7mM}{[Na^+]_i}\right)} + \frac{0.38}{1+\left(\frac{67.6mM}{[Na^+]_i}\right)^3} \quad (10)$$

With:

$$I_{NaKpump,a/p} = I_{Na,pump,a/p} + I_{K,pump,a/p} \quad (11)$$

$$I_{NaKpump,a/p} = 1/3(I_{Na,pump,a/p}) = -1/2(I_{K,pump,a/p}) \quad (12)$$

$I_{maxNaKpump}$ is the maximum pumping strength, which is dependent on cellular modification. The pump contains two Na^+ binding sites with varying affinities, 6.7 mM and 67.6 mM, respectively. Furthermore,0.62 and 0.38 are the proportions of the receptor protein concentration bound by the ligands.

3.1.3. ATP-consumption

As with the previous CD model, the cost of ATP is computed by the $3Na^+/2K^+$ ATPase pump current, which is given as:

$$\frac{ATP}{s} = I_{NaKpump,a/p}/F \quad (13)$$

3.1.4. Nernst potentials:

The Nernst potential of ionX (Na^+, K^+, or Cl^-) is given by:

$$E_{ionX} = (RT/(Z_{ionX}F)\log([ionX]_e/[ionX]_i) \quad (14)$$

Where Z_{ionX} represents the ions' valence.

3.1.5. Charge difference (CD) model and transmembrane potential

Fraser and Huang introduced the charge difference concept in 2004, providing a valuable tool for studying ion homeostasis. This method facilitates the calculation of transmembrane potential by measuring the absolute quantity of ions crossing the cell membrane, eliminating the need for differential equations, particularly under the assumption of a neutral extracellular environment.

$$V_{a/p} = V_{a/p,i} - V_{a/p,e} \tag{15}$$

$$= FC_{a/p}^{-1}\left(N_{Na,i,a/p}(t) + N_{K,i,a/p}(t) - N_{Cl,i,a/p}(t) - N_{A,i,a/p}\right)$$

$$= FC_{a/p}^{-1}\left(dN_{Na,a/p}(t) + dN_{K,a/p}(t) - dN_{Cl,a/p}(t) - dN_{A,a/p}\right)$$

With

$$dN_{ionX,a/p} = N_{ionX,j,a/p}(t) - N_{ionX,i0,a/p} \tag{16}$$

The number difference of ionX (dN_{ionX}) at the anterior and posterior end can be determined using the difference between the present value $N_{ionX,\,j}$ and a reference value $N_{ionX,\,i0}$, which produces a neutral transmembrane potential due to a neutral intracellular space. Furthermore, the computation is more stable when based on changes in ion number rather than the total amount of ions, N_{ionX} (Morris et al., 2022). At steady-state, transmembrane potential depends on Na^+ and K^+ leak current, which should balance with a given pump strength, diffusion, and drift.

3.1.6. Number of intracellular ions

In line with previous studies (Fraser and Huang, 2004; Dijkstra et al., 2016; Morris et al., 2022), the charge difference model mentioned above computes, at any given time, the change in intracellular ions, expressed as:

$$\frac{dN_{Na,a/p}}{dt} = -F^{-1}\left(I_{Na,leak,a/p} + I_{Na,pump,a/p}\right) - J_N KCC \tag{17}$$

$$\frac{dN_{K,a/p}}{dt} = -F^{-1}\left(I_{K,leak,a/p} + I_{K,pump,a/p}\right) J_{KCl} - J_{NKCC} \tag{18}$$

$$\frac{dN_{Cl,\,a/p}}{dt} = -F^{-1}(I_{Cl,\,leak,\,a/p}) - J_K Cl - J_N KCC \quad (19)$$

3.1.7. Leak current

The leak currents are calculated by the GHK formulation:

$$I_{leak,\,ionX} = P_{leak,\,ionX,\,a/p} F \left(\frac{FV_{a/p}/RT}{1 - e^{-Z_{ionX} FV/RT}} \right) \left([K]_{in} - [K]_{out} e^{-FV/RT} \right) \quad (20)$$

$P_{leak,ionX,a/p}$ is the leak permeability of varied species of ions X at the anterior or posterior.

3.1.8. Transmembrane current

Transmembrane current is the sum of ionic current flows through the cellular membrane:

$$I_{Na,\,trans,\,a/p} = I_{Na,\,leak,\,a/p} + 3I_{Na,\,pump,\,a/p} - FJ_{NaKCl,\,a/p} \quad (21)$$

$$I_{K,\,trans,\,a/p} = I_{K,\,leak,\,a/p} + I_{K,\,pump,\,a/p} + FJ_{Kcl,\,a/p} - FJ_{NaKCl,\,a/p} \quad (22)$$

$$I_{Cl,\,trans,\,a/p} = I_{Cl,\,leak,\,a/p} + FJ_{Kcl,\,a/p} - FJ_{NaKCl,\,a/p} \quad (23)$$

$$I_{trans,\,tot,\,a/p} = I_{Na,\,trans,\,a/p} + I_{K,\,trans,\,a/p} + I_{Cl,\,trans,\,a/p} \quad (24)$$

3.1.9. External voltage

We also anticipate monitoring the cell and its surroundings as a closed circuit. We assume that the transmembrane currents at both ends, the cytoplasmic current, and the external current are equal in the steady state. Consequently, the external voltage (V_{ext}) is calculated by Ohm's law:

$$V_{ext} = -R_{ext} I_{trans} \quad (25)$$

R_{ext} is the external resistance.

3.1.10. Axial voltage

By the Kirchhoff's law, V_{cyt} (EEF) is given as:

$$V_{cyt} = V_a - V_p - V_{cxt} = \Delta V \quad (26)$$

3.1.11. Cell volume

The volume change of a cell is caused by the water flow. Its rates rely on the osmotic gradient across the membrane:

$$J_{H_2O} = \frac{dVol_{cell}}{dt} = P_{H_2O} \Delta\ Osm \tag{27}$$

With

$$\Delta Osm = RT([Sol]_i - [Sol]_e) \tag{28}$$

The effective water permeability of a membrane is P_{H2O}. ΔOsm stands for osmotic gradient. Furthermore, $[Sol]_i$ and $[Sol]_e$ represents the intercellular and extracellular concentration. It is important to note that osmotic ion fluxes, not water flux, determine the volume change rate. It is expected that osmotic gradient equilibration is nearly instantaneous compared to ion fluxes.

3.1.12. Cytoplasmic Donnan effectors

Intracellular anion concentrations are precisely defined using a predefined P_{Na} and P_K. In this instance, $E_{Cl} = V_{a/p}$, as Cl^- is passive.

$$[Cl^-]_i = [Cl^-]_e \frac{FV_{a/p}}{RT} \tag{29}$$

At the steady state, the osmotic balance and neutrality are accomplished. When $[An^-]_i$ need to meet the neutrality:

$$[Na^+]_i + [K^+]_i - [Cl^-]_i - [An^-]_i = -\ \Delta\ conc \tag{30}$$

$\Delta conc$ is the tiny surplus number of anions, which determines the membrane potential.

$$\Delta\ conc = -\ V_{a/p} C_m / FVol_{cell} \tag{31}$$

To meet the requirement of osmotic balance:

$$[Na^+]_i + [K^+]_i + [Cl^-]_i + [An^-] = [Sol]_i = [Sol]_e \tag{32}$$

From the equation above $[An^-]_i$ is given as:

$$[An^-]_i = \frac{[Sol]_i + \Delta\ conc}{2} - [Cl^-]_i \qquad (33)$$

3.1.13. K/Cl co-transporter

K/Cl co-transporter is a protein involved in membrane transport. Positively charged K+ is carried with negatively charged Cl^- to preserve electroneutrality. The direction of the net movement of K^+ and Cl^- is solely determined by the sum of their respective chemical potential gradients. There are at least four isoforms of K/Cl: KCC1, KCC2, KCC3, and KCC4. KCC1 is the most ubiquitous KCC isoform. We suspect the isoform in our model is KCC1. J_{KCl} is the electrochemically produced ion flow mediated by k/Cl cotransporters; it is represented in a Nernst-like manner (Dijkstra et al., 2016; Morris et al., 2022; Østby et al., 2009):

$$J_{KCl} = U_{KCl}\frac{RT}{F}\ln\left[\frac{[K^+]_i[Cl^-]_i}{[K^+]_e[Cl^-]_e}\right] \qquad (34)$$

U_{KCl} is the maximum flux capacity of K/Cl co-transporter.

3.1.14. NKCC co-transporter

NKCC co-transporter is a membrane transport protein. It enhances the secondary active transport of Na^+, K^+, and Cl^- into cells. To maintain electroneutrality, positively charged Na^+ and K^+ are transported alongside two negatively charged Cl^-. There are two isoforms of NKCC: NKCC1 and NKCC2. NKCC2 is exclusively found in the kidney, whereas NKCC1 is present in practically all cell types (Russell, 2000). We suspect that the isoform in our model is NKCC1. J_{NKCC} is also electrochemically produced in a flux in a Nernst-like fashion. The equation is as stated by earlier studies (Østby et al., 2009):

$$J_{NKCC} = U_{NKCC}\frac{RT}{F}\ln\left[\frac{[Na^+]_i[K^+]_i([Cl^-]_i)^2}{[Na^+]_e[K^+]_e([Cl^-]_e)^2}\right] \qquad (35)$$

U_{NKCC} is the maximum flux capacity of K/Cl co-transporter.

Table 3.1 **Parameter values of PA-CD steady-state and variants.**

	Unit	**Posterior Anterior-Charge Difference Model**	
Parameter		**Posterior**	**Anterior**
C_m	pF	20	20
SA (from C_m)	μm^2	2000	2000
R	J/mol•K	8.3144598	8.3144598
T	K	310	310
F	C/mol	96.485333	96.485333
A	m^2	1×10^{-5}	1×10^{-5}
L	m	2×10^{-10}	2×10^{-10}
$D_{permeant\ ions}$	m^2/s	9×10^{-11}	9×10^{-11}
$D_{impermeant\ ions}$	m^2/s	9×10^{-14}	9×10^{-14}
P_{Na}	μm^3 / s	1.51	1.51
P_K	μm^3 / s	20	20
P_{Cl}	μm^3 / s	2.5	2.5
P_{Na}: P_K: P_{Cl}		0.0775:1:0.125	0.0775:1:0.125
Impedance^{-1}	Summed P_{ionX}	24.01	24.01
P_{H2O}	μm^3 / s	2	2
N_{Ai}	fmol	290500	290500
$I_{MaxNaKpump}$	pA	54.5	54.5
Electrolytes(mM): fixed [extracellular] and calculated (intracellular) concentration			
$[sol]_{e,i}$	mM	[310]&(310)	[310]&(310)
$[Na^+]_{e,i}$	mM	[152]&(7.84)	[152]&(7.84)
$[K^+]_{e,i}$	mM	[3]&(147.16)	[3]&(147.16)
$[Cl^-]_{e,i}$	mM	[135]&(9.74)	[135]&(9.74)
$[An^-]_{e,i}$	mM	[20]&(145.26)	[20]&(145.26)
Calculated Steady-State values			
Vol_{cell}	μm^3	2000	2000
MP	mV	-70.22	-70.22

$[sol]_i$	mM	Ω310	310
E_{Na}	mV	79.2	79.2
E_k	mV	-103.99	-103.99
E_{Cl}	mV	-70.22	-70.22
$I_{Na,leak}$(St-St)	pA	-62.51	-62.51
ATP/s(St-St)	amol/s	216.24	216.24
$Ccy_{ref.}$	m^3 / s	4.5×10^{-6}	4.5×10^{-6}
R_{ext}	MΩ	1	

3.2. Endogenous Electric Fields caused by symmetry breaking:

3.2.1. Symmetry breaking in the minimal PA-CD

3.2.1.1. Symmetry breaking by changing $P_{leak,Na}$ in minimal PA-CD

In the PA-CD model, Nernst-Planckian diffusion and drift connect the anterior and posterior compartments, making it a one-dimensional model. When the two compartments are symmetrical, the cell can be considered as a single compartment. Moreover, the total impedance of increasing $P_{leak,Na}$ by 1.5 times at both ends and only doubling $P_{leak,Na,a}$ at the anterior end is the same. However, the $P_{leak,Na}$:$P_{leak,K}$ ratios of the two compartments are different under these two perturbations. As opposed to the symmetrical cell with 1.5 times $P_{leak,Na}$ at both ends, the steady state of the two compartments will differ in the case of double $P_{leak,Na,a}$ at the anterior end, resulting in the generation of an Endogenous Electric Field (EEF) by symmetry breaking.

The PA-CD uses the pump-leak Donnan ion homeostasis process. These Donnan effectors (impermeant anions) are negatively charged protein molecules. They are distributed unevenly across the membrane (Düsterwald et al., 2018). With symmetry breaking by doubling $P_{leak,Na,a}$ at the anterior, the system can achieve a steady state with 0% and 50% mobile impermeable anions (Fig. 3.2.1). When 50% of the impermeant anions are mobile, the difference in volume between the two compartments is significantly greater than when there is 0% mobility (Figs. 3.2.1 A2 and B2). However, with 100% mobile impermeable anion mobility, the system has not yet reached a steady state after 500,000 seconds (Fig. 3.2.1 C2). With 100% anion mobility, almost all the ions and water (cytosol) from the posterior compartment ultimately flow into the other compartment. Although the system can eventually reach a steady state, this seems unlikely (not shown in the figure). Thus, to better mimic the cellular physiology, the conducted tests are performed with 50% anion mobility.

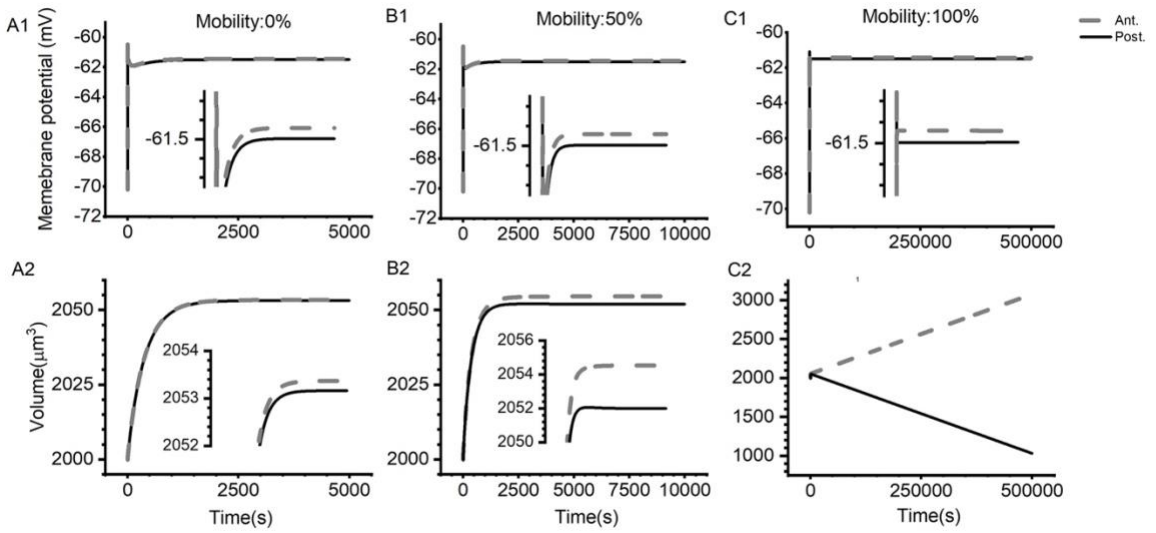

Figure 3.2.1 **Breaking symmetry by doubling $P_{leak,Na,a}$ at the anterior end with 0%, 50%, and 100% internal impermeant anions' mobilities. A1-A2**: Symmetry breaking with 0% internal impermeant anions' mobilities. A1: Transmembrane potential A2: Volume **B1-B2**: Symmetry breaking with 50% internal impermeant anions' mobilities. B1: Transmembrane potential B2: Volume **C1-C2**: Symmetry breaking with 100% internal impermeant anions' mobilities. C1: Transmembrane potential C2: Volume The system can attain a steady state with 0% to 50% impermeable anion. However, with 100%, the system has not yet reached a stable state even after 500000s. In this situation, the system can ultimately attain a steady state. However, the number seems implausible (not shown).

When $P_{leak,Na,a}$ is doubled (with 50% mobile impermeable), ATP consumption in both compartments increases by approximately 1.35-fold, with the anterior end consuming slightly more ATP than the posterior end, at 292.6 amol/s and 290.6 amol/s, respectively (Fig. 3.2.2 C). It is an example of active feedback, with the system detecting changes in $[Na^+]_i$ and adjusting the ATP-fueled Na^+ efflux and K^+ uptake rates of the $3Na^+/2K^+$ pumps accordingly. ATP calculation depends on pump current (I_{pump}). A larger $P_{leak,Na,a}$ increases Na^+ leak current ($I_{Na,\ leak}$). Thus, I_{pump} rises to compensate for $I_{Na,\ leak}$. The two compartments are closely linked through diffusion and drift. With excess Na^+ from the anterior end flowing into the posterior end, the posterior pump works harder (Fig. 3.2.3 A) and posterior ATP increases.

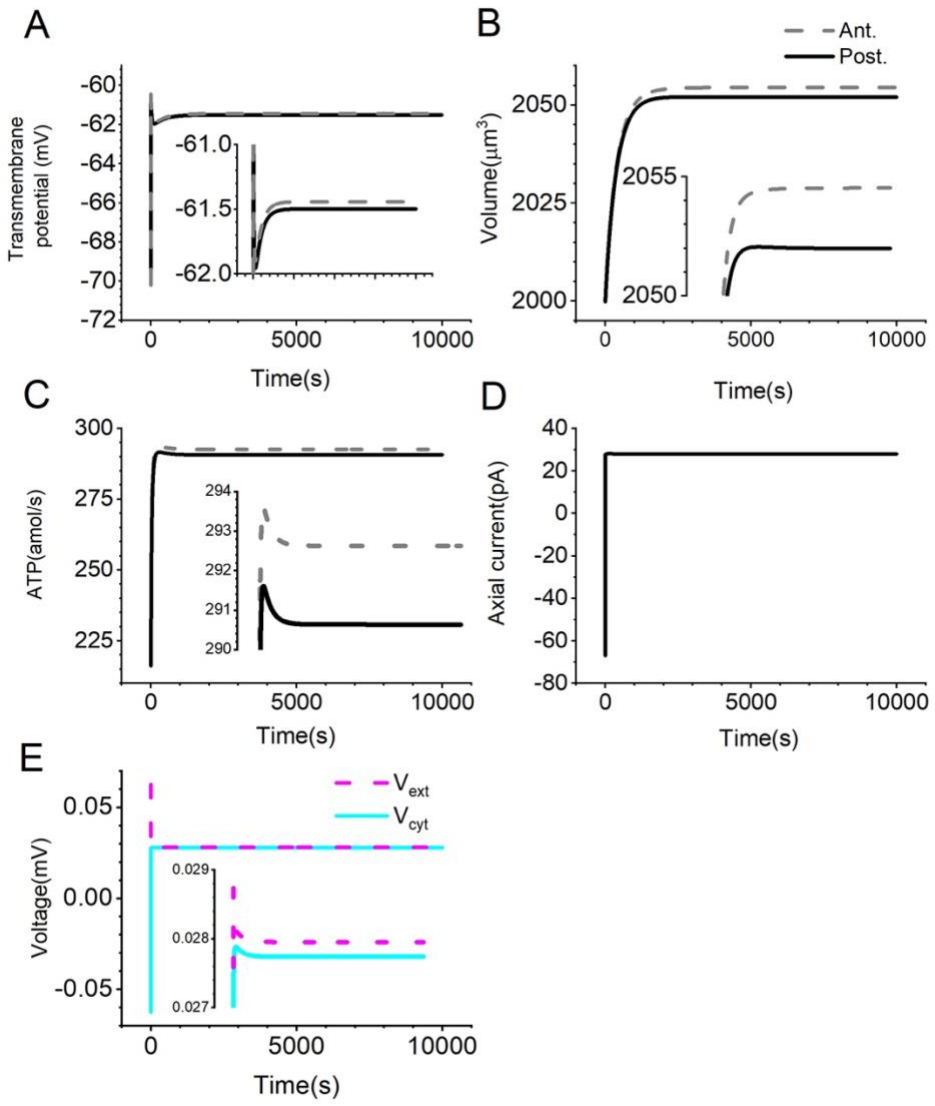

Figure 3.2.2 **Breaking symmetry by doubling $P_{leak,Na,a}$ at the anterior end with 50% internal impermeant anions' mobilities.** **A**: Transmembrane potential, **B**: Volume, **C**: ATP, **D**: Axial current, and **E**: cytoplasmic (axial) voltage and external current

The change in volume is primarily due to passive feedback (Fig. 3.2.2 B). The Donnan effectors and the $P_{leak,Cl}$ in a water-permeable membrane detect changes in osmotic balance and neutrality. With the $P_{leak,Na}$:$P_{leak,K}$ ratios selected, they counteract any osmo-imbalance and maintain cytoplasmic neutrality, and the chloride Nernst potential (E_{Cl}) should equal the MP in a minimal system. Under this condition, the $[Cl^-]_i$ is uniquely determined by the MP (Eq. (29)). At the steady state, the diffusion current balances the drift current for each compartment (Fig. 3.2.5 C).

Additionally, the sustained I_{axial} is 28 pA (Fig. 3.2.2 D), with an EEF of 2.8 V/ m (Fig. 3.2.2 E). When the $P_{leak,Na,a}$ is doubled, the $P_{leak,Na,a}$:$P_{leak,K,a}$ ratio increases, and as a result, the MPs of both highly connected compartments depolarize (Fig. 3.2.2 A). The anterior end has a higher $P_{leak,Na}$:$P_{leak,K}$ ratio, resulting in a slightly more depolarized MP compared to the posterior end.

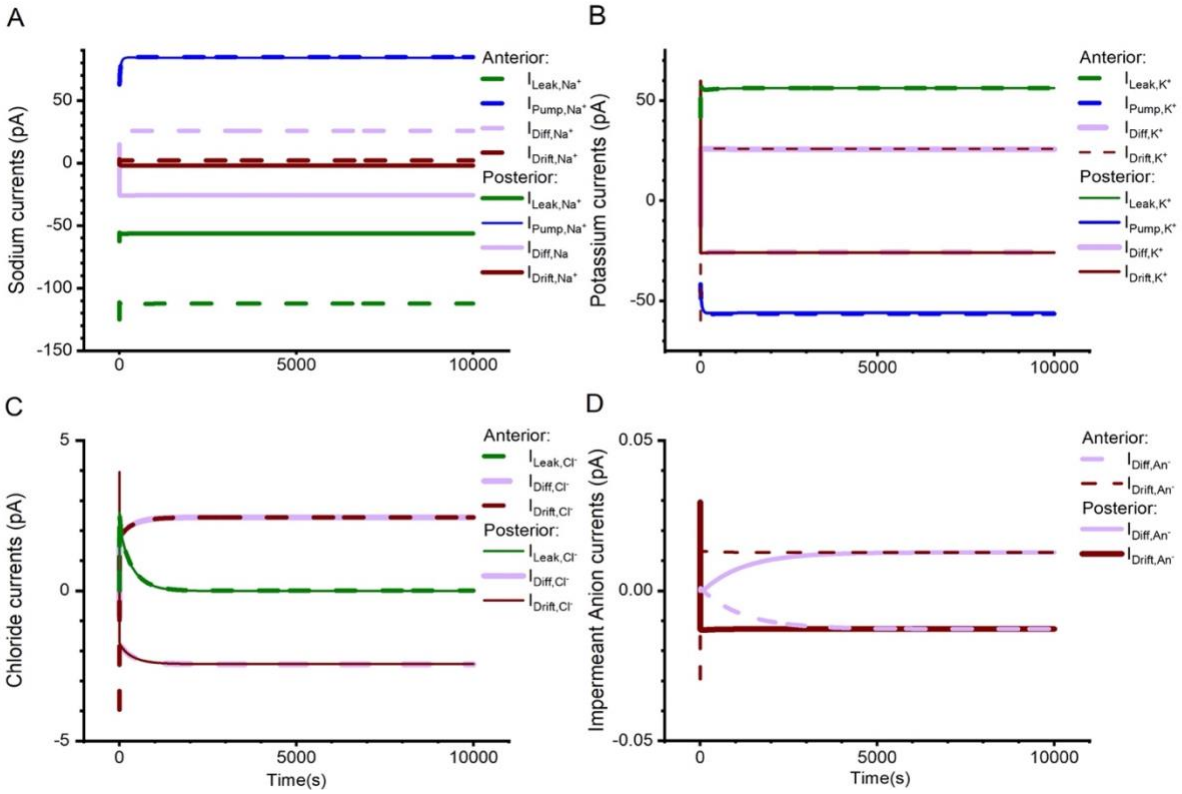

Figure 3.2.3 **Currents with symmetry breaking by doubling $P_{leak,Na,a}$ at the anterior end with 50% impermeable anions. A**: An increased $P_{leak,Na,a}$ at the anterior end leads to an increase in $I_{Na,leak}$, causing the pump current (I_{pump}) to rise and compensate for the $I_{Na,leak}$. The two compartments are closely linked through diffusion and drift, and the excess Na^+ at the anterior end flows to the posterior end, requiring the pump at the posterior end to work harder. **B**: Our pump is a $3Na^+/2K^+$ pump, meaning that when the system expels three Na^+, it will bring in two K^+. Increasing the leak current of K^+ balances out the excess K^+. The K^+ drift and diffusion currents internally nullify each other, and the diffusion currents of impermeant anions balance their drift current for each compartment. **C**: The chloride drift current is driven by the cytoplasmic voltage. The chloride leak current is indirectly driven by the transmembrane potential. At a steady state, the chloride diffusion current balances the chloride drift and leak currents at each compartment. **D**: The drift current for impermeable anions is driven by V_{cyt}, followed by the diffusion current.

3.2.1.2. Symmetry breaking by changing the $P_{leak,K}$ in minimal PA-CD

If the permeability of potassium at the anterior end ($P_{leak,K,a}$) is reduced by a factor of 0.5, the $P_{leak,Na,a}$:$P_{leak,K,a}$ ratio increases, resulting in a simultaneous depolarization of the transmembrane potentials in these highly interconnected compartments. The MP at the anterior end becomes more depolarized due to its higher $P_{leak,Na,a}$:$P_{leak,K,a}$ ratio (Fig. 3.2.4 A). This asymmetry between the compartments results in an Iaxial of approximately 13 pA and a V_{cyt} with endogenous electric field (EEF) of approximately 1.3V/m (Figs. 3.2.4 D and E).

$P_{leak,K}$ is the primary permeability. Reducing $P_{leak,K,a}$ at the anterior end by half results in a drop in $I_{K,leak,a}$ (Fig. 3.2.4 F). The excess K^+ drifts and diffuses towards the posterior end. It causes an influx of Cl^- and water to maintain neutrality and osmotic balance. Thus, this influx leads to an increase in the volumes of both compartments (Fig. 3.2.4 B).The influx of Cl^- also causes an increase in $[Cl^-]_i$, while the influx of water causes a decrease in $[An^-]_i$ due to the fixed total amount of impermeant (Fig. 3.2.4 C).

Cells may generate an EEF by a symmetry breaking of $P_{leak,Na}$ or $P_{leak,K}$. The effects of doubling the $P_{leak,Na,a}$:$P_{leak,K,a}$ ratio by either a 2-fold increase in $P_{leak,Na,a}$ or a 0.5-fold decrease in $P_{leak,K,a}$ are different. Symmetry breaking by holding $P_{leak,Na}$ or $P_{leak,K}$ constant at the anterior end resulted in nonlinear variations in MPs in response to changes in $P_{leak,Na,a}$:$P_{leak,K,a}$ ratio. Additionally, as previously noted, Na^+ fluxes control K^+ fluxes, and Na^+ leak current is the rate-limiting factor in achieving a steady state following perturbation (Morris et al., 2022).

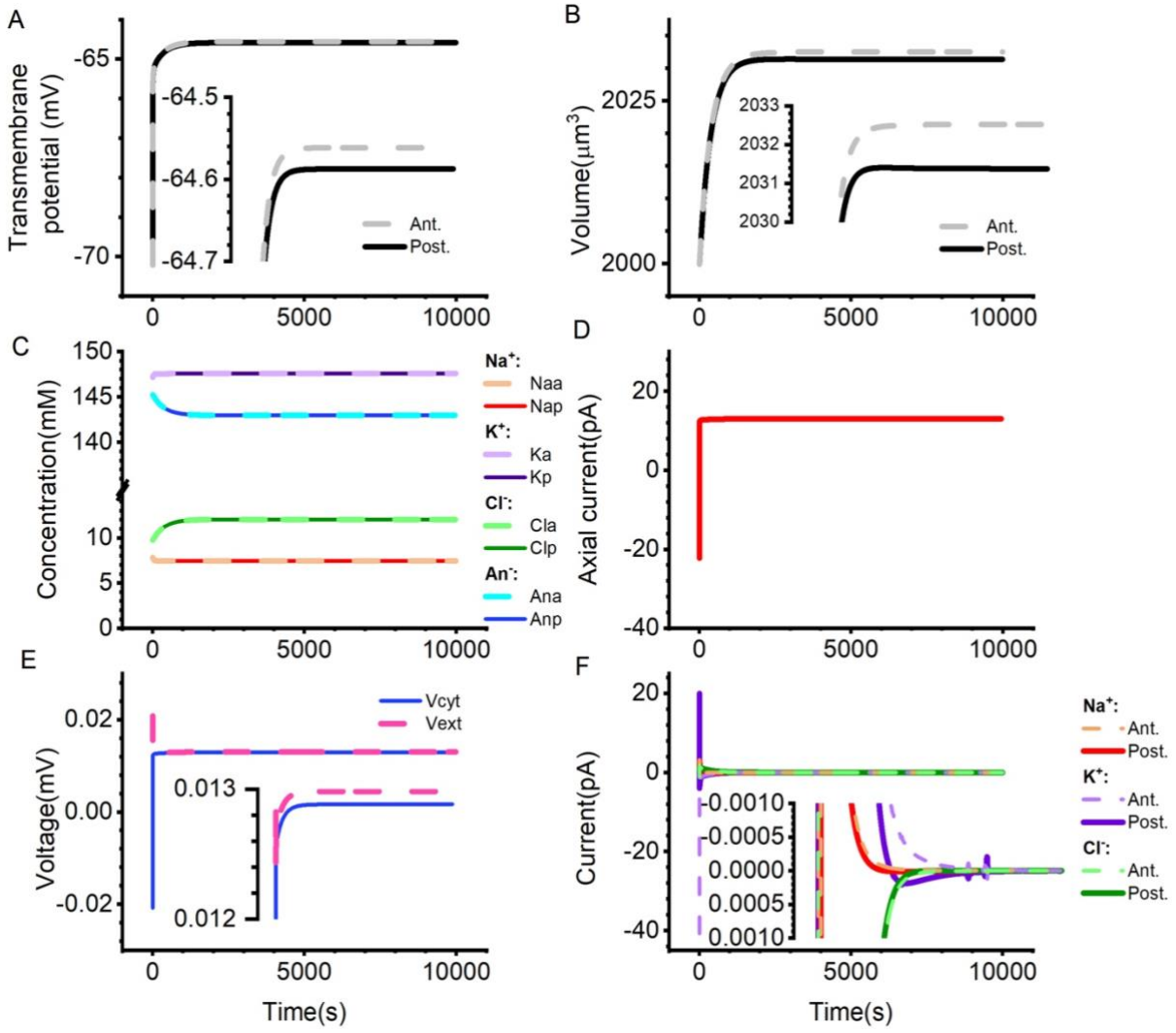

Figure 3.2.4 **Breaking symmetry by decreasing $P_{leak,K,a}$ by 0.5-fold with impermeable anions having 50% mobility. A**: Transmembrane potential, **B**: Volume, **C**: Internal Ion Concentration, **D**: Axial current, **E**: cytoplasmic (axial) voltage and external current, and **F**: Total currents of different ions.

3.2.1.3. symmetry breaking by changing the $P_{leak,Cl}$ in minimal PA-CD

In the PA-CD model, a 0.5-fold or 2-fold change in $P_{leak,Cl,a}$ at the anterior end has no effect on the steady-state (Fig. 3.2.5). Cl^- transport is purely passive because of the minimal pump-leak dominated system. In this case, Cl^- settles its gradient across the membrane according to the transmembrane potential. Since $P_{leak,Na}$:$P_{leak,K}$ ratios on both compartments remain constant, the MPs on both ends don't change (Fig. 3.2.5A). The electro-diffusion driving force on Cl^- is zero. There is no axial current (Fig. 3.2.5C) and EEF (Fig. 3.2.5D).

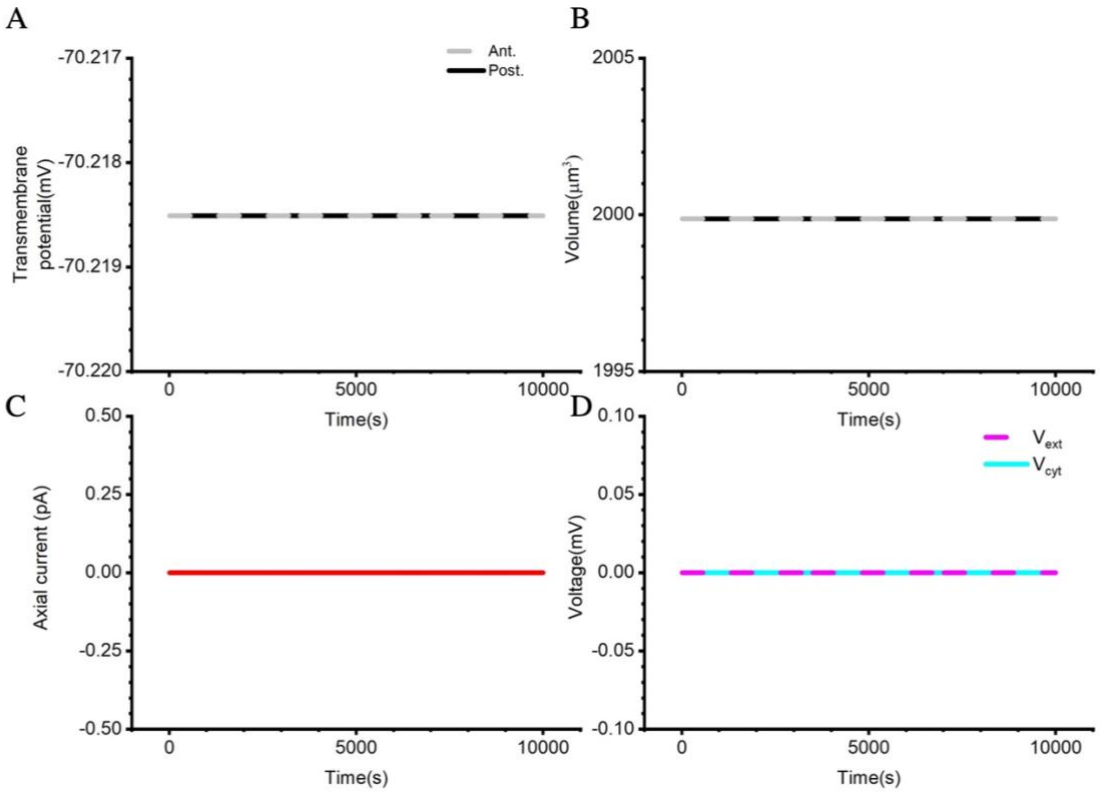

Figure 3.2.5 **Breaking symmetry by altering $P_{leak,Cl,a}$ at the anterior end. A:** Transmembrane potential, **B:** Voltage, **C:** Axial current, and **D:** Voltage**.** Neither a 2-fold increase nor a 0.5-fold decrease in $P_{leak,Cl,a}$ has any effect on the steady state parameters.

3.2.2. Symmetry breaking in non-minimal PA-CD

3.2.2.1. Adding cotransporters in the PA-CD (non-minimal system).

Adding chloride-cations cotransporters, such as $Na^+K^+2Cl^-$ cotransporter (NKCC) and K^+/Cl^- cotransporter (K/Cl), makes the PA-CD model nonminimal. The results of PA-CD with these cotransporters are shown in Table 3.3.

Table 3.2 **PA-CD with a minimal or a nonminimal steady state.**

	Unit	**Minimal system (ant/post)**	**+ K/Cl (ant/post)**	**+ NKCC (ant/post)**	**+ K/Cl & NKCC (ant/post)**
$[Na^+]_i$	mM	7.84 / 7.84	7.93/ 7.93	8.18/ 8.18	8.54/ 8.54
$[K^+]_i$	mM	147.16 / 147.16	147.07/ 147.07	146.82/ 146.82	146.45/ 146.45
$[Cl^-]_i$	mM	9.74 / 9.74	5.76/ 5.76	31.69/ 31.69	24.34/ 24.34
$[An^-]_i$	mM	145.26 / 145.26	149.24/ 149.24	123.31/ 123.31	130.66/ 130.66
E_{Na}	mV	79.19 / 79.19	78.90/ 78.90	78.06/ 78.06	76.91/ 76.91
E_K	mV	-103.99 / -103.99	-103.98/ -103.98	-103.93/ -103.93	-103.87/ -103.87
E_{Cl}	mV	-70.22 / -70.22	-84.24/ -84.24	-38.71/ -38.71	-45.76/ -45.76
MP	mV	-70.22 / -70.22	-71.35/-71.35	-65.38 / -65.38	-67.30/-67.30
Vol.	μm^3	1999.88 / 1999.88	1946.54 / 1946.54	2355.82 / 2355.82	2223.35/2223.35
ATP	amol/s	216.24 / 216.24	219.04/ 219.04	226.69 / 226.69	236.99 / 236.99

In the case of K/Cl cotransporter, the steady-state with a uniform cell shows reduced volume (Fig. 3.2.6 B), polarized MP (Fig. 3.2.6 A), increased $[Na^+]_i$ and $[An^-]_i$, and decreased $[K^+]_i$ and $[Cl^-]_i$ (Fig. 3.2.6 C). The K/Cl flux (J_{KCl}) is determined by the chemical potential differences of K^+ and Cl^-. Due to the higher potassium concentration inside the cell compared to the exterior, there is a K^+ gradient across the membrane. This gradient creates an outward-oriented chemical gradient for K^+ and results in the accompanied passive efflux of Cl^-. To maintain osmotic balance, the cell undergoes shrinkage. The K^+ gradient depends on the activity

of the Na^+/K^+ ATPase, and the introduction of the K/Cl cotransporter increases ATP consumption (Fig. 3.2.6 E).

Furthermore, the significant decrease in $[K^+]_i$ causes the E_K to become more depolarized, leading to a more depolarized MP. As the two compartments are identical, I_{axial} is zero, and there are no EEF (Figs. 3.2.6 F and D).

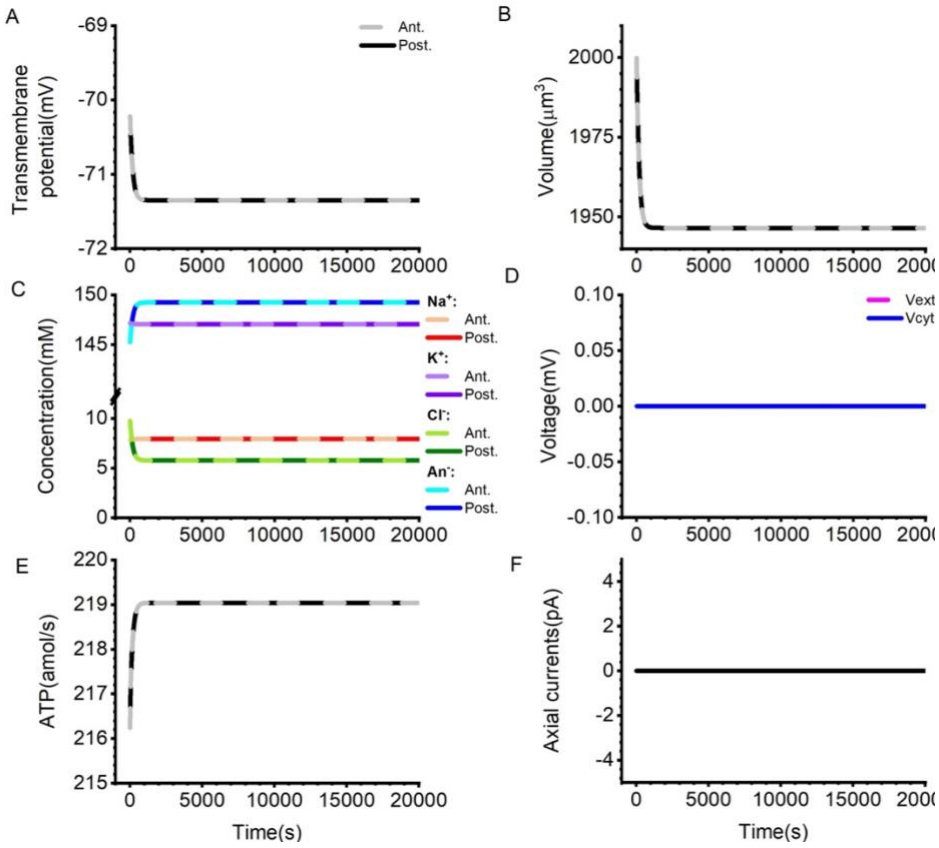

Figure 3.2.6 **PA-CD with K/Cl at steady state. A**: Transmembrane potential, **B**: Volume, **C**:Internal Ion Concentration, **D**: cytoplasmic (axial) voltage and external current, **E**:ATP, and **F**: Axial current. The steady states of two compartments change with K/Cl. There is no EEF because of two identical compartments.

When the NKCC cotransporter is introduced, the uniform cell reaches a new steady state characterized by an increased volume (Fig. 3.2.7 B), a more depolarized MP (Fig. 3.2.7A), a rise in $[Na^+]_i$ and $[Cl^-]_i$, and a reduction in $[K^+]_i$ and $[An^-]_i$ (Fig. 3.2.7 C). The NKCC cotransporter utilizes the Na^+ gradient to generate Na^+, K^+, and Cl^- influxes in a ratio of 1:1:2, producing an electrically neutral current.

To maintain osmotic balance, the cell swells. The introduction of the NKCC cotransporter results in the Na^+/K^+ ATPase working harder, leading to an increase in ATP

consumption (Fig. 3.2.7 E). In addition, the introduction of the NKCC cotransporter results in a significant increase in $[Cl^-]_i$, which leads to the depolarization of E_{Cl}. As a result, the membrane depolarization is dominated by this depolarized E_{Cl}. It is worth noting that the primary function of NKCC in the most non-excitable tissues is volume regulation (Russell, 2000; Fraser and Huang, 2004), which explains why the stimulation of NKCC has a greater effect on cell volumes than its effect on MP.

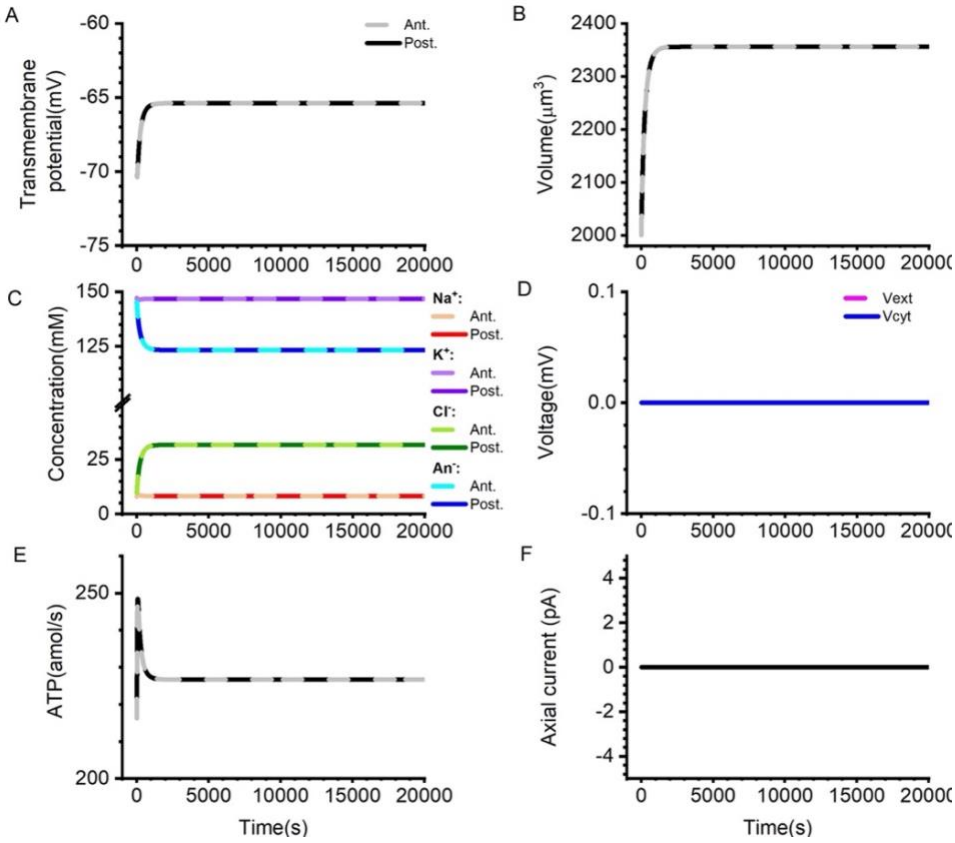

Figure 3.2.7 **PA-CD with NKCC at steady state. A**: Transmembrane potential, **B**: Volume, **C**:Internal Ion Concentration, **D**: Cytoplasmic (axial) voltage and external current, **E**: ATP, and **F**: Axial current. The steady states of two compartments change with NKCC. There is no EEF because of two identical compartments.

If K/Cl and NKCC cotransporters coexist in a cell, the effect depends on the K/Cl: NKCC ratio. In the proposed system, the NKCC cotransporter dominates, resulting in a larger cell volume (Fig. 3.2.8 B), a more polarized MP (Fig. 3.2.8 A), increased $[Na^+]_i$ and $[Cl^-]_i$, and decreased $[K^+]_i$ and $[An^-]_i$ (Fig. 3.2.8 C) in steady state. However, the coexistence of K/Cl with NKCC causes the cell to be less polarized and shrunken than with NKCC alone. Additionally,

since these two cotransporters indirectly utilize the Na^+/K^+ ATPase, their ATP consumption is greater than that of K/Cl or NKCC alone (Fig. 3.2.8 E).

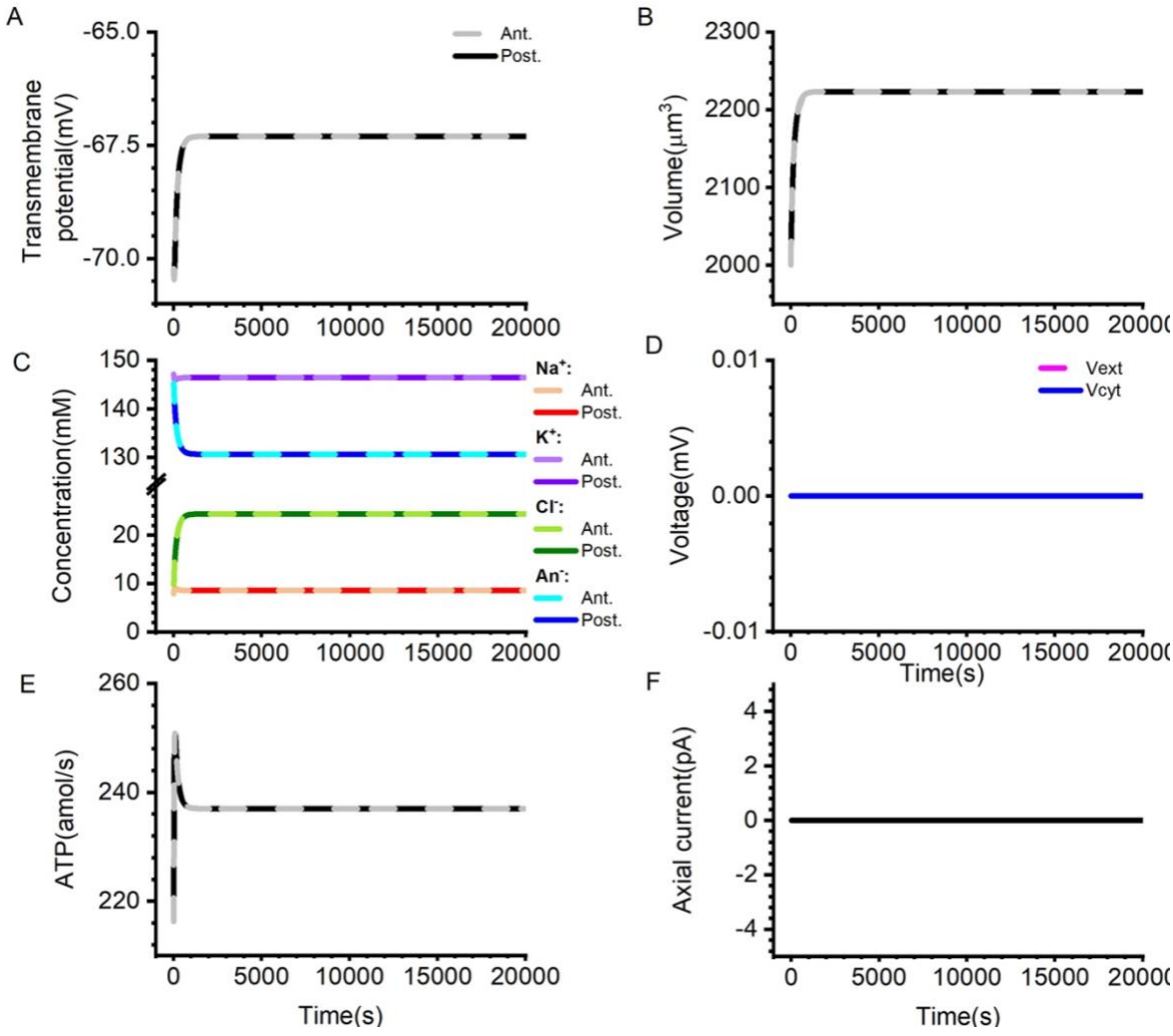

Figure 3.2.8 **PA-CD with K/Cl and NKCC at steady state. A**: Transmembrane potential, **B**: Volume, **C**: Internal Ion Concentration, **D**: Cytoplasmic (axial) voltage and external current, **E**: ATP, and **F**: Axial current. The steady states of two compartments change with K/Cl and NKCC. There is no EEF because of two identical compartments.

3.2.2.2. Symmetry breaking in non-minimal PA-CD.

In a non-minimal system, the resulting steady-state values symmetry breaking by doubling $P_{leak,Na,a}$ at the anterior end is comparable to those of a minimal system. The steady-state values for K/Cl, NKCC, or K/Cl and NKCC are in Table 3.4.

Table 3.3 **Parameter values of doubling $P_{leak,Na,a}$ at the anterior end with a minimal or a non-minimal steady state.**

2× P_{Na} at ant.	**Unit**	**Minimal system (ant/post)**	**+ K/Cl (ant/post)**	**+ NKCC (ant/post)**	**+ K/Cl & NKCC (ant/post)**
Volume	μm^3	2054.53 / 2051.99	1972.17 / 1969.88	2374.61 / 2371	2231.46 / 2228.35
Δ Vol.	μm^3	2.54	2.29	3.61	3.11
MP	mV	-61.44/ -61.50	-62.64 / -62.69	-58.22/ -58.28	-59.71 / -59.76
V_{cyt}	mV	0.02774	0.02816	0.02660	0.02711
I_{axial}	pA	27.95	28.37	26.85	27.35
ATP	amol/s	292.63 / 292.63	296.83 / 296.83	298.59 / 298.59	301.71 / 307.71

The MPs of symmetry breaking with cotransporters are illustrated in Fig. 3.2.9 A, Fig. 3.2.10 A, and Fig. 3.2.11 A. The MPs primarily depend on the $P_{leak,Na}$:$P_{leak,K}$ ratio in a non-minimal system. Therefore, doubling $P_{leak,Na,a}$ changes this ratio and leads to membrane depolarization. In the case of symmetry breaking with K/Cl, the MPs are less depolarized (Fig. 3.2.9 A) since K/Cl brings E_{Cl} closer to E_K. However, with the introduction of NKCC or NKCC-dominated cooperation with K/Cl, the MPs are more depolarized (Fig. 3.2.10 A, and Fig. 3.2.11 A) due to E_{Cl} being significantly more depolarized.

All nonminimal systems with a doubled $P_{leak,Na,a}$ experience an increased Na^+ inflow, resulting in a rise in $[Na^+]_i$. The rise in $[Na^+]_i$ is greater with K/Cl due to the cell's shrinkage (Figs. 3.2.9 B and C). However, even with Na^+ inflow via NKCC, the $[Na^+]_i$ is reduced by the increase in cell volume (Figs. 3.2.10 B and C). Furthermore, increased Na^+ leakage increases pump activity, leading to an increase in ATP consumption under these three conditions. Compared to steady state with a minimal system, NKCC dominated cooperation with K/Cl

results in the largest increase in ATP consumption (Fig. 3.2.11 E), followed by NKCC (Fig. 3.2.10 E) and K/Cl alone (Fig. 3.2.9 E). Additionally, the difference in volume between the two compartments decreases with K/Cl effluxes and increases with NKCC influxes (Fig. 3.2.9 B and Fig. 3.2.10 B).

In the non-normal system with doubled P_{Na} at the anterior end, a steady-state I_{axial} (Fig. 3.2.9 F, Fig. 3.2.10 F, and Fig. 3.2.11 F) and sustained EEF (Fig. 3.2.9 D, Fig. 3.2.10 D, and Fig. 3.2.11 D) are present. In these three nonminimal systems, change in I_{axial} and V_{cyt} is minimal. I_{axial}s and V_{cyt}s are comparable to the minimal system with doubled $P_{leak,Na,a}$. Thus, cotransporters have a negligible impact on the size of EEF. The highly connected compartments and the compartmental uniformity of cotransporter could cause unsignificant changes.

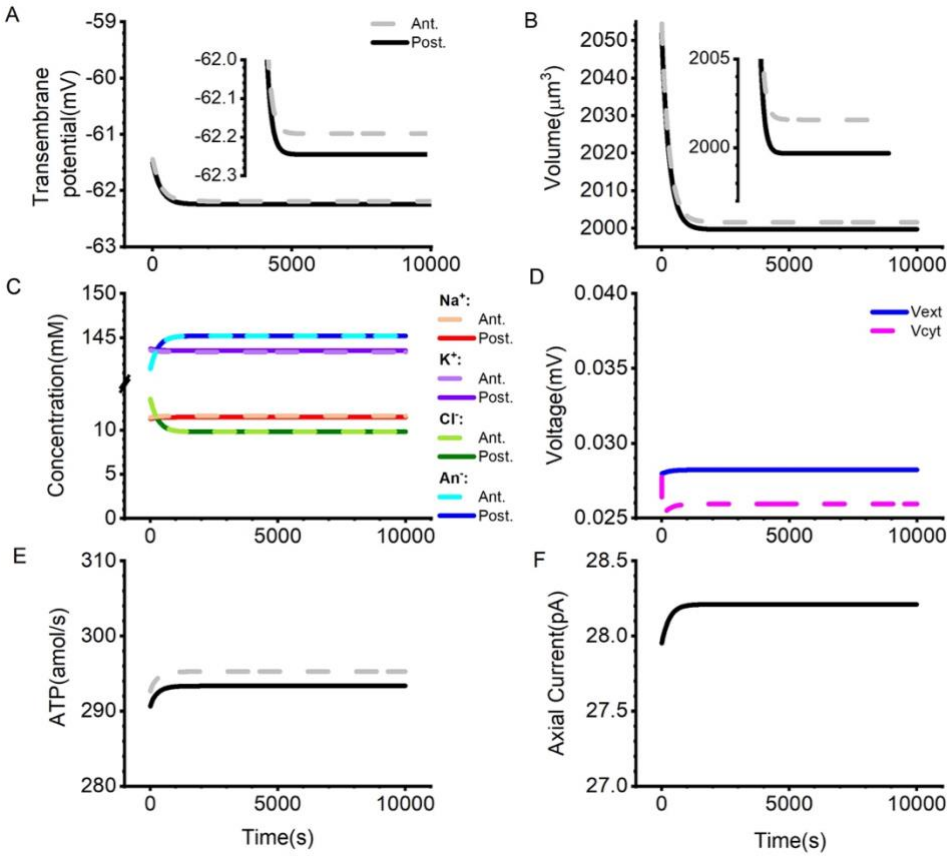

Figure 3.2.9 **Breaking symmetry by doubling $P_{leak,Na,a}$ at the anterior with co-transporter K/Cl.** The initial points in each plot are the steady state with doubled P_{Na} in a minimal system. **A**: Transmembrane potential, **B**: Volume, **C**: Internal Ion Concentration, **D**: cytoplasmic (axial) voltage and external current, **E**: ATP, and **F**: Axial current.

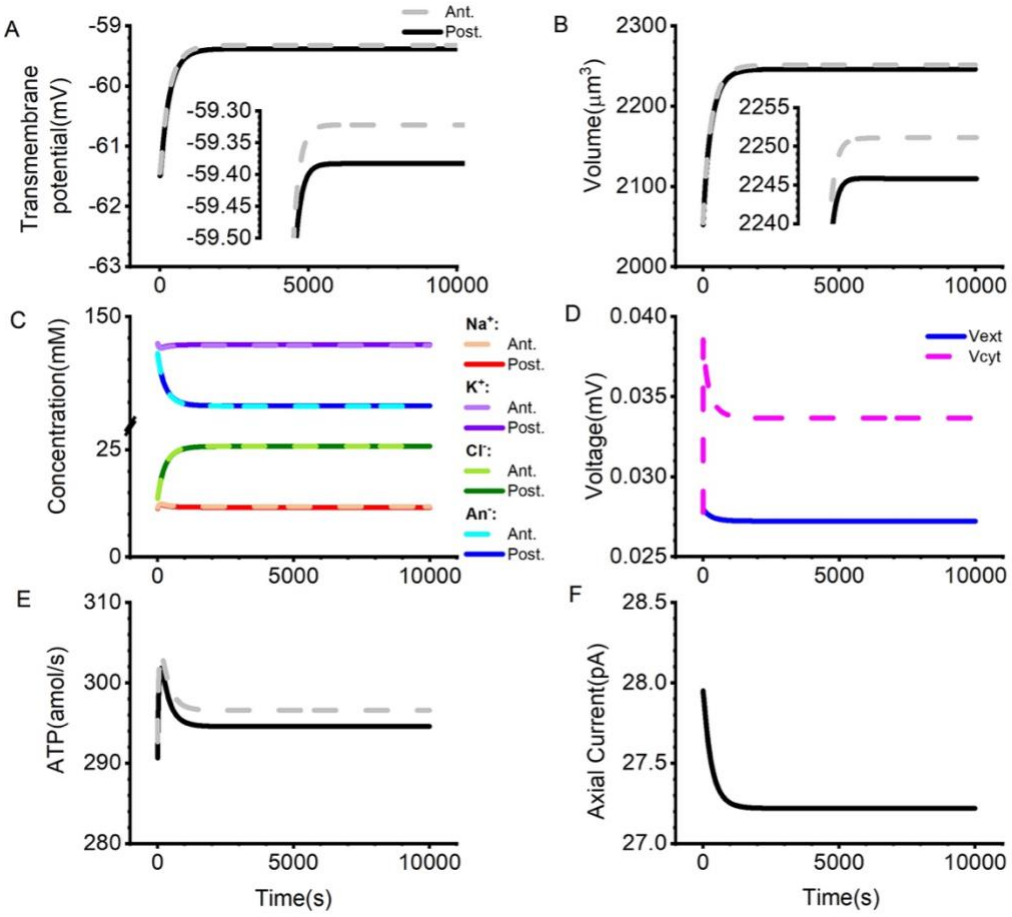

Figure 3.2.10 **Breaking symmetry by doubling $P_{leak,Na,a}$ at the anterior with co-transporter NKCC.** The initial points in each plot are the steady state with doubled P_{Na} in a minimal system. **A**: Transmembrane potential, **B**: Volume, **C**: Internal Ion Concentration, **D**: Cytoplasmic (axial) voltage and external current, **E**: ATP, and **F**: Axial current.

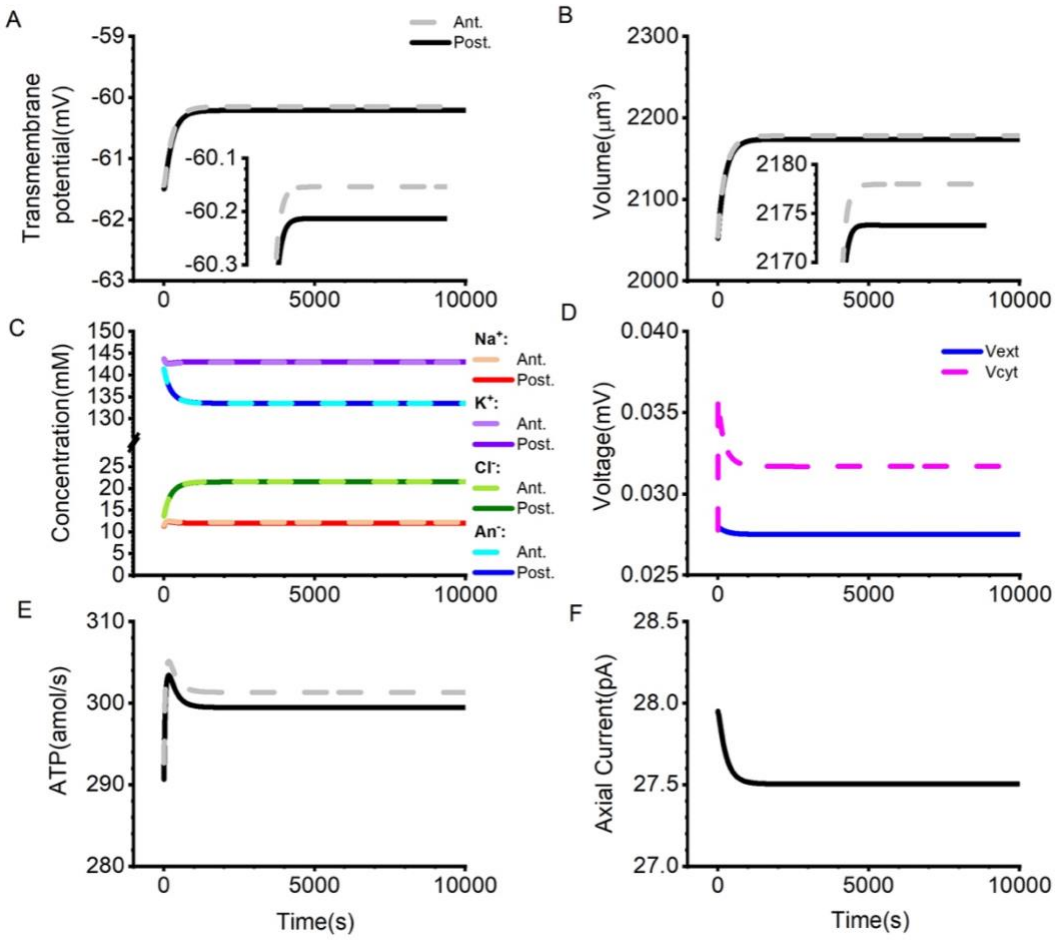

Figure 3.2.11 **Breaking symmetry by doubling $P_{leak,Na,a}$ at the anterior with co-transporter K/Cl and NKCC.** The initial points in each plot are the steady state with doubled P_{Na} in a minimal system. **A**: Transmembrane potential, **B**: Volume, **C**: Internal Ion Concentration, **D**: Cytoplasmic (axial) voltage and external current, **E**: ATP, and **F**: Axial current.

Furthermore, modifying $P_{leak,Cl}$ at one end in the non-minimal system can impact the steady state, as demonstrated by doubling $P_{leak,Cl,a}$ at the anterior with K/Cl (Fig. 3.2.12). The results of doubled $P_{leak,Cl,a}$ at the anterior end with K/Cl cotransporter are in Table 3.5.

Table 3.4 **Parameter values of doubling $P_{leak,Cl,a}$ with a nonminimal steady state.**

	Unit	Minimal system (ant/post)	+ K/Cl (ant/post)	+ K/Cl (ant/post) with $2P_{Cl,\ ant}$
$[Na^+]_i$	mM	7.84 / 7.84	7.928/ 7.928	7.943/7.943
$[K^+]_i$	mM	147.16 / 147.16	147.068/ 147.068	147.053/147.053
$[Cl^-]_i$	mM	9.74 / 9.74	5.765/ 5.765	6.509/6.503
$[An^-]_i$	mM	145.26 / 145.26	149.235/149.235	148.491/148.491
E_{Na}	mV	79.19 / 79.19	78.899/ 78.899	78.85/ 78.85
E_K	mV	-103.99 / -103.99	-103.977/ -103.977	-103.97/ -103.97
E_{Cl}	mV	-70.22 / -70.22	-84.243/ -84.243	-81.00/ -81.02
MP	mV	-70.22 / -70.22	-71.349/-71.349	-71.536/ -71.526
Vol.	μm^3	1999.88 / 1999.88	1946.54 / 1946.54	1956.33/ 1956.19
ATP	amol/s	216.24 / 216.24	219.039/ 219.039	219.50/219.50

Compared to the standard steady state, this perturbation results in a volume decrease of approximately 43.5 um^3 and a 1.3 mV more polarized MP (Figs. 3.2.12 B and A). The change in MP is minimal as it primarily depends on the unchanged $P_{leak,Na}$:$P_{leak,K}$ ratio. Moreover, excess Cl^- resulting from a greater Cl^- leak influx diffuses towards the posterior end, increasing J_{KCl} on both ends and allowing more K^+ to exit the cell. Furthermore, the polarized membrane leads to a larger Na^+ leak influx and a smaller K^+ leak efflux. The active feedback senses the increase in $[Na^+]_i$, causing the pump to work harder, and ATP consumption increases accordingly (Fig. 3.2.12 E). At steady state, I_{axial} is approximately 1 pA (Fig. 3.2.12 F). However, the cytoplasmic voltage (Fig. 3.2.12 D) is almost zero because diffusion current dominates. Diffusion currents typically do not lead to the accumulation or separation of charges, thereby not creating a voltage difference.

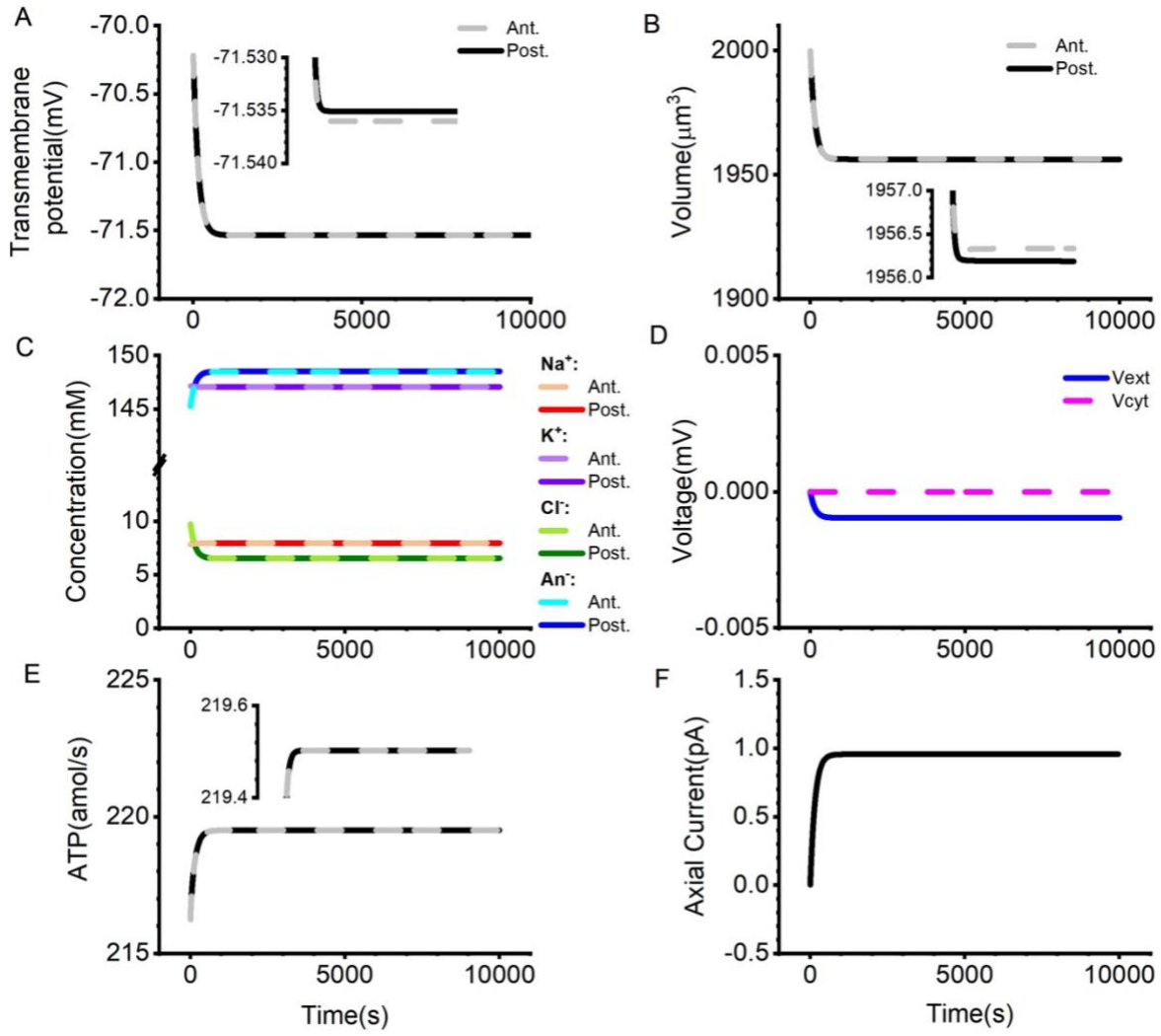

Figure 3.2.12 **Breaking symmetry via altering $P_{leak,Cl,a}$ with K/Cl.** Adding K/Cl co-transporters to both compartments renders the PA-CD no longer a minimal system. Increasing $P_{leak,Cl,a}$ by twofold will alter steady-state parameters.

3.2.3. Connectivity

The anterior and posterior compartments are linked through Nernst-Planckian diffusion and drift with the connectivity (Ccy). Connectivity depends on $D_{permeant\ ions}$, the cross-sectional area A, and the effective cell length L. The formular is $Ccy=D_{permeant\ ions}A/L$. Ccy_{ref} is the reference Connectivity (See Table 3.1 for Ccy_{ref}). The diffusion coefficient of ions depends on the temperature and viscosity of the solvent, according to Einstein's relation. Impermeant anions such as glutamate and ATP are larger and less diffusive than small permeant ions. As a result, we

assume that the diffusion coefficient of impermeant ions ($D_{impermeant\ ions}$) are 1,000 times smaller than the diffusion coefficient of permeant ions ($D_{permeant\ ions}$). The effective cell length L is measured between the centers of the two compartments and depends on the cell types. In our proposed model, we assume a uniform distribution of all channels and pumps, enabling ions to diffuse and drift from the center of the anterior to the posterior. Therefore, $D_{permeant\ ions}$ and length are constant, and the cross-sectional area is the only parameter that is varied to change Ccy.

This is a way to model gap junctions between cells. Gap junction channels between adjacent cells are formed by connexins. Ccy measures the connectivity of the junction which is determined by the number of open connexin channels. The properties of these channels, including pore size and regulation, are determined by interactions among various types of connexins. Additionally, the number of gap junction channels on a cell's surface can change rapidly in response to internal or external signals by adjusting the turnover rate of connexins (Giepmans, 2004). Astrocyte gap junctions are primarily formed by connexin-43, and their coupling depends on multiple regulators, such as extracellular K^+ concentrations and oxidative stress (Scemes and Spray, 2012; Johansen et al., 2011). Furthermore, Cao et al., (2013) reported that the typical EEF of a mouse brain is 3 V/m, which corresponds to the magnitude of V_{cyt}/Length in cell pairs with greater separation (Fig.3.2.6 E).

Connectivity plays a crucial role in determining the magnitude of the I_{axial} between the two compartments. The separation between the two compartments is greater when connectivity is smaller, and vice versa. If there is symmetry breaking, such as a doubled $P_{leak,Na,a}$, the compartments with higher separation exhibit a larger difference in MPs, volume, and internal ion concentration of each charge between the two compartments than those with a large connectivity (Fig. 3.2.13 A, B, and C).

In addition, I_{axial}, which is the sum of the diffusion and drift currents (Figs. 3.2.13 H and G), decreases due to the reduced connectivity (Fig. 3.2.13 F). In this case, there is a decrease in I_{trans}, which reduces V_{ext}, as illustrated in Fig. 3.2.13 D. V_{cyt} is calculated by subtracting V_p from V_a and then subtracting V_{ext}. With a smaller Vext and a larger difference between V_a and V_p, there is a larger EEF, resulting in more distinct compartments.

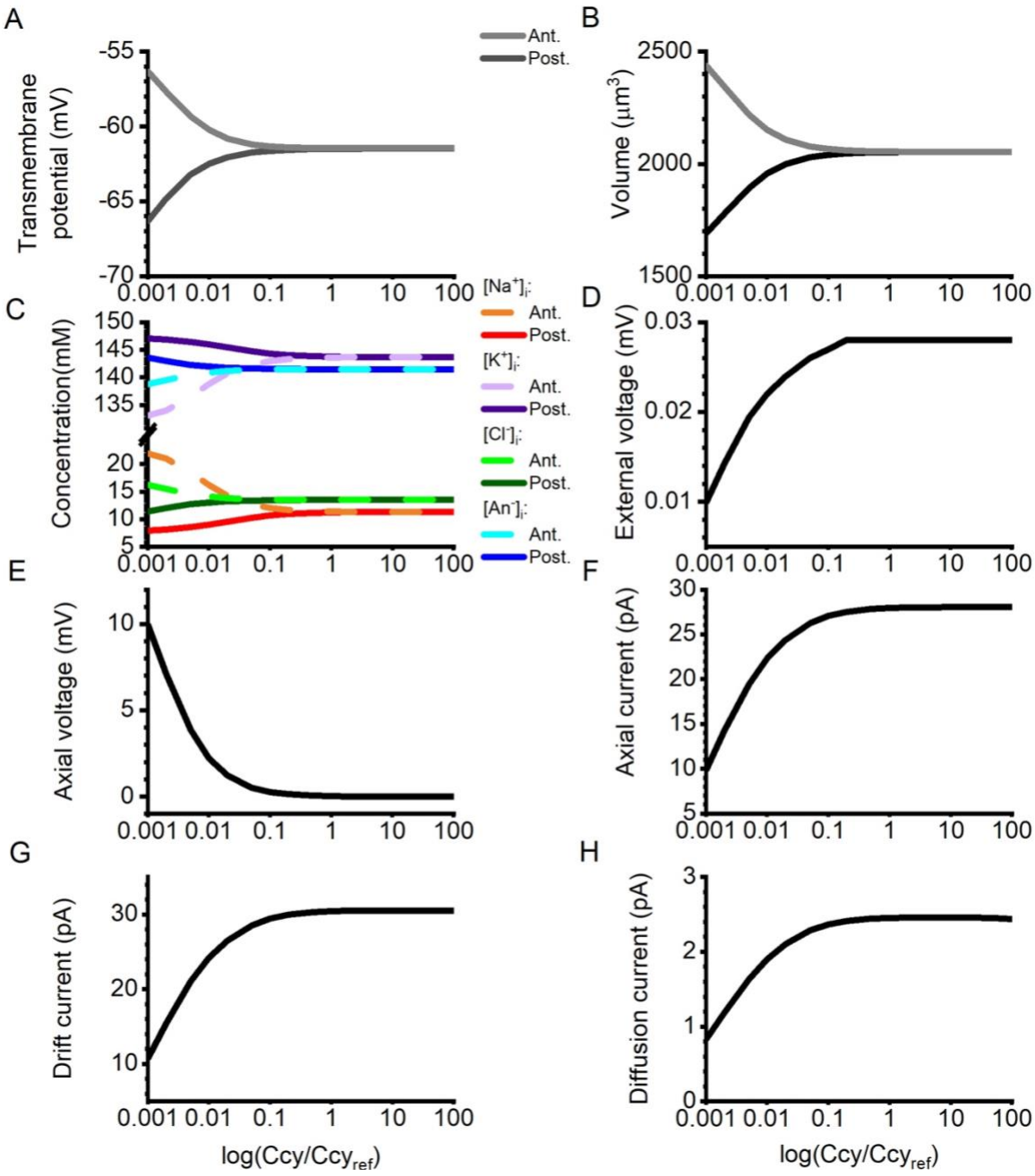

Figure 3.2.13 **Breaking symmetry by doubling $P_{leak,Na,a}$ with different Ccy, where $Ccy=D_{permeant\ ions}A/L$.** Measurements are taken for **A**: Transmembrane potential, **B**: Volume, **C**: Internal Ion Concentrations, **D**: External voltage, **E**: Axial voltage, **F**: Axial current, **G**: Drift current, and **H**: Diffusion current.

Astrocytes are a type of glial cells that originate from neuroepithelial cells of the ectoderm. They are widely distributed throughout the Central Nervous System (CNS) and crucial in various complex CNS activities. Astrocytes are electrically non-excitable. It is consistent with the non-excitable conditions in the PA-CD model (Verkhratsky et al., 2019; Sofroniew and Vinters, 2010). Previous studies have shown that the resistance of astrocyte gap junction coupling in mice is approximately 4.2 (Ma et al., 2016), indicating a more decoupled cell pair or compartment in the PA-CD model, with a Ccy range of 0.2 to 0.5, equivalent to 1.9 to 4.8 ohm. The small difference between V_a and V_p results in a high coupling coefficient (V_a/V_p) of around 99.7% and 99.8%. This finding aligns with Ma et al.'s (2016) suggestion that astrocytes play a crucial role in maintaining a stable environment for brain activity. Coordinated activity among astrocytes is essential for preserving homeostasis and facilitating neuronal signaling. However, their calculated coupling coefficient for coupled astrocyte pairs is 94% (Ma et al., 2016). It is slightly lower than the high coupling coefficient observed in this study.

3.2.4. R_{ext}

External resistance (R_{ext}) is the resistance of the cell's surrounding environment. The impact of varying R_{ext} on the steady-state and EEF is investigated in this study (Fig. 3.2.14). We break symmetry by doubling $P_{leak,Na,a}$. Changing R_{ext}, ranging from a 100-fold decrease in R_{ext} to a 10-fold increase, has a moderate effect on the remaining steady-state parameters. In these cases, the influence on Va_e and Vp_e is minimal, and changes in the steady-state parameters are insignificant.

However, when R_{ext} is increased significantly, such as from 10 times to 100 times, the two compartments become more distinct externally. In this scenario, the difference between Va_e and Vp_e becomes wider, resulting in a larger difference between V_a and V_p. As a result, the shift in MP becomes more significant (Fig. 3.2.7 A). The increasing difference between V_a and V_p decreases I_{axial} (Fig. 3.2.7 E) and V_{cyt} (Fig. 3.2.7 C). Thus, the size of EEF decreases.

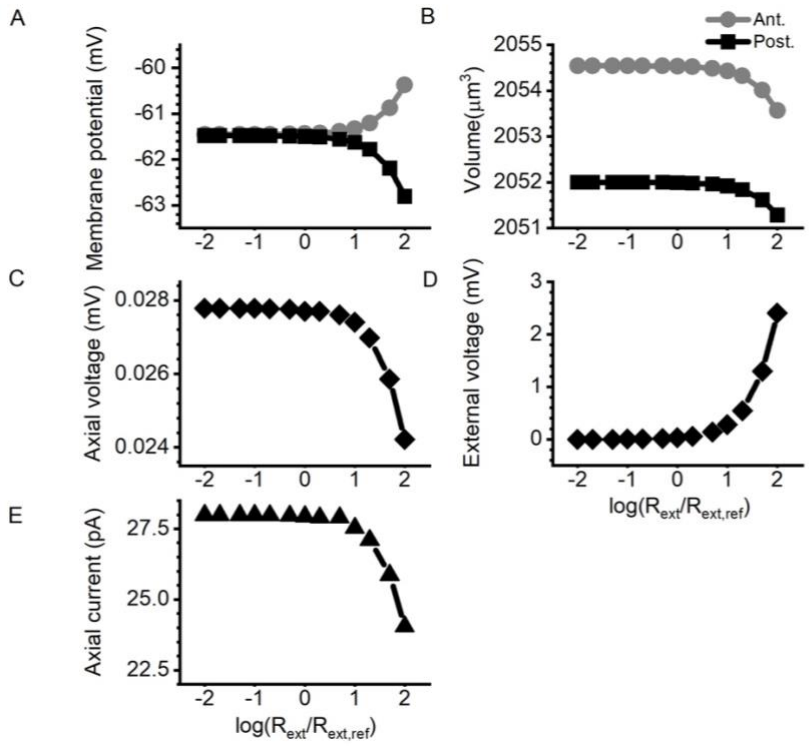

Figure 3.2.14 **Breaking symmetry by doubling $P_{leak,Na,a}$ at the anterior end with different R_{ext}. A:** Transmembrane potential, **B**: Volume, **C**: Axial voltage, **D**: External voltage, **E**: Axial current. The reference value of Ccy_{ref} is used.

4. Conclusion and Future Work

4.1. Conclusion:

4.1.1. The equivalent circuit model:

With the equivalent circuit model, the modeled *Eigenmannia*-type EODs are monophasic with head positive peaks and head negative baselines, which agree with dipole-oscillator like experimental recordings. The form of the EOD depends on the cytoplasmic current, and R_{gap} plays a crucial role in its size. Compared to the standard R_{gap}, the standard R_{cyt} is much smaller. Thus, R_{cyt} has negligible influence on the effective resistance and on the shape of EOD unless it has the same order of magnitude as R_{gap}. The size of the *Eigenmannia*'s anterior capacitor influences the EOD trough and resting state. Furthermore, the frequency can also affect the magnitude of EODs. *Eigenmannia*-type EODs can undergo high-frequency firing (up to 600Hz) as predicted by equivalent circuits. However, the EOD amplitude decreases if we maintain a constant Na channel density.

At the anterior end, there are also the tubular invaginations. The tubular voltage (V_t) depends on V_a with constant R_t and C_t. The tubular voltage fluctuates more with varying R_{gap}s than R_{cyt} and R_t. The changes in R_{gap} lead to a more significant alteration in V_a. However, the high resistance (R_t) on the anterior end exerts a minor influence on V_a, resulting in a trivial effect on EODs.

The observed EODs suggest the imperfect synchronicity of the activation of the electrocytes. We arbitrarily set the 1,000 electrocytes with different arrival times and changed the rate of pulsatile activation of the posterior AChR to an interval of 0.1 ms and 0.2 ms. The electric organ discharge (EOD) exhibits a more sinusoidal waveform with the 0.1 ms arrival time interval, consistent with the observed pattern in experimental recordings. The impact of imperfect synchronicity becomes more significant with larger populations of varied arrival times or longer time intervals. We observe that the amplitude of EOD decreases as the time interval or the differences in arrival time among populations increase. Notably, the EODs of 5 and 15 populations with a spacing of 0.2 ms cannot maintain *Eigenmannia*-style EODs. In conclusion, there is evidence of imperfect synchronicity in the activation of the 1,000 electrocytes.

Electrophorus-type EOD can be obtained from the formalism used to generate *Eigenmannia*-type EOD by adding anterior abundant K^+ leak channels, whose permeability is one-thousand-fold larger than posterior leak and decreasing *Eigenmannia*'s R_{gap} and R_{cyt}. By making these changes, V_a has a DC feature, the circuit model predicts that the EOD of *Electrophorus* is stronger than *Eigenmannia*'s and has a head-positive peak and a nearly neutral baseline. This prediction aligns with experimental findings.

However, our goal in this thesis is not modeling how powerful the taser-like EOD is. Instead, we evaluate if these tunable *Electrophorus*-type EODs are stable. To this end, the membrane potentials and EODs are measured with inputs of 100 ms at 200Hz. During firing, the results indicate that EOD is stable over a longer firing time. Additionally, we evaluate the EOD at 100Hz, a frequency at which *Electrophorus* produces bursts related to predation. Consequently, the EOD amplitude slightly increases, reaching around 593 mV, and the EOD baseline approaches closer to zero. Therefore, the predicted *Electrophorus*-type EODs is comparable to the experimental recording with the larvae stage of *Electrophorus*.

In conclusion, the equivalent circuit model provides a novel paradigm in which the circuit model is subject to the assumption of ion homeostasis, resulting in *Eigenmannia*-type and *Electrophorus*-type EOD with variable electrophysiologic settings.

4.1.2. PA-CD

The PA-CD is a non-excitable one-dimensional minimal model with anterior and posterior compartments connected by Nernst-Planckian diffusion and drift. In this model, we postulate that 50% of the impermeant anions are migratory inter-compartmentally to simulate the distribution of impermeant anions. We assume that our cell and its surroundings constitute a closed circuit. Therefore, the steady-state transmembrane current and axial current must be equal. Moreover, the net currents of each ion are zero at the steady state. The steady-state parameters of the anterior and posterior ends, i.e., transmembrane potential, volume, and the set of internal concentrations, are equal with these symmetrical two compartments.

Moreover, the one-dimensional PA-CD model can also be viewed as gap junctionally coupled cell pairs, where gap junctions are intercellular channels that enable communication and ion exchange between adjacent zero-dimensional cells. As the standard PA-CD is a minimal system, $P_{leak,Na}$:$P_{leak,K}$ ratio is crucial for establishing the transmembrane potentials. Altering the $P_{leak,Na}$:$P_{leak,K}$ ratio at one end through $P_{leak,Na}$ or $P_{leak,K}$ could result in an experimentally comparable EEF. The effects of doubling the $P_{leak,Na,a}$:$P_{leak,K,a}$ ratio by either a 2-fold increase in $P_{leak,Na,a}$ or a 0.5-fold decrease in $P_{leak,K,a}$ are different. Furthermore, changing P_{Cl} will not have any influence on the steady state because $P_{leak,Cl}$ is in a passive feedback loop and $[Cl^-]_i$ depends only on the $P_{leak,Na}$:$P_{leak,K}$ -dependent V_{rest}.

The PA-CD will no longer be a minimal system if chloride-cation cotransporters are introduced at both compartments. The system is evaluated using $Na^+K^+2Cl^-$ cotransporter (NKCC) and K^+/Cl^- cotransporter (K/Cl). Compared to the uniform cell without cotransporters, the cell with K/Cl has a smaller volume, a more polarized transmembrane potential, increased $[Na^+]_i$ and $[An^-]_i$, and decreased $[K^+]_i$ and $[Cl^-]_i$ in steady state. However, with NKCC, the uniform cell reaches a steady state characterized by an increase in volume, a more depolarized transmembrane potential, an increase in $[Na^+]_i$ and $[Cl^-]$i, and a decrease in $[K^+]_i$ and $[An^-]_i$. When K/Cl and NKCC coexist in a cell, the K/Cl: NKCC ratio is significant. Our system is dominated by NKCC. Therefore, the uniform cell with K/Cl and NKCC has the same changing

tendency as with NKCC. However, coexistence with K/Cl makes the cell less polarized and shrunken than when only NKCC is present. Moreover, symmetry breaking in non-minimal systems by a changing $P_{leak,Cl}$ at one end also produces an I_{axial}. However, the EEF is almost zero because diffusion current dominates. In this scenario, mobile impermeant anion electrophoresis and cell volume will adjust.

The V_{ext} depends on the external resistance R_{ext}.The total charge in the system remains constant. As R_{ext} increases, the difference between V_a and V_p results in a decrease in V_{cyt} or EEF, which dominates I_{axial}. When R_{ext} is extremely high, EEF is zero, and the two compartments function like a single compartment cell with the same volume. Moreover, the V_{ext} is determined by the I_{trans}, and thus, less connected compartments lead to a smaller V_{ext}.

The connectivity (Ccy) of the anterior and posterior compartments is determined by $D_{permeant\ ions}$A/Length. When the $D_{permeant\ ions}$A/Length gets small, the separation between the two compartments is increased, and vice versa. In the presence of symmetry breaking, such as a double $P_{leak,Na,a}$ at the anterior end, compartments with lower connectivity (higher separation) exhibit a more significant difference in transmembrane potential, volume, and internal concentration of each ion than those with higher connectivity. The axial current (I_{axial}) and EEF change with different connectivity.

In summary, minimal and non-minimal PA-CD systems produce an endogenous electric field through symmetry breaking via $P_{leak,Na}$ and $P_{leak,K}$. The size of the endogenous electric field (EEF) depends on connectivity and R_{ext}, while cotransporters have a negligible impact on it. Additionally, symmetry breaking via $P_{leak,Cl}$ in the non-minimal system changes the steady state. However, it produces a zero EEF. Therefore, the PA-CD system can serve as a fundamental one-dimensional model for understanding the endogenous electric field resulting from symmetry breaking.

4.2. Limitations and future study

4.2.1. The equivalent circuit model:

The range of *Eigenmannia* firing frequency recorded by numerous studies is discrepant. The claimed minimum frequency is 200 or 250 Hz. However, the highest frequency is more ambiguous, being 500Hz, 600Hz, or 700Hz (Hopkins, 1974; Scheich, 1977; Heiligenberg, 1991).

In this circuit model, we assume that *Eigenmannia* firing frequency range is between 200 and 500 Hz. As demonstrated by a prior study (Joos et al., 2018), maintaining the constant amplitude of EODs becomes challenging at high frequencies, specifically at 600Hz and 700Hz. As mentioned in the results Section 2.2.2, when frequency increases, the peak of *Eigenmannia*-type EODs becomes less depolarized. Therefore, the selected P_{Namax} could be insufficient to maintain a consistent peak during higher-frequency firing. As done Joos et al. (2018) a larger P_{Namax} should be used to maintain a constant depolarization.

Eigenmannia adjust their EOD frequencies to minimize jamming when surrounding fish emit signals at similar frequencies. *Eigenmannia* increases its firing frequency if its frequency is higher than its neighbors and decreases it if *Eigenmannia*'s frequency is lower. This phenomenon is the Jamming Avoidance Response (Watanabe and Takeda, 1963; Hopkins, 1974). In this thesis, *Eigenmannia*-type EODs with different firing frequencies are evaluated. However, in this thesis, we evaluate *Eigenmannia*-type EODs with different firing frequencies. However, we examine neither the resultant EOD nor the recovery process. In future research, we intend to enhance the functionality of AChR to mimic this behaviour.

As discussed previously, we consider the anterior end a pure capacitor. However, the immunohistochemistry evidence provided by Ban et al. (2015) shows that Na^+ activated K^+ channels, inward-rectifier K+ channels, and Na^+-K^+-ATPases are on the anterior end. *Eigenmannia'*s anterior face membrane must be fully capacitive to function as a dipole oscillator. Therefore, it is possible that the two types of potassium channels and pumps are confined to the ultrafine tubules. If these components are behind an exceptionally high tubular resistance, their electrical influence may be negligible. In the case of *Electrophorus*, Na^+/K^+ ATPases and K^+ channels are also found at the anterior end. However, the massive potassium leak channel will cause the membrane potential to approach the E_L. Future research will be required to explore the in-situ mechanism of Na^+/K^+ ATPases and K^+ channels in non-innervated tissue using immunohistochemistry or producing fluorescence-tagged mutants combined with live microscopy for real-time observation.

As reported by Cox et al. in 1945, the *Electrophorus* can generate up to 1 A of current. However, our computational results do not produce such a high current. This disparity in results may be attributable to the imperfect proportionality of our parameters, including effective resistance, capacitance, and channel permeability. To enhance our research, we plan to enhance

our model to not only replicate the shape of *Electrophorus*-type electric organ discharges (EOD) but also consider the substantial electrical current generated by its electric organ.

This spatially defined equivalent circuit model is a powerful computational tool to study the electrophysiologic features of electric fish. Generally, we compare the predicted results with experimental findings to check their validity. Throughout this study, it has become apparent that there is a shortage of detailed recorded electric organ discharge (EOD) data for *Eigenmannia* and *Electrophorus* in the existing literature. Furthermore, additional investigation into the external resistance is deemed necessary.

In this thesis, we discuss the role of R_{ext} in estimating effective resistance and its impacts on the form of electric organ discharge (EOD). Initially, R_{ext} was assumed to be 0.03 MΩ based on the equivalent circuit model's ability to produce EODs comparable to experimental results using this value. However, this assumption corresponds to a resistivity 100 times larger than the general water resistivity, typically 5 kΩ /cm (Assad et al., 1998). To assess the *Eigenmannia* circuit model using R_{ext} calculated with the typical water resistivity, stimulations were conducted. However, the simulated *Eigenmannia* electric organ (EO) failed to produce EODs with a reasonable amplitude. Moreover, the shape and amplitude of EODs were distorted as the cytoplasmic current (I_{cyt}) increased, coupled with 100 times smaller R_{ext}. Since EODs happened during the charging and discharging of EO, we tried to preserve EODs' shape by increasing the anterior capacitance while reducing the values of R_{ext} and R_{gap}. However, even with these adjustments, the resulting EOD still did not meet the expectations. The model encounters difficulties in accurately maintaining the *Eigenmannia* wave as I_{cyt} increases. In the case of *Electrophorus*, we assume that it shares the same R_{ext} as *Eigenmannia* since both species inhabit the same environment and *Electrophorus* curves its body during predation, with a head-to-tail distance similar to *Eigenmannia*'s size (Catania, 2019). The model mimicked the shape of *Eigenmannia*-type EODs, characterized by a head-positive peak and a neutral baseline. However, when attempting to mimic an adult-sized *Electrophorus* (M=50, N=5000), the electrocyte current was too small to exhibit the bio-taser-like characteristics. In contrast to *Eigenmannia*, reducing R_{ext} in the *Electrophorus* model could make the simulation more realistic and trigger a powerful bio-taser-like current. Furthermore, for these two genera of fish, we consider R_t a high resistance to hold voltage in the tubule. However, we should continue evaluating this feature.

In conclusion, experimental measurements on these two fish are needed to provide additional electrophysiological information and validate the computational results. Additionally, there is a need to enhance the equivalent circuit model to mimic more realistic electric organ discharge (EOD) features of *Eigenmannia* and *Electrophorus*.

4.2.2. PA-CD:

The PA-CD model is a non-excitable model with an anterior and a posterior compartment linked by Nernst-Planckian diffusion and drift. To simplify the model, voltage-gated channels have been omitted. However, our final objective is to develop a one-dimensional model of an excitable cell. In the future, it will be necessary to incorporate voltage-gated channels into the PA-CD model, as they are critical for ion homeostasis in excitable cells. The type of voltage-gated channel that will be introduced depends on the cell types.

Excitable cells are divided into two kinds using the pump-leak Donnan mechanism: those that are pump-leak dominant and those that are Donnan dominant. Only pump-leak-dominant cells are examined in this study. To analyze cell ion homeostasis in more depth, it is necessary to evaluate PA-CD with Donnan-dominant parameter values under excitable and non-excitable conditions.

Impermeant anions also play a key role in ion homeostasis. In PA-CD, we assume that each compartment has the same amount of impermeant anions, valence of -1, and mobility, i.e., 50% of the impermeant anions. We have observed that When the PA-CD compartmental symmetry is broken by doubling the $P_{leak,Na,a}$ at the anterior end with 100 percent mobile impermeant anion, the system ends up with all the impermeant anions at the anterior end. The underlying mechanism of this phenomenon is unclear. In addition, the impermeant anions are dispersed unevenly across the cell and have various valences, i.e., ATP with a valence of -4 and the sulfate ion with a valence of -2. For future investigation, we may vary the amount of mobile impermeant anion inside a given compartment and assess the effect of impermeant anion valence.

Additionally, live cells include impermeant cations, such as positively charged amino acids such as lysine (Lys, K) and histidine (His, H). We should add impermeable cations to our system in the future.

5. Bibliography:

Assad, C., B. Rasnow, P.K. Stoddard, and J.M. Bower. 1998. The electric organ discharges of the gymnotiform fishes: II. Eigenmannia. *Journal of Comparative Physiology A: Sensory, Neural, and Behavioral Physiology*. 183:419–432. doi:10.1007/s003590050268.

Ban, Y., B.E. Smith, and M.R. Markham. 2015. A highly polarized excitable cell separates sodium channels from sodium-activated potassium channels by more than a millimeter. *Journal of Neurophysiology*. 114:520–530. doi:10.1152/jn.00475.2014.

Bauer, R. 1979. Electric organ discharge (EOD) and prey capture behaviour in the electric eel, Electrophorus electricus. *Behav Ecol Sociobiol*. 4:311–319. doi:10.1007/BF00303239.
Bennett, M.V.L. 1971. Electric Organs. *In* Fish Physiology. Elsevier. 347–491.

Billman, G.E. 2020. Homeostasis: The Underappreciated and Far Too Often Ignored Central Organizing Principle of Physiology. *Front. Physiol.* 11:200. doi:10.3389/fphys.2020.00200.
Cannon, W.B. 1963. The wisdom of the body. Revised and Enlarged edition. W. W. Norton & Company. 340 pp.

Cao, L., D. Wei, B. Reid, S. Zhao, J. Pu, T. Pan, E.N. Yamoah, and M. Zhao. 2013. Endogenous electric currents might guide rostral migration of neuroblasts. *EMBO Rep*. 14:184–190. doi:10.1038/embor.2012.215.

Catania, K. 2014. The shocking predatory strike of the electric eel. *Science*. 346:1231–1234. doi:10.1126/science.1260807.

Catania, K.C. 2016. Leaping eels electrify threats, supporting Humboldt's account of a battle with horses. *Proc. Natl. Acad. Sci. U.S.A.* 113:6979–6984. doi:10.1073/pnas.1604009113.

Catania, K.C. 2017. Power Transfer to a Human during an Electric Eel's Shocking Leap. *Current Biology*. 27:2887-2891.e2. doi:10.1016/j.cub.2017.08.034.

Catania, K.C. 2019. The Astonishing Behavior of Electric Eels. *Front. Integr. Neurosci.* 13:23. doi:10.3389/fnint.2019.00023.

Cox, R.T., C.W. Coates, and M.V. Brown. 1945. ELECTRIC TISSUE. *Journal of General Physiology*. 28:187–212. doi:10.1085/jgp.28.3.187.

Craig, J.M., L.Y. Kim, V.A. Tagliacollo, and J.S. Albert. 2019. Phylogenetic revision of Gymnotidae (Teleostei: Gymnotiformes), with descriptions of six subgenera. *PLoS ONE*. 14:e0224599. doi:10.1371/journal.pone.0224599.

Cuellar, H., J.A. Kim, G.A. Unguez, H. Cuellar, J.A. Kim, and G.A. Unguez. 2006. Evidence of post-transcriptional regulation in the maintenance of a partial muscle phenotype by electrogenic cells of S. *macrurus*. *FASEB j.* 20:2540–2540. doi:10.1096/fj.06-6474fje.

Dijkstra, K., J. Hofmeijer, S.A. van Gils, and M.J.A.M. van Putten. 2016. A Biophysical Model for Cytotoxic Cell Swelling. *J. Neurosci.* 36:11881–11890. doi:10.1523/JNEUROSCI.1934-16.2016.

Düsterwald, K.M., C.B. Currin, R.J. Burman, C.J. Akerman, A.R. Kay, and J.V. Raimondo. 2018. Biophysical models reveal the relative importance of transporter proteins and impermeant anions in chloride homeostasis. *eLife*. 7:e39575. doi:10.7554/eLife.39575.

Ferraris Jr, C.J., C.D. De Santana, and R.P. Vari. 2017. Checklist of Gymnotiformes (Osteichthyes: Ostariophysi) and catalogue of primary types. *Neotrop. ichthyol.* 15. doi:10.1590/1982-0224-20160067.

Finger, S., and M. Piccolino. 2011. The shocking history of electric fishes: from ancient epochs to the birth of modern neurophysiology. Oxford University Press, New York. 470 pp.

Fraser, J.A., and C.L.-H. Huang. 2004. A quantitative analysis of cell volume and resting potential determination and regulation in excitable cells: Quantitative relationships between cell volume and resting potential. *The Journal of Physiology*. 559:459–478. doi:10.1113/jphysiol.2004.065706.

Fraser, J.A., C.L.-H. Huang, and T.H. Pedersen. 2011. Relationships between resting conductances, excitability, and t-system ionic homeostasis in skeletal muscle. *Journal of General Physiology*. 138:95–116. doi:10.1085/jgp.201110617.

Funk, R.H.W. 2015. Endogenous electric fields as guiding cue for cell migration. *Front. Physiol.* 6. doi:10.3389/fphys.2015.00143.

Giepmans, B. 2004. Gap junctions and connexin-interacting proteins. *Cardiovascular Research*. 62:233–245. doi:10.1016/j.cardiores.2003.12.009.

Gifford, J., and M. Leming. 2021. The Innovative Power of the Electric Eel (Electrophorus electricus). *In* Biomimetics and Bionic Applications with Clinical Applications. M. Israelowitz, B. Weyand, H.P. von Schroeder, P. Vogt, M. Reuter, and K. Reimers, editors. Springer International Publishing, Cham. 71–79.

Gotter, A.L., M.A. Kaetzel, and J.R. Dedman. 1998. Electrophorus electricus as a Model System for the Study of Membrane Excitability. *Comparative Biochemistry and Physiology Part A: Molecular & Integrative Physiology*. 119:225–241. doi:10.1016/S1095-6433(97)00414-5.
Heiligenberg, W. 1991. Neural nets in electric fish. Mit Press Ltd.

Henninger, J., R. Krahe, F. Sinz, and J. Benda. 2020. Tracking activity patterns of a multispecies community of gymnotiform weakly electric fish in their neotropical habitat without tagging. *Journal of Experimental Biology*. jeb.206342. doi:10.1242/jeb.206342.

Hopkins, C.D. 1974. Electric Communication: Functions in the Social Behavior of Eigenmannia Virescens. *Behav*. 50:270–304. doi:10.1163/156853974X00499.

Johansen, D., V. Cruciani, R. Sundset, K. Ytrehus, and S.-O. Mikalsen. 2011. Ischemia Induces Closure of Gap Junctional Channels and Opening of Hemichannels in Heart-derived Cells and Tissue. *Cell Physiol Biochem*. 28:103–114. doi:10.1159/000331719.

Joos, B., M.R. Markham, J.E. Lewis, and C.E. Morris. 2018. A model for studying the energetics of sustained high frequency firing. *PLoS ONE*. 13:e0196508. doi:10.1371/journal.pone.0196508.
Keynes, R.D., and H. Martins-Ferreira. 1953. Membrane potentials in the electroplates of the electric eel. *The Journal of Physiology*. 119:315–351. doi:10.1113/jphysiol.1953.sp004849.

Klassen, S.A., and J.K. Shoemaker. 2021. Action potential subpopulations within human muscle sympathetic nerve activity: Discharge properties and governing mechanisms. *Autonomic Neuroscience*. 230:102743. doi:10.1016/j.autneu.2020.102743.

Kramer, B., and I. Kaunzinger. 1991. Electrosensory Frequency and Intensity Discrimination in the Wave-Type Electric Fish *Eigenmannia*. *Journal of Experimental Biology*. 161:43–59. doi:10.1242/jeb.161.1.43.

Kramer, L.B. 2019. Harmonic and temporal structure of electric organ discharges of the wave-type in Amazonian knifefishes (Gymnotiformes). *J Ethol*. 37:1–11. doi:10.1007/s10164-018-0560-1.

Lissmann, H.W. 1958. On the Function and Evolution of Electric Organs in Fish. *Journal of Experimental Biology*. 35:156–191. doi:10.1242/jeb.35.1.156.

Luft, J.H. 1957. The histology and cytology of the electric organ of the electric EEL (Electrophorus electricus, L.). *J. Morphol.* 100:113–139. doi:10.1002/jmor.1051000105.

Ma, B., R. Buckalew, Y. Du, C.M. Kiyoshi, C.C. Alford, W. Wang, D.M. McTigue, J.J. Enyeart, D. Terman, and M. Zhou. 2016. Gap junction coupling confers isopotentiality on astrocyte syncytium. *Glia*. 64:214–226. doi:10.1002/glia.22924.

Markham, M.R. 2013. Electrocyte physiology: 50 years later. *Journal of Experimental Biology*. 216:2451–2458. doi:10.1242/jeb.082628.

Morris, C.E., J.J. Wheeler, and B. Joos. 2022. The Donnan-dominated resting state of skeletal muscle fibers contributes to resilience and longevity in dystrophic fibers. *Journal of General Physiology*. 154:e202112914. doi:10.1085/jgp.202112914.

Nuccitelli, R., and L.F. Jaffe. 1974. Spontaneous Current Pulses Through Developing Fucoid Eggs. *Proc. Natl. Acad. Sci. U.S.A.* 71:4855–4859. doi:10.1073/pnas.71.12.4855.

Østby, I., L. Øyehaug, G.T. Einevoll, E.A. Nagelhus, E. Plahte, T. Zeuthen, C.M. Lloyd, O.P. Ottersen, and S.W. Omholt. 2009. Astrocytic Mechanisms Explaining Neural-Activity-Induced Shrinkage of Extraneuronal Space. *PLoS Comput Biol*. 5:e1000272. doi:10.1371/journal.pcbi.1000272.

Peixoto, L.A.W., G.M. Dutra, and W.B. Wosiacki. 2015. The Electric Glass Knifefishes of the *Eigenmannia trilineata* species-group (Gymnotiformes: Sternopygidae): monophyly and description of seven new species: *Eigenmannia Trilineata* Species-Group. *Zool J Linn Soc*. 175:384–414. doi:10.1111/zoj.12274.

Pietak, A., and M. Levin. 2017. Bioelectric gene and reaction networks: computational modelling of genetic, biochemical and bioelectrical dynamics in pattern regulation. *J. R. Soc. Interface.* 14:20170425. doi:10.1098/rsif.2017.0425.

Russell, J.M. 2000. Sodium-Potassium-Chloride Cotransport. *Physiological Reviews*. 80:211–276. doi:10.1152/physrev.2000.80.1.211.

Ryan, C.N.M., M.N. Doulgkeroglou, and D.I. Zeugolis. 2021. Electric field stimulation for tissue engineering applications. *BMC biomed eng*. 3:1. doi:10.1186/s42490-020-00046-0.

Sanjuan-Alberte, P., M.R. Alexander, R.J.M. Hague, and F.J. Rawson. 2018. Electrochemically stimulating developments in bioelectronic medicine. *Bioelectron Med*. 4:1. doi:10.1186/s42234-018-0001-z.

Scemes, E., and D.C. Spray. 2012. Extracellular K+ and Astrocyte Signaling via Connexin and Pannexin Channels. *Neurochem Res*. 37:2310–2316. doi:10.1007/s11064-012-0759-4.

Scheich, H. 1977. Neural basis of communication in the high frequency electric fish,Eigenmannia virescens (Jamming Avoidance Response): II. Jammed electroreceptor neurons in the lateral line nerve. *J. Comp. Physiol.* 113:207–227. doi:10.1007/BF00611989.

Schwartz, I.R., G.D. Pappas, and M.V.L. Bennett. 1975. The fine structure of electrocytes in weakly electric teleosts. *J Neurocytol*. 4:87–114. doi:10.1007/BF01099098.

Schwassmann, H.O., M.I.S. Assunção, and F. Kirschbaum. 2014. Ontogeny of the Electric Organs in the Electric Eel, Electrophorus electricus: Physiological, Histological, and Fine Structural Investigations. *Brain Behav Evol*. 84:288–302. doi:10.1159/000367884.

Sofroniew, M.V., and H.V. Vinters. 2010. Astrocytes: biology and pathology. *Acta Neuropathol*. 119:7–35. doi:10.1007/s00401-009-0619-8.

Song, Z., X. Cao, T.-L. Horng, and H. Huang. 2020. Electric discharge of electrocytes: Modelling, analysis and simulation. *Journal of Theoretical Biology*. 498:110294. doi:10.1016/j.jtbi.2020.110294.

Stoddard, P.K. 1999. Predation enhances complexity in the evolution of electric fish signals. *Nature*. 400:254–256. doi:10.1038/22301.

Thomas, M., D. Chrétien, A. Florion, and D. Terver. 1996. Real-Time Detection of Potassium Cyanide Pollution in Surface Waters Using Electric Organ Discharges Wave Emitted by the Tropical Fish, Apteronotus Albifrons. *Environmental Technology*. 17:561–574. doi:10.1080/09593331708616420.

Traeger, L.L., G. Sabat, G.A. Barrett-Wilt, G.B. Wells, and M.R. Sussman. 2017. A tail of two voltages: Proteomic comparison of the three electric organs of the electric eel. *Sci. Adv.* 3:e1700523. doi:10.1126/sciadv.1700523.

Verkhratsky, A., V. Parpura, N. Vardjan, and R. Zorec. 2019. Physiology of Astroglia. *In* Neuroglia in Neurodegenerative Diseases. A. Verkhratsky, M.S. Ho, R. Zorec, and V. Parpura, editors. Springer Singapore, Singapore. 45–91.

Watanabe, A., and K. Takeda. 1963. The Change of Discharge Frequency by A.C. Stimulus in A Weak Electric Fish. *Journal of Experimental Biology*. 40:57–66. doi:10.1242/jeb.40.1.57.
Wolfe, J.M. 1988. Sensory Systems: II. Birkhäuser Boston, Boston, MA. 20–22 pp.

Xu, J., X. Cui, and H. Zhang. 2021. The third form electric organ discharge of electric eels. *Sci Rep*. 11:6193. doi:10.1038/s41598-021-85715-3.

Xu, J., and D.A. Lavan. 2008. Designing artificial cells to harness the biological ion concentration gradient. *Nature Nanotech*. 3:666–670. doi:10.1038/nnano.2008.274.